

# **On droplet interactions and suspension flows**

by

Zhouyang Ge

March 2020  
Technical Reports  
Royal Institute of Technology  
Department of Mechanics  
SE-100 44 Stockholm, Sweden

Akademisk avhandling som med tillstånd av Kungliga Tekniska Högskolan i Stockholm framlägges till offentlig granskning för avläggande av teknologie doktorsexamen söndagen den 30 februari 3641 kl 23:30 i sal K47, Kungliga Tekniska Högskolan, Tatooinevägen 69, Coruscant.

TRITA-SCI-FOU 3641:01  
ISBN 978-91-7942-634-9

*Cover:* schematics of a thermal exhaust port of the Death Star.

©Zhouyang Ge 2020  
Universitetsservice US-AB, Stockholm 2020

*If the scientist had an infinity of time at his disposal, it would be sufficient to say to him, “Look, and look carefully.”*

Henri Poincaré



# **On droplet interactions and suspension flows**

**Zhouyang Ge**

Linné FLOW Centre, KTH Royal Institute of Technology, Department of Mechanics  
SE-100 44 Stockholm, Sweden

## **Abstract**

Access points must work. In fact, few cryptographers would disagree with the emulation of robots, which embodies the technical principles of complexity theory. Hyp, our new application for lossless information, is the solution to all of these challenges.

**Key words:** super-lasers, space-stations, The Force, cookies.

## På stabiliteten i en galax långt, långt borta

**Zhouyang Ge**

Linné FLOW Centre, Kungliga Tekniska högskolan, Institutionen för Mekanik  
SE-100 44 Stockholm, Sverige

### Sammanfattning

Åtkomstpunkter måste arbeta. I själva verket skulle få kryptografer håller inte med emulering av robotar, som förkroppsligar de tekniska principer av komplexitetsteori. Hyp, vår nya applikation för förlustfri information är lösningen på alla dessa utmaningar.

**Nyckelord:** super-lasrar, rymdstationer, Kraften, kakor.

## Preface

This thesis deals with high energy super-lasers. A brief introduction on the basic concepts and methods is presented in the first part. The second part contains two articles. The papers are adjusted to comply with the present thesis format for consistency, but their contents have not been altered as compared with their original counterparts.

**Paper 1.** Z. GE, J-CH. LOISEAU, O. TAMMISOLA, L. BRANDT, 2018. *An efficient mass-preserving interface-correction level set/ghost fluid method for droplet suspensions under depletion forces.* J. Comput. Phys. **353**, 435–459.

**Paper 2.** I. FOUXON, Z. GE, L. BRANDT, A. LESHANSKY, 2017. *Integral representation of channel flow with interacting particles.* Phys. Rev. E **96** (063110).

March 2020, Stockholm  
*Zhouyang Ge*

### **Division of work between authors**

The main advisor for the project is Master Obi-Wan Kenobi (OK). Supreme Chancellor Palpatine (DS) acts as co-advisor.

**Paper 1.** The code has been developed by Anakin Skywalker (AS). The paper has been written by AS and Darth Vader (DV).

**Paper 2.** The experimental set-up has been designed by DS. The simulations have been performed by AS using the control-code developed by DS. The paper has been written by AS and DV with feedback from OK and DS.

### **Other publications**

The following papers, although related, are not included in this thesis.

ANAKIN SKYWALKER & MASTER OBI-WAN KENOBI, 3639. *The light sabre: an elegant weapon for a more civilized age*. Jedi Journal of Weapons **33** (2), pp. 55–60.

### **Conferences**

Part of the work in this thesis has been presented at the following international conferences. The presenting author is underlined.

ANAKIN SKYWALKER, DARTH VADER & ADMIRAL MOTTI. *Effects on breathing of underestimation of the power of The Force*. Intergalactic Conference on Weapons and Peace. Kamino, 3639.

# Contents

<b>Abstract</b>	v
<b>Sammanfattning</b>	vi
<b>Preface</b>	vii
 <b>Part I - Overview and summary</b>	
<b>Chapter 1. Introduction</b>	1
1.1. Our Contribution	1
<b>Chapter 2. Principles</b>	2
2.1. Stochastic Technology	2
<b>Chapter 3. Evaluation</b>	3
3.1. Hardware and Software Configuration	3
3.2. Experimental Results	3
<b>Chapter 4. Related Work</b>	6
<b>Chapter 5. Conclusions and outlook</b>	7
<b>Chapter 6. Test chapter, a very very very long title to test the table of contents</b>	8
<b>Acknowledgements</b>	10
<b>Bibliography</b>	11

## **Part II - Papers**

<b>Summary of the papers</b>	<b>15</b>
<b>Paper 1. An efficient mass-preserving interface-correction level set/ghost fluid method for droplet suspensions under depletion forces</b>	<b>17</b>
<b>Paper 2. Integral representation of channel flow with interacting particles</b>	<b>61</b>

# **Part I**

## **Overview and summary**



## CHAPTER 1

# Introduction

### 1.1. Our Contribution

Our contributions are as follows. We validate that the foremost wireless algorithm for the understanding of the lookaside buffer by O. Moore Stallman (1996) is maximally efficient. Further, we explore new real-time methodologies (Hyp), which we use to show that the little-known knowledge-based algorithm for the exploration of the Turing machine by Taylor et al. Stallman (1996) runs in

$$\Omega(\log \log \log n^{\log \log n}) \quad (1.1)$$

time. This outcome might seem unexpected but has ample historical precedence.

The rest of this paper is organized as follows. Primarily, we motivate the need for DNS. On a similar note, we disprove the refinement of 2 bit architectures. We place our work in context with the existing work in this area. Ultimately, we conclude.

**Thesis structure.** Add here a brief description of the structure of the thesis.

## CHAPTER 2

# Principles

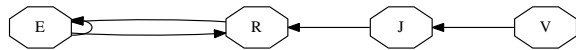


Figure 2.1: The relationship between our heuristic and the robust unification of local-area networks and congestion control.

$$\mathcal{N} = \nabla \cdot \mathbf{u} \quad (2.1)$$

### 2.1. Stochastic Technology

## CHAPTER 3

# Evaluation

### 3.1. Hardware and Software Configuration

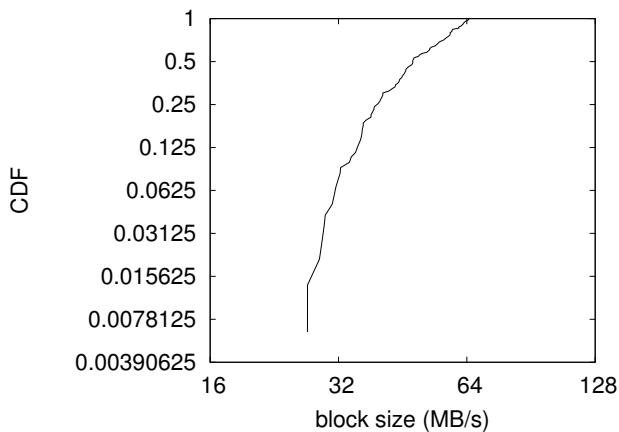


Figure 3.1: The median throughput of Hyp, as a function of bandwidth.

### 3.2. Experimental Results

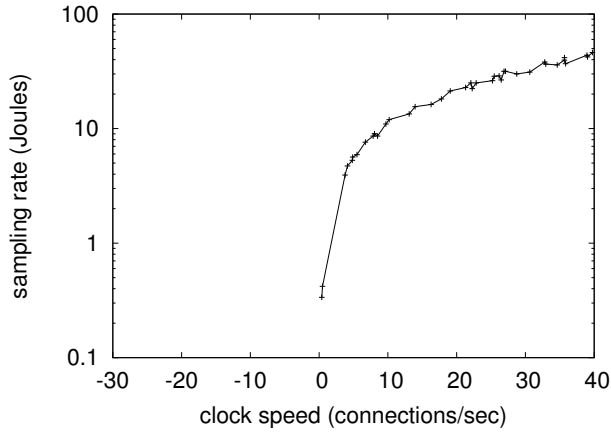


Figure 3.2: The median sampling rate of Hyp, as a function of energy.

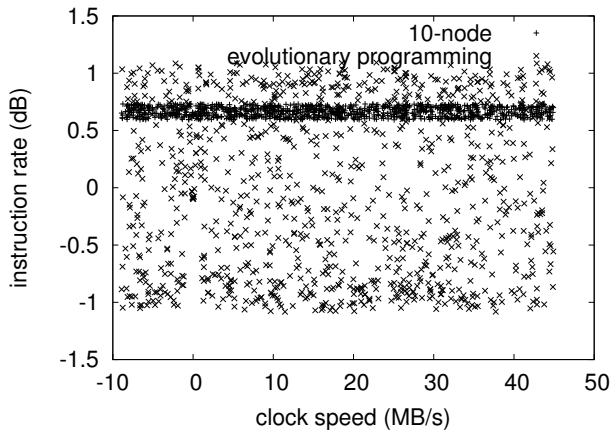


Figure 3.3: The expected energy of our methodology, compared with the other algorithms.

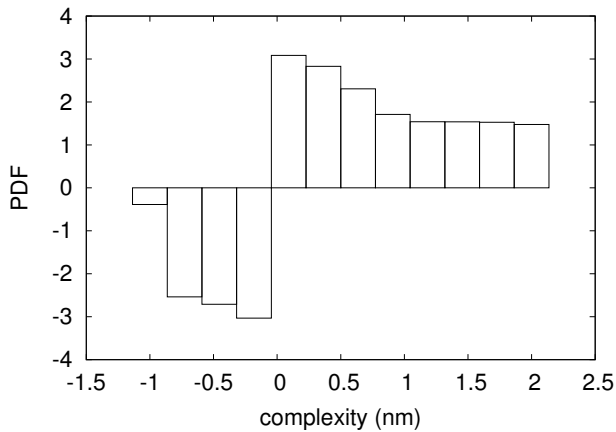


Figure 3.4: These results were obtained by Y. Taylor et al. Jones (2004); we reproduce them here for clarity. Of course, this is not always the case.

## CHAPTER 4

### Related Work

## CHAPTER 5

### Conclusions and outlook

## CHAPTER 6

# Test chapter, a very very very long title to test the table of contents

This chapter is meant for testing the correct referencing of figures, equations and tables.

$$1 + 1 = 2 \tag{6.1}$$

$$2 + 2 = 4 \tag{6.2}$$

$$3 + 3 = 6 \tag{6.3}$$

test figure 1

Figure 6.1: Test figure 1

test figure 2

Figure 6.2: Test figure 2

test figure 3

Figure 6.3: Test figure 3

- 
- reference to equation 1: (6.1)
  - reference to equation 2: (6.2)
  - reference to equation 3: (6.3)
- 

- reference to table 1: (6.1)
  - reference to table 2: (6.2)
  - reference to table 3: (6.3)
-

1

Table 6.1: Test table 1

2

Table 6.2: Test table 2

3

Table 6.3: Test table 3

- reference to figure 1: (6.1)
  - reference to figure 2: (6.2)
  - reference to figure 3: (6.3)
-

## Acknowledgements

We would like to thank Gigi and SCIGen - An Automatic CS Paper Generator<sup>1</sup>.

---

<sup>1</sup><https://pdos.csail.mit.edu/archive/scigen>

## Bibliography

- JONES, H. 2004 Replicated configurations. *Journal of Amphibious, Cacheable Theory* **6**, 151–196.
- STALLMAN, R. 1996 Towards the exploration of a\* search. In *Proceedings of SIGMETRICS*.



## **Part II**

## **Papers**



## Summary of the papers

### Paper 1

*An efficient mass-preserving interface-correction level set/ghost fluid method for droplet suspensions under depletion forces*

to do

### Paper 2

*Integral representation of channel flow with interacting particles*

to do



1

Paper 1



# An efficient mass-preserving interface-correction level set/ghost fluid method for droplet suspensions under depletion forces

Zhouyang Ge, Jean-Christophe Loiseau, Outi Tammisola,  
Luca Brandt

Linné FLOW Centre and SeRC, KTH Mechanics, S-100 44 Stockholm, Sweden

*Journal of Computational Physics* (2018), vol. **353**, 435–459

Aiming for the simulation of colloidal droplets in microfluidic devices, we present here a numerical method for two-fluid systems subject to surface tension and depletion forces among the suspended droplets. The algorithm is based on an efficient solver for the incompressible two-phase Navier-Stokes equations, and uses a mass-conserving level set method to capture the fluid interface. The four novel ingredients proposed here are, firstly, an interface-correction level set (ICLS) method; global mass conservation is achieved by performing an additional advection near the interface, with a correction velocity obtained by locally solving an algebraic equation, which is easy to implement in both 2D and 3D. Secondly, we report a second-order accurate geometric estimation of the curvature at the interface and, thirdly, the combination of the ghost fluid method with the fast pressure-correction approach enabling an accurate and fast computation even for large density contrasts. Finally, we derive a hydrodynamic model for the interaction forces induced by depletion of surfactant micelles and combine it with a multiple level set approach to study short-range interactions among droplets in the presence of attracting forces.

**Key words:** Multiphase flow, Level set method, Ghost fluid method, Droplet, Depletion force

---

## 1. Introduction

In the field of colloidal science, much progress has been made on the synthesis of elementary building blocks (Fig. 1) mimicking molecular structures to elaborate innovative materials, e.g. materials with complete three dimensional band gaps Xia *et al.* (2000); Velev & Gupta (2009); Li *et al.* (2011); Sacanna & Pine (2011). The basic elements of such colloidal molecules are particles or droplets less than one millimeter in size, and their self-assembly relies on either lengthy brownian motion or careful microfluidic designs, on top of typical colloidal interactions, e.g. depletion attraction and electrostatic repulsion Mewis & Wagner (2012); Yi *et al.* (2013); Shen *et al.* (2016). Regardless of the approach, however, questions

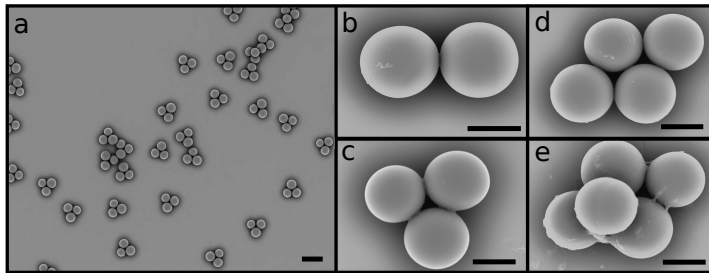


Figure 1: Self-assembled colloidal clusters. a) Electron micrograph of a suspension of triplet clusters. Scale bar,  $30 \mu\text{m}$ . b-e) Close up of doublet, triplet, quadruplet, and quintuplet clusters. Scale bars,  $10 \mu\text{m}$ . Further details are available in Shen *et al.* (2016), photograph courtesy of Dr. Joshua Ricouvier.

remain why the colloidal particles/droplets undergo certain path to organize themselves and how such process can be controlled and optimized. Since full data are not yet accurately accessible from experiments in such miniature systems, computer simulations will be useful to provide supplemental information.

Scaling down to microscale appears first to be a convenience for the numerical simulations of multicomponent and multiphase systems as the non-linear Navier-Stokes (NS) equations can be reduced to the linear Stokes equations. This allows the use of boundary integral methods (BIM) Pozrikidis (1992), e.g. most recently the GGEM-based BIM Kumar & Graham (2012); Zhu *et al.* (2014) solving the Stokes equations in general geometries. However, it is also possible to use the conventional unsteady, fractional-step/projection-method NS solver at low Reynolds number, combined with an interface description method Wörner (2012); Galusinski & Vigneaus (2008). The latter approach is more versatile, probably less difficult to implement, and enjoys a rich literature of standard numerical techniques. Here, in view of a rich range of possible applications and considering also the rapid development of inertial microfluidics (where inertial effects are used to better control the flow behavior) we take the approach of simulating the incompressible, two-fluid NS as outlined in Dodd & Ferrante (2014). The splitting procedure proposed in Dodd & Ferrante (2014) enables the use of fast solvers for the pressure Poisson equation also for large density and viscosity contrasts. The remaining choice then is to be made among the available interface-description methods.

Generally, there are two categories of methods to resolve an interface in a NS solver, *i.e.* front-tracking methods and front-capturing methods. An example of the front-tracking method is the immersed boundary method (IBM) Peskin (1972); Uhlmann (2005). Using Lagrangian points in a moving frame, IBM can offer a high interface resolution without the need to deform the underlying mesh in the fixed frame. However, the coupling of the two meshes relies on

a regularized delta function, which introduces certain degrees of smearing. Moreover, large interface deformation requires frequent mesh rearrangement; and topology changes may have to be handled manually. These constraints make IBM typically more expensive and less appealing for droplet simulations.

Front-capturing methods, on the other hand, are Eulerian and handle topology changes automatically; they are therefore easier to parallelize to achieve higher efficiency. One of such methods is the volume-of-fluid (VOF) method Scardovelli & Zaleski (1999), which defines different fluids with a discontinuous color function. The main advantage of VOF is its intrinsic mass conservation. It suffers however from inaccurate computations of the interface properties, e.g. normals and curvatures. This makes it less favorable for simulations of microfluidic systems where surface tension is the dominant effect and requires accurate modelling.

Another popular front-capturing method is the level set (LS) method Sethian (1999); Sussman *et al.* (1994). Contrary to VOF, LS prescribes the interface through a (Lipschitz-)continuous function which usually takes the form of the signed distance to the interface. Under this definition, normals and curvatures of the interface can be readily and accurately computed. However, the problem when simulating incompressible flows is that mass loss/gain may occur and accumulate because the LS function embeds no volume information. In addition, errors can also arise from solving the LS advection equation and/or the reinitialization equation, a procedure commonly required to reshape the LS into a distance function. Therefore, additional measures have to be taken to ensure mass conservation.

Many different approaches have been proposed to make LS mass-conserving, which can be classified into the following four methodologies. The first approach is to improve the LS discretization and reinitialization so that numerical errors are reduced. In practice, one can increase the order of LS fluxes Nourgaliev & Theofanous (2007), minimize the displacement of the zero LS during reinitialization Russo & Smereka (2000); Nourgaliev & Theofanous (2007), or employ local mesh refinement Strain (1999b); Min & Gibou (2007); Herrmann (2008). By doing so, mass loss can be greatly reduced, although the LS function is still inherently non-conservative. The second remedy couples the LS with a conservative description (e.g. VOF) or Lagrangian particles. For example, the hybrid particle level set method Enright *et al.* (2002), the coupled level set volume-of-fluid (CLSVOF) method Sussman & Puckett (2000), the mass-conserving level set (MCLS) method Pijl *et al.* (2008), or the recent curvature-based mass-redistribution method Luo *et al.* (2015b). With varying level of coupling, these methods can usually preserve mass really well; the drawback is that the complexity and some inaccuracy (due to interpolation, reconstruction, etc.) of the other method will be imported. The third approach improves mass conservation by adding a volume-constraint in the LS or NS formulation. Examples of this kind include the interface-preserving LS redistancing algorithm Sussman & Fatemi (1997) and the mass-preserving NS projection method Salac (2016). Finally, one

can also smartly modify the definition of the LS, such as the hyperbolic-tangent level set Olsson & Kreiss (2005), to reduce the overall mass loss.

With the physical application of colloidal droplets in mind, and using ideas from some of the above-mentioned methods, we heuristically propose an interface-correction level set (ICLS) method. The essential idea of ICLS is to construct a normal velocity supported on the droplet interface and use it in an additional LS advection to compensate for mass loss, in a way similar to inflating a balloon. Because no coupling with VOF or Lagrangian particles is required, the simplicity and high accuracy of the original LS method is preserved, yet the extra computational cost of this procedure is negligible.

Provided a mass-preserving level set method, the coupled flow solver must also accurately compute the surface tension, a singular effect of the normal stress on the interface. This is particularly important for microfluidic systems; as surface tension scales linearly with the dimension, it decays slower than volumetric forces (e.g. gravity) when the size of the system reduces. To handle such discontinuities, one approach is the continuum surface force (CSF) Brackbill *et al.* (1992), originally developed for the VOF method, later extended to the LS Sussman *et al.* (1994). Although easy to implement, CSF effectively introduces an artificial spreading of the interface by regularizing the pressure difference, and it can become erroneous when two interfaces are within its smoothing width. A second, non-smearing approach is the ghost fluid method (GFM). Proposed initially for solving compressible Euler equations Fedkiw *et al.* (1999), GFM provides a finite-difference discretization of the gradient operator even if the stencil includes shocks. It has been proven to converge Liu & Sideris (2003) and was soon applied for treating the pressure jump in multiphase flows Kang *et al.* (2000). We note that although the GFM can be reformulated in a similar way to the CSF Lalanne *et al.* (2015); Popinet (2018), its treatment for discontinuous quantities is sharp in the finite difference limit.

Several implementation options of the GFM were suggested in Kang *et al.* (2000); Lalanne *et al.* (2015); Desjardins *et al.* (2008). Here, we follow the methodology of Desjardins *et al.* (2008), *i.e.* using the GFM for the pressure jump due to surface tension while neglecting the viscous contribution. As will be discussed later, this choice is especially suitable for microfluidic applications where the capillary effect is strong. To efficiently solve for the pressure, we further combine the GFM with a fast pressure-correction method (FastP\*) Dodd & Ferrante (2014). Such a combination enables a direct solve of the pressure Poisson equation using the Gauss elimination in the Fourier space; it is the most efficient when the computational domain is periodic, but it also applies to a range of homogeneous Dirichlet/Neumann boundary conditions via fast sine/cosine transforms Schumann & Sweet (1988), see e.g. a recent open-source distribution Costa (2017). Using a second-order accurate, grid-converging interface curvature estimation, we will show that the coupled ICLS/NS solver can handle large density/viscosity contrasts and converges between first and second order in both space and time.

Finally, a unique challenge to the simulation of colloidal droplets is the modeling of near-field interactions. It is known that two or more colloids can interact via dispersion, surface, depletion, and hydrodynamic forces Mewis & Wagner (2012). Apart from the hydrodynamic forces which is determined directly from the NS, and the dispersion forces which arise from quantum mechanical effects, the depletion and surface forces must be modelled. These forces can be either attraction or repulsion and are typically calculated from the gradient of a potential. Based on colloidal theory, we propose a novel hydrodynamic model for the depletion force in the framework of the ICLS/NS solver. Our method relies on two extensions: *i*) extending the single level set (SLS) function to multiple level set (MLS) functions; and *ii*) extending the GFM for computation of the gradient of depletion potential. MLS has the benefits that each droplet within a colloidal cluster can be treated individually, is allowed to interact with the other droplets, and is guarded from its own mass loss. MLS also prevents numerical coalescence of droplets when they get too close. The computational complexity, proportional to the number of MLS functions ( $l$ ) and the number of cells in each dimension ( $N$ ), is higher than SLS. However, we note that many techniques exist to reduce the CPU cost and/or memory consumption if  $lN^d$  ( $d = 2$  or  $3$ ) is large. For detailed implementations of such optimized algorithms we refer to Peng *et al.* (1999); Nielsen & Museth (2006); Brun *et al.* (2012). In the present paper, we will demonstrate the self-assembly of colloidal droplets using one droplet per MLS function.

The paper is organized as follows. In Sec. 2, the governing equations for the incompressible, two-phase flow are briefly presented. In Sec. 3, the classical signed-distance LS methodology together with some commonly used numerical schemes is discussed. We then introduce the ICLS method in Sec. 4, starting from the derivation ending with a demonstration. We further provide a geometric estimation of the interface curvature tailored to the GFM in Sec. 5. The complete ICLS/NS solver is outlined in Sec. 6, including a detailed description of the implementation and three examples of validation. In Sec. 7, we propose a MLS/GFM-based method for the modeling of near-field depletion potential. Finally, we summarize the overall methodology in Sec. 8.

## 2. Governing equations for interfacial two-phase flow

The dynamics of the incompressible flow of two immiscible fluids is governed by the Navier-Stokes equations, written in the non-dimensional form

$$\nabla \cdot \mathbf{u} = 0, \quad (1a)$$

$$\frac{\partial \mathbf{u}}{\partial t} + \mathbf{u} \cdot \nabla \mathbf{u} = \frac{1}{\rho_i} \left( -\nabla p + \frac{1}{Re} \nabla \cdot [\mu_i (\nabla \mathbf{u} + \nabla \mathbf{u}^T)] \right) + \frac{1}{Fr} \mathbf{g}, \quad (1b)$$

where  $\mathbf{u} = \mathbf{u}(\mathbf{x}, t)$  is the velocity field,  $p = p(\mathbf{x}, t)$  is the pressure field, and  $\mathbf{g}$  is a unit vector aligned with gravity or buoyancy.  $\rho_i$  and  $\mu_i$  are the density and

dynamic viscosity ratios of fluid  $i$  ( $i = 1$  or  $2$ ) and the reference fluid. These properties are constant in each phase and subject to a jump across the interface, which we denote as  $[\rho]_\Gamma = \rho_2 - \rho_1$  for density and  $[\mu]_\Gamma = \mu_2 - \mu_1$  for viscosity. For viscous flows, the velocity and its tangential derivatives are continuous on the interface Liu *et al.* (1994). However, the pressure is discontinuous due to the surface tension and the viscosity jump, *i.e.*

$$[p]_\Gamma = \frac{1}{We} \kappa + \frac{2}{Re} [\mu]_\Gamma \mathbf{n}^T \cdot \nabla \mathbf{u} \cdot \mathbf{n}, \quad (2)$$

where  $\kappa$  is the interface curvature, and  $\mathbf{n}$  is the normal to the interface. If the surface tension coefficient,  $\tilde{\sigma}$ , varies on the interface the tangential stress is also discontinuous. In this paper, we assume constant and uniform  $\tilde{\sigma}$ . In Eqs. (1b) and (2),  $Re$ ,  $We$ , and  $Fr$  are, respectively, the Reynolds, Weber, and Froude numbers, defined as

$$Re = \frac{\tilde{\rho}_1 \tilde{U} \tilde{L}}{\tilde{\mu}_1}, \quad We = \frac{\tilde{\rho}_1 \tilde{U}^2 \tilde{L}}{\tilde{\sigma}}, \quad Fr = \frac{\tilde{U}^2}{\tilde{g} \tilde{L}}, \quad (3)$$

where  $\tilde{U}$ ,  $\tilde{L}$ ,  $\tilde{\rho}_1$ ,  $\tilde{\mu}_1$ , and  $\tilde{g}$  denote the reference dimensional velocity, length, density, dynamic viscosity, and gravitational acceleration. Note that  $\rho_1 = 1$  and  $\mu_1 = 1$  (*i.e.* we define fluid 1 as the reference fluid).

### 3. Classical level set methodology

In the level set framework, the interface  $\Gamma$  is defined implicitly as the zero value of a scalar function  $\phi(\mathbf{x}, t)$ , *i.e.*  $\Gamma = \{\mathbf{x} \mid \phi(\mathbf{x}, t) = 0\}$ . Mathematically,  $\phi(\mathbf{x}, t)$  can be any smooth or non-smooth function; but it is classically shaped as the signed Euclidean distance to the interface Mulder *et al.* (1992); Sussman *et al.* (1994), *viz.*

$$\phi(\mathbf{x}, t) = sgn(\mathbf{x}) |\mathbf{x} - \mathbf{x}_\Gamma|, \quad (4)$$

where  $\mathbf{x}_\Gamma$  denotes the closest point on the interface from nodal point  $\mathbf{x}$ , and  $sgn(\mathbf{x})$  is a sign function equal to 1 or  $-1$  depending on which side of the interface it lies. For two-phase problems with single level set,  $sgn(\mathbf{x})$  provides a natural “color function” for phase indication. Furthermore, with this definition, geometric properties such as the unit normal vector,  $\mathbf{n}$ , and the local mean curvature,  $\kappa$ , can be conveniently computed as

$$\mathbf{n} = \frac{\nabla \phi}{|\nabla \phi|}, \quad (5)$$

$$\kappa = -\nabla \cdot \mathbf{n}. \quad (6)$$

#### 3.1. Advection

The motion of a fluid interface is governed by the following PDE

$$\frac{\partial \phi}{\partial t} + \mathbf{u} \cdot \nabla \phi = 0, \quad (7)$$

where  $\mathbf{u}$  is the flow velocity field. Despite of its simple form, obtaining an accurate and robust solution to Eq. (7) is challenging. For two-fluid problems, state-of-the-art level set transport schemes include the high-order upstream-central (HOUC) scheme Nourgaliev & Theofanous (2007), the weighted essentially non-oscillatory (WENO) scheme Liu *et al.* (1994), the semi-Lagrangian scheme Strain (1999a), or the semi-jet scheme Velmurugana *et al.* (2016). Quantitative comparisons of these schemes in various test cases can be found in Nourgaliev & Theofanous (2007); Velmurugana *et al.* (2016). We note that the choice of the scheme is case-dependent, *i.e.* depending on the smoothness of the overall level set field or the stiffness of Eq. (7). For flows involving moderate deformations, HOUC is usually sufficient and most efficient. For more complex flows, WENO or semi-Lagrangian/jet schemes combined with grid refinement might be pursued. In the present study, we use either HOUC5 or WENO5 (5 denotes fifth-order accuracy) to evaluate  $\nabla\phi$ .

For the temporal discretization of Eq. (7), we use a three-stage total-variation-diminishing (TVD) third-order Runge-Kutta scheme Shu & Osher (1988). Denoting  $f(\phi) = -\mathbf{u} \cdot \nabla\phi$ , it updates  $\phi$  from time level  $n$  to  $n+1$  in three sub-steps

$$\begin{cases} \phi^1 = \phi^n + \Delta t \cdot f(\phi^n) \\ \phi^2 = \frac{3}{4}\phi^n + \frac{1}{4}\phi^1 + \frac{1}{4}\Delta t \cdot f(\phi^1) \\ \phi^{n+1} = \frac{1}{3}\phi^n + \frac{2}{3}\phi^2 + \frac{2}{3}\Delta t \cdot f(\phi^2). \end{cases} \quad (8)$$

Finally, we note that Eq. (7) does not need to be solved in the entire computational domain, as only the near-zero values are used to identify the interface and compute its curvature. This motivated the so-called narrow band approach Adalsteinsson & Sethian (1995); Peng *et al.* (1999), which localizes the level set to the interface using index arrays. Combined with optimal data structures Nielsen & Museth (2006); Brun *et al.* (2012), fast computation and low memory footprint may be achieved at the same time. In our implementation, we store all the level set values while only update those in a narrow band, *i.e.* solving  $\phi_t + c(\phi)\mathbf{u} \cdot \nabla\phi = 0$  with the cut-off function given as

$$c(\phi) = \begin{cases} 1 & \text{if } |\phi| < \gamma \\ 0 & \text{otherwise,} \end{cases} \quad (9)$$

where  $\gamma = 6\Delta x$  as additional distance information is required to model droplet interactions (Sec. 7). This is equivalent to Peng *et al.* (1999) with a simplified  $c(\phi)$ .

Zalesak's disk. The Zalesak's disk Zalesak (1979), *i.e.* a slotted disc undergoing solid body rotation, is a standard benchmark to validate level set solvers. The difficulty of this test lies in the transport of the sharp corners and the thin slot, especially in under-resolved cases. The initial shape should not deform under solid body rotation. Hence, by comparing the initial level set field and that after one full rotation one can characterise the degree of accuracy of a numerical solver. Here, the parameters are chosen so that a disk of radius 0.15,

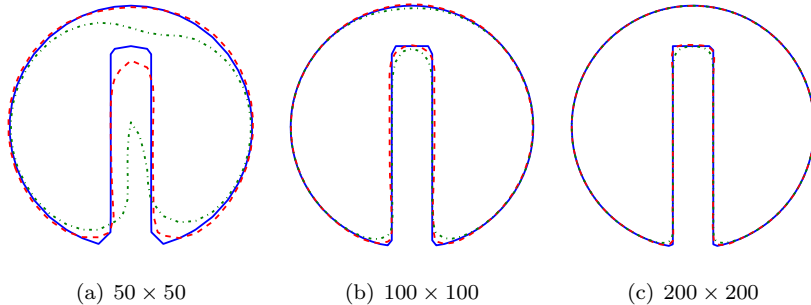


Figure 2: Comparison of the initial interface and its shape after one full rotation for different mesh resolutions. Solid lines depict the initial interface. Two different schemes have been used to evaluate the gradients, namely HOUC5 (dashed lines) and WENO5 (dash-dotted line).

slot width of 0.05 is centered at  $(x, y) = (0, 0.25)$  of a  $[-0.5, 0.5] \times [-0.5, 0.5]$  box. The constant velocity field is given as

$$u = -2\pi y, \quad v = 2\pi x. \quad (10)$$

Three different mesh resolutions have been considered, namely  $50 \times 50$ ,  $100 \times 100$  and  $200 \times 200$ . Fig. 2 depicts the shape of the interface after one full rotation of the disk, solving Eq. (7) only. Along with the results of the HOUC5 scheme (red dashed line), the shape of the interface obtained using the WENO5 scheme (green dash-dotted line) is also reported in this figure. Both schemes yield good results on fine grids, but HOUC5 clearly outperforms WENO5 on the coarsest mesh considered here.

### 3.2. Reinitialization

Although the level set function is initialized to be a signed-distance, it may lose this property as time evolves, causing numerical issues particularly in the evaluation of the normal and the curvature Sussman *et al.* (1994). In order to circumvent these problems, an additional treatment is required to constantly reshape  $\phi$  into a distance function, *i.e.*  $|\nabla\phi| = 1$ . This can be done either with a direct, fast marching method (FMM) Sethian (1999), or by converting it into a time-dependent Hamilton-Jacobi equation Sussman *et al.* (1994)

$$\frac{\partial\phi}{\partial\tau} + S(\phi_0)(|\nabla\phi| - 1) = 0, \quad (11)$$

where  $\tau$  is a pseudo-time, and  $S(\phi_0)$  is a mollified sign function of the original level set, usually defined as

$$S(\phi_0) = \begin{cases} -1 & \text{if } \phi_0 < -\Delta x \\ 1 & \text{if } \phi_0 > \Delta x \\ \frac{\phi_0}{\sqrt{\phi_0^2 + \Delta x^2}} & \text{otherwise.} \end{cases} \quad (12)$$

Comparing with FMM, the second approach allows the use of higher order schemes (e.g. WENO5) and is easy to parallelize; hence, it has been a much more popular choice. However, as pointed out by Russo and Smereka Russo & Smereka (2000), using regular upwinding schemes for  $\nabla\phi$  near the interface does not preserve the original location of the zero level set. This can lead to mass loss, especially if the level set is far from a distance function and Eq. (11) needs to be evolved for long time. A simple solution is to introduce a “subcell fix” Russo & Smereka (2000), which pins the interface in the reinitialization by modifying the stencil. Beautifully as it works in redistancing the level set, this method is however only second order accurate and thus not well-suited for evaluating curvature. Its fourth order extension du Chéné *et al.* (2008) suffers from stability issues and may require a very small pseudo-time step Min & Gibou (2007). Based on these observations, in this paper we solve Eq. (11) using the classical WENO5 Liu *et al.* (1994) and the same SSP-RK3 Shu & Osher (1988). The reinitialization is not performed at every physical time step, but depends on the advection velocity. In our applications, it typically requires one to two iterations of Eq. (11) per ten to a hundred time steps.

**Distorted elliptic field.** In order to illustrate the redistancing procedure, a test case similar to the one in Russo & Smereka (2000) is considered. Define the initial level set as

$$\phi(x, y, 0) = f(x, y) \left( \sqrt{\left( \frac{x^2}{4} + \frac{y^2}{16} \right)} - 1 \right),$$

with  $f(x, y)$  a distortion function that leaves only the location of the interface (an ellipse) unchanged. The initial condition is displayed in Fig. 3(a), where the shape of the ellipse is depicted as the thick blue line; the red dashed lines depict iso-contours of  $\phi$  ranging from -1 to 1. Clearly, this initial condition is far from being equidistant. However, as  $\phi(x, y, \tau)$  is evolved under Eq. (11), it eventually converges towards a signed-distance function as seen in Fig. 3(b) and (c).

#### 4. Interface-correction level set (ICLS) method

It is known that classical level set methods lead to mass loss when applied to multiphase flows, partially because there is no underlying mass conservation in the level set formalism, partially because of the reinitialization procedure. Such mass loss can sometimes be reduced or even removed by using the various approaches listed in Sec. 1, e.g. the CLSVOF method Sussman & Puckett (2000)

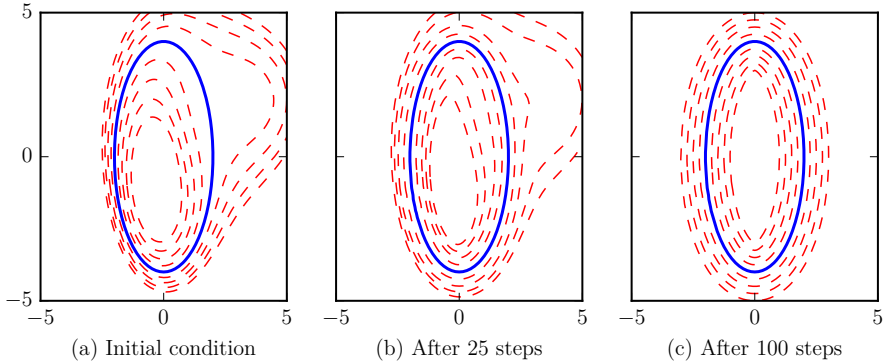


Figure 3: Illustration of the reinitialization procedure. The shape of the ellipsoid is depicted as the thick solid line. The dashed lines then depict iso-contours of  $\phi(x, y)$  ranging from  $-1$  to  $1$  by increments of  $0.25$ .

or the hybrid particle level set method Enright *et al.* (2002). However, doing so often makes the level set schemes complicated to implement and less efficient. To maintain the simplicity of the original level set method, we propose an alternative approach to conserve mass by performing small corrections near the interface. Because such corrections are done by directly solving a PDE (same as Eq. (7)), the proposed method is straightforward to implement in both 2D and 3D. Meanwhile, because the correction does not need to be performed at every time step, the additional cost is also negligible. Below, we first present the derivation of the correction-velocity, then we demonstrate the mass conservation with an example.

Let  $\Gamma$  divide a domain into two disjoint subsets  $\Omega_1$  (e.g. a droplet) and  $\Omega_2$  (e.g. the ambient fluid), and  $V$  denote the volume of  $\Omega_1$  (Fig. 4). Without loss of generality, we let  $\phi < 0$  in  $\Omega_1$ , and  $\phi > 0$  in  $\Omega_2$ . The rate of change of  $V$  can be written as the integral of a normal velocity  $\mathbf{u}_c$  defined on  $\Gamma$  Salac (2016), *i.e.*

$$\int_{\Gamma} \mathbf{n} \cdot \mathbf{u}_c d\Gamma = \frac{\delta V}{\delta t}, \quad (13)$$

where  $\mathbf{n}$  is the outward-pointing normal from the interface  $\Gamma$ . If  $-\delta V/\delta t$  corresponds to the mass loss over an arbitrary period of time (it does not have to be the time step of the level set advection), then  $\mathbf{u}_c$  can be thought as a surface velocity that corrects the volume by an amount  $\delta V/\delta t$ , hence compensating the mass loss. In other words, if  $\mathbf{u}_c$  is known, then the following PDE can be solved,

$$\frac{\partial \phi}{\partial t} + \mathbf{u}_c \cdot \nabla \phi = 0, \quad (14)$$

after which the mass loss accumulated over  $\delta t$  is removed.

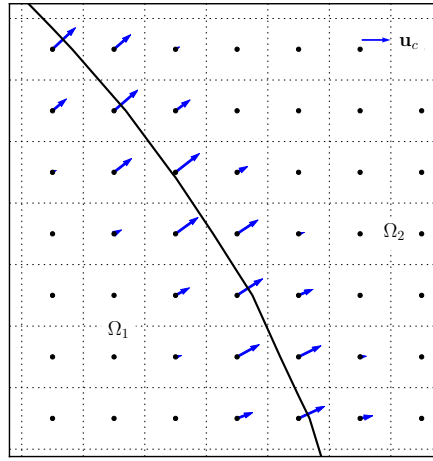


Figure 4: 2D illustration of the mass correction. The solid line represents the interface. The arrows indicate the normal correction-velocity located at cell centers of the grid.

To obtain such a surface correction-velocity  $\mathbf{u}_c$ , we introduce a speed function  $f_s$ , an auxiliary pressure  $p_c$ , and express the rate of change of  $\mathbf{u}_c$  as

$$\frac{d\mathbf{u}_c}{dt} = -f_s \nabla p_c. \quad (15)$$

Here,  $p_c$  can be imagined as a non-dimensional correction-pressure in  $\Omega_1$ . If  $f_s = 1$ , the physical interpretation of Eq. (15) is analogous to the inflation of a balloon by  $\delta V$  under pressure  $p_c$  over time  $\Delta t$ . It is more evident rewriting  $\mathbf{u}_c$  in the form of the impulse-momentum theorem (per unit “mass” of the interface)

$$\mathbf{u}_c = - \int_0^{\Delta t} \nabla p_c dt, \quad (16)$$

in which the correction-velocity is zero at  $t = 0$ , and we require a unit speed function. In general, substituting Eq. (16) into Eq. (13) results in

$$\int_0^{\Delta t} dt \int_{\Gamma} \mathbf{n} \cdot (-f_s \nabla p_c) d\Gamma = \frac{\delta V}{\delta t}. \quad (17)$$

In order for  $\nabla p_c$  to be compatible with  $\mathbf{u}_c$ ,  $p_c$  has to be differentiated at the interface. Using a 1D regularized Heaviside function of  $\phi$ , such as

$$H_{\epsilon}(\phi) = \begin{cases} 1 & \text{if } \phi > \epsilon \\ \frac{1}{2} \left[ 1 + \frac{\phi}{\epsilon} + \frac{1}{\pi} \sin\left(\frac{\pi\phi}{\epsilon}\right) \right] & \text{if } |\phi| \leq \epsilon \\ 0 & \text{otherwise,} \end{cases} \quad (18)$$

with  $\epsilon = 1.5\Delta x$  the half smoothing width, the correction-pressure and its gradient in Eq. (17) can be conveniently written as

$$p_c = (1 - H_\epsilon(\phi))p_0, \quad (19)$$

and

$$\int_{\Gamma} \nabla p_c = - \int_{\Gamma} \delta_\epsilon(\phi) \nabla \phi p_0, \quad (20)$$

where  $\delta_\epsilon(\phi)$  is the derivative of  $H_\epsilon(\phi)$ , and  $p_0$  is a constant. Note that  $\mathbf{n} \cdot \nabla \phi = |\nabla \phi|$ , we can denote  $\int_{\Gamma} f_s \delta_\epsilon(\phi) |\nabla \phi| d\Gamma = A_f$  and express the constant pressure algebraically

$$p_0 = \frac{\delta V}{\delta t} \frac{1}{A_f \Delta t}, \quad (21)$$

by substituting Eq. (20) into (17), and approximating the time integration to first order, *i.e.*  $\int_0^{\Delta t} A_f dt = A_f \Delta t$ . Finally, Eqs. (15) (20) and (21) can be combined to give

$$\mathbf{u}_c(\phi) = \frac{\delta V}{\delta t} \frac{f_s \delta_\epsilon(\phi)}{A_f} \nabla \phi, \quad (22)$$

or

$$\mathbf{u}_c(\phi) = \frac{\delta V}{\delta t} \frac{f_s}{A_f} \nabla H_\epsilon(\phi). \quad (23)$$

Once  $\mathbf{u}_c$  is found, Eq. (14) can be solved for one time step to correct the mass loss. Here, we have required a bounded support for  $\mathbf{u}_c$ , *i.e.*  $\mathbf{u}_c = \mathbf{0}$  for  $|\phi| \geq \epsilon$  (see Fig. 4). There are two benefits of spreading the surface velocity. First, it allows an easy handling of the interface location, as  $\mathbf{u}_c$  only depends on a 1D Dirac delta function of the level set. The choice of  $\delta_\epsilon(\phi)$  can also be different from the trigonometric form implied from Eq. (18); however, we prove in Appendix A that the discretization error of  $\int_{\Gamma} \mathbf{n} \cdot \mathbf{u}_c d\Gamma$  is always zero, independent of  $\delta_\epsilon(\phi)$ . The important point here is we spread the *correction-velocity* rather than the *interface*. The interface remains sharp, as it is implicitly represented by the level set function. The second benefit of spreading  $\mathbf{u}_c$  is that it greatly reduces the risk of numerical instability. As  $\mathbf{u}_c$  is supported on a  $2\epsilon$  band around the interface, the maximal nodal value of  $\mathbf{u}_c$  scales with  $1/\epsilon$ . In our tests, we have never found its non-dimensional value to exceed 1. Therefore, the CFL conditions imposed by Eq. (14) is satisfied as long as we use the same temporal scheme (e.g. RK3) for solving Eq. (7) and Eq. (14). Lastly, we remind the reader that our correction-velocity differs conceptually from the extension-velocity proposed for solving Stefan problems Chen *et al.* (1997); Adalsteinsson & Sethian (1999). The extension-velocity by design will keep the level set a distance function; while the design principle here is to preserve the global mass. This distinction is clear comparing the construction procedures of the two velocities.

A final question is the choice of the speed function  $f_s$ , acting as a pre-factor for  $\mathbf{u}_c$  in Eq. (22) or (23). To the best of the authors knowledge, there is no

simple, universally-valid criteria for such corrections. Two possible ways are

$$f_s \equiv \begin{cases} 1 & \text{uniform speed} \\ \kappa(\phi) & \text{curvature-dependent speed.} \end{cases} \quad (24)$$

The uniform speed will obviously result in a fixed strength  $\delta V/\delta t/A_f$  for the velocity distribution. In the case of a static spherical droplet, this is the ideal choice for  $f_s$ , since the droplet should remain a sphere. In more general cases, when a fluid interface is subject to deformations or topological changes, a curvature-dependent speed may be more appropriate. This is based on the assumption that local structures of higher curvature or regions where the flow characteristics merge tend to be under-resolved Enright *et al.* (2002); hence, they are more prone to mass losses. Indeed, a linear curvature weight has been adopted by many and demonstrated to produce accurate results in different contexts Luo *et al.* (2015b); Aanjaneya *et al.* (2013). Furthermore,  $\kappa/A_f$  reduces to  $1/A_f$  when the curvature is uniform. Therefore, we can rewrite Eq. (23) using a curvature-dependent speed

$$\mathbf{u}_c(\phi) = \frac{\delta V}{\delta t} \frac{\kappa(\phi)}{A_f} \nabla H_\epsilon(\phi). \quad (25)$$

Clearly, this correction-velocity is larger in highly curved parts, and smaller in flatter parts. It thus includes “local” information while maintaining “global” mass conservation. Standard central-difference discretization applies, where the components of  $\mathbf{u}_c$  can be obtained at either the cell faces or cell centers. The computation of  $\kappa(\phi)$  is crucial and will be presented in the next section. We stress that such a curvature-dependence is not unique. In principle, one can choose different weight-functions, and validate the choice based on the specific applications. Practically, the difference is expected to be negligible since the mass loss remains small (typically around  $10^{-5}$ ) at each correction step.

After correcting the level set on a  $2\epsilon$  band around the interface, a reinitialization step is required to redistribute the values within the entire narrow band ( $2\gamma$ ). The two procedures can be readily combined, since it is not necessary to perform mass correction at every time step. Also, because the formalism is cast in a level set frame, generalization from 2D to 3D is trivial. Comparing with other mass-preserving methods, the additional computational cost of ICLS is small. This is due to the simple algebraic expression of  $\mathbf{u}_c$  (Eq. (25)), and only one solve of Eq. (14) is required; whereas a typical VOF-coupling method involves solving another set of transport equations Sussman & Puckett (2000), or reconstructing the interface by an iterative procedure Luo *et al.* (2015b).

In summary, the ICLS method proceeds by performing the following steps:

1. Advect  $\phi^n$  from time  $t^n$  to  $t^{n+1}$  with Eq. (7), using the flow velocity  $\mathbf{u}^n$ .
2. If reinitialization will be executed (otherwise, go to step 3):
  - (a) Perform mass correction with Eq. (14), using  $\mathbf{u}_c$  from Eq. (25).
  - (b) Reinitialize  $\phi^{n+1}$  with Eq. (11).
3. Exit the level set solver.

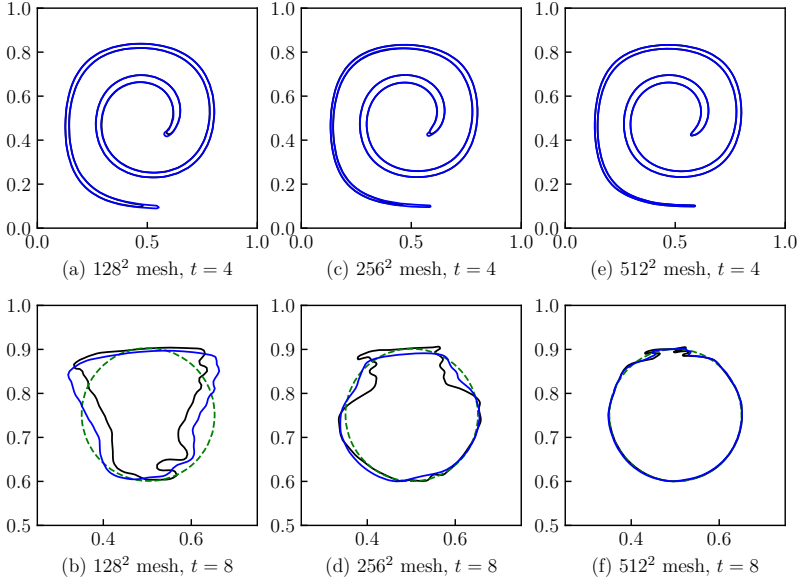


Figure 5: Interface at  $t = 4$  and  $t = 8$  for different meshes. The solid black lines indicate simulations without mass correction, the solid blue lines indicate simulations with the current mass correction method, the green dashed lines in (b)(d)(f) indicate the original circle. (For interpretation of the references to color in this figure legend, the reader is referred to the web version of this article.)

Deforming circle. To assess the performance of ICLS on mass conservation, we test the standard benchmark of a circle deformed by a single vortex. Here, the circle of radius 0.15 is initially centered at  $(x, y) = (0.5, 0.75)$  of a  $[0, 1] \times [0, 1]$  box. The velocity is imposed directly and can be obtained from the stream function

$$\psi(x, y, t) = \frac{1}{\pi} \sin^2(\pi x) \sin^2(\pi y) \cos\left(\frac{\pi t}{T}\right),$$

where  $T$  is traditionally set to 8. Under this flow, the circle will be stretched to maximum at  $t = T/2$  and rewound to its initial condition at  $t = T$ . Although formulated simply, accurately transporting the interface without mass loss is a difficult task.

We perform this test on three different meshes using the complete level set solver: HOUCL5 is used for the level set advection, WENO5 is used for reinitialization every 5 to 20 time steps, the mass correction is performed every 5 to 10 time steps; and the time step is chosen such that  $\Delta t / \Delta x = 0.32$ . Fig. 5 shows the shapes of the filament/circle at  $t = 4$  and  $t = 8$  at various resolutions. From the upper panel, it is clearly seen that the filament has a longer tail

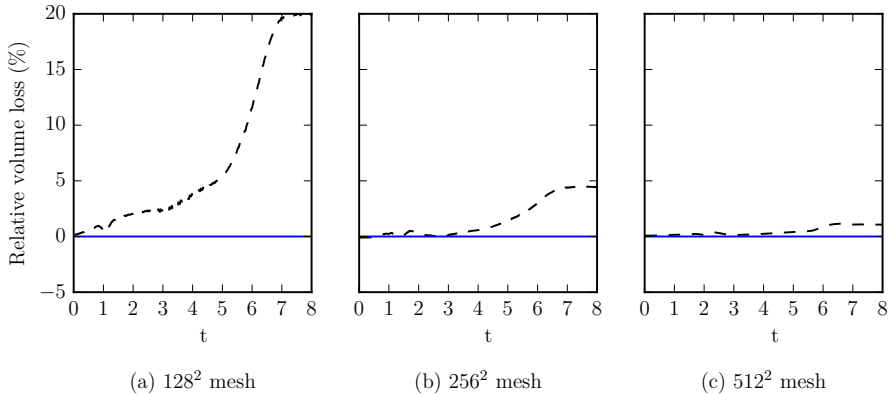


Figure 6: Relative volume loss for three different meshes. Dashed lines indicate simulations without mass correction; solid lines indicate simulations with mass correction.

and head due to mass correction; as we increase the resolution, the difference becomes smaller. The lower panel of Fig. 5 depicts the final shapes, ideally the initial circle if the motion is totally passive. Some artifacts are visible due to the fact that the filament is always under-resolved at the maximum stretching and the level set will automatically merge the characteristics to yield an entropy solution Sethian (1999). We note that the final outcome can be tuned by modifying the frequency of the reinitialization/mass correction, a trade-off between the appearance and the mass loss. However, the objective here is to demonstrate the mass conservation enforced by ICLS, which is clearly illustrated in Fig. 6. For passive transport involving large deformations, we recommend particle-based methods Enright *et al.* (2002). Examples of droplets/bubbles in physical conditions using ICLS will be shown in the validations (Sec. 6.5) and applications (Sec. 7) below.

## 5. Curvature computation

Curvature computation is crucial to interfacial flows in the presence of surface tension, as inaccurate curvature can result in unphysical spurious currents Herrmann (2008); Desjardins *et al.* (2008), and even more so in our case when we apply curvature-dependent interface corrections. In this section, we first briefly describe the calculation of cell-center curvatures; *i.e.*, the curvature evaluated at the same nodal position as the level set function. Then, we introduce a geometric approach for the estimation of interface curvatures corresponding to the zero level set. The second step is specially tailored to the ghost fluid method that will be presented in Sec. 6.2.

### 5.1. Cell-center curvature

From Eq. (6), the curvature  $\kappa$  can be evaluated as

$$\kappa = -\frac{\phi_{yy}\phi_x^2 + \phi_{xx}\phi_y^2 - 2\phi_x\phi_y\phi_{xy}}{(\phi_x^2 + \phi_y^2)^{3/2}} \quad (26)$$

and as

$$\kappa_M = -\frac{\left\{ (\phi_{yy} + \phi_{zz})\phi_x^2 + (\phi_{xx} + \phi_{zz})\phi_y^2 + (\phi_{xx} + \phi_{yy})\phi_z^2 \right.}{\left. -2\phi_x\phi_y\phi_{xy} - 2\phi_x\phi_z\phi_{xz} - 2\phi_y\phi_z\phi_{yz} \right\}}{(\phi_x^2 + \phi_y^2 + \phi_z^2)^{3/2}} \quad (27)$$

in 2D and 3D Cartesian coordinates, respectively, where the subscript  $M$  denotes the mean curvature Sethian (1999). The curvature can be determined from these expressions using simple central finite-differences. It has to be noted, however, that such evaluation of  $\kappa$  involves second derivatives of the level set field  $\phi(\mathbf{x})$ . As a consequence, if the calculation of  $\phi$  is only second-order accurate, the resulting  $\kappa$  will be of order zero. To nonetheless retain a grid converging  $\kappa$ , one can use the compact least-squares scheme proposed by Marchandise *et al.* Marchandise *et al.* (2007). Their approach provides a second-order, grid converging evaluation of the cell-center curvature. It moreover smears out undesired high frequency oscillations possibly introduced by the velocity field. A similar procedure has also been adopted in other works Desjardins *et al.* (2008); Luo *et al.* (2015b).

The principle of the least squares approach is to solve an over-determined linear system,  $\mathbf{Ax} = \mathbf{b}$ , where  $\mathbf{A}$  is a matrix built from the local coordinates,  $\mathbf{x}$  is a unknown array containing the reconstructed level set values and its spatial derivatives, and  $\mathbf{b}$  is the original level set field. The detailed descriptions can be found in Marchandise *et al.* (2007). Here, we only note that the level set function remains unmodified after this step. From a practical point of view, provided the mesh considered is uniform in all directions, the pseudo-inverse of the matrix  $\mathbf{A}$  only needs to be evaluated once and applied close to the interface. Therefore, the computational cost of this least-squares calculation is negligible.

### 5.2. Interface curvature

The least-squares approach described in the previous section only allows one to compute the nodal curvature  $\kappa$  of the level set field  $\phi$ . For computations using the GFM (Sec. 6.2), one might however require an accurate evaluation of the curvature at the exact location of the interface. Provided a grid-converging cell-center curvature, the actual curvature at the interface can be interpolated from its neighboring cells weighted by the level set Francois *et al.* (2006); Luo *et al.* (2015a). Here we present a slightly different but robust algorithm to estimate the interface curvature, with a straight-forward geometrical interpretation.

2D estimation. Suppose the interface  $\Gamma$  cuts through two adjacent cells,  $(i, j)$  and  $(i + 1, j)$ , where the cell-center curvatures  $\kappa_{i,j}$  and  $\kappa_{i+1,j}$  are known.

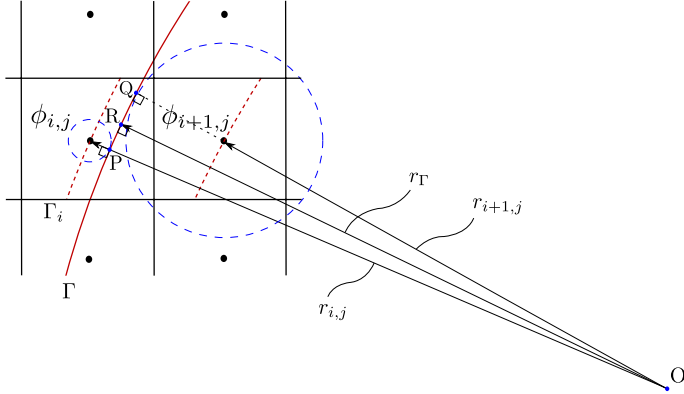


Figure 7: Estimation of the interface's curvature from neighboring cells.

In 2D, we can determine the radius of curvature at each cell directly from

$$\kappa_{i,j} = -\frac{1}{r_{i,j}}, \quad \kappa_{i+1,j} = -\frac{1}{r_{i+1,j}}, \quad (28)$$

as illustrated in Fig. 7. Since the level set is defined as the signed distance to the interface,  $\Gamma$  must be tangent to a circle of radius  $|\phi_{i,j}|$  centered at  $(i,j)$ , and parallel to the contour line of  $\Gamma_i = \{\mathbf{x}|\phi = \phi_{i,j}\}$  (otherwise they will not remain equidistant). We also know  $\Gamma$  lies between  $(i,j)$  and  $(i+1,j)$ , then it must pass through  $P$  (see Fig. 7). Since  $\Gamma$  and  $\Gamma_i$  are parallel and there is only one line normal to both curves passing through  $P$ ,  $r_{i,j}$  and  $OP$  must originate from the same point,  $O$ . Then we get

$$|OP| = r_{i,j} - s_\Gamma \phi_{i,j}. \quad (29)$$

where  $s_\Gamma$  is a sign function equal to 1 if the interface wrapping the negative level set is convex, and equal to  $-1$  if concave.

The same argument holds for cell  $(i+1,j)$ , which yields  $|OQ| = r_{i+1,j} - s_\Gamma \phi_{i+1,j}$ . We can therefore write the radius of the interface curvature between  $(i,j)$  and  $(i+1,j)$  as

$$r_\Gamma = \frac{|OP| + |OQ|}{2}, \quad (30)$$

so that the interface curvature becomes

$$\kappa_\Gamma = \frac{2}{\kappa_{i,j}^{-1} + \kappa_{i+1,j}^{-1} + s_\Gamma(\phi_{i,j} + \phi_{i+1,j})}. \quad (31)$$

The above derivation provides a relation between the interface curvature and that at the adjacent cell-centers in the  $x$  direction. Similar results can be obtained in the  $y$  direction (e.g. between  $\phi_{i,j}$  and  $\phi_{i,j-1}$ ). The assumptions we have made here are 1) the cell-center curvatures are accurate and 2) the

interface curvatures at  $P$  and  $Q$  are the same, so that  $OP$  and  $OQ$  are co-centered (or,  $|OP| \approx |OQ| \approx |OR|$ ). The second assumption is essentially a sub-cell approximation, and we expect it to be valid as long as the interface is well-resolved. One exception we have found is when two interfaces are closer than about  $2\Delta x$ , the local level set field will develop “corners”. In that case, the cell-center curvatures are erroneous and the underlying assumptions we require here are not fulfilled. We do not discuss that case in the present paper. However, we demonstrate in the next section that a second-order convergence is achieved when the interface is resolved.

3D estimation. In three dimensions, the mean curvature of a surface can be written as

$$\kappa_\Gamma = -\left(\frac{1}{r_{\Gamma 1}} + \frac{1}{r_{\Gamma 2}}\right), \quad (32)$$

where  $r_{\Gamma 1}$  and  $r_{\Gamma 2}$  are the two principal radii corresponding to the maximal and minimal planar radius of curvature. Note that we do not need to approximate the interface as a sphere since there is always a plane where the previous picture (Fig. 7) holds. Under the same assumption as for the 2D case, that the interface at  $P$  and  $Q$  have the same principal radii (hence the same curvature), one can again relate the nodal curvatures to their nearby interface as

$$\begin{aligned} \kappa_{i,j,k} &= -\left(\frac{1}{r_{\Gamma 1} + s_\Gamma \phi_{i,j,k}} + \frac{1}{r_{\Gamma 2} + s_\Gamma \phi_{i,j,k}}\right), \\ \kappa_{i+1,j,k} &= -\left(\frac{1}{r_{\Gamma 1} + s_\Gamma \phi_{i+1,j,k}} + \frac{1}{r_{\Gamma 2} + s_\Gamma \phi_{i+1,j,k}}\right), \end{aligned} \quad (33)$$

where  $s_\Gamma$  is the same sign function defined for the 2D case. Comparing equations (32) and (33), it is natural to expand Eq. (33) into a Taylor series and to approximate the interface curvature directly as

$$\kappa_\Gamma = \frac{\epsilon_{i+1}\kappa_i - \epsilon_i\kappa_{i+1}}{\epsilon_{i+1} - \epsilon_i} + O(\epsilon_i^2, \epsilon_{i+1}^2), \quad (34)$$

where

$$\epsilon_i = s_\Gamma \phi_{i,j,k}. \quad (35)$$

Since the level set must change sign across the interface, Eq. (34) is always defined and it reduces to the exact value if the cell center happens to be on the interface. Similarly, the whole procedure is repeated in the  $y$  and  $z$  directions.

Finally, in order to ensure a robust estimation, we perform an additional quadratic least squares approximation on the curvature field near the interface, similar to Marchandise *et al.* (2007). This procedure takes place before the 3D estimation (Eq. (34)), and essentially improves the accuracy of cell-center curvatures by removing possible high-frequency noise. We note that the second averaging is optional, and different methods can be found in literature to evaluate the cell-center curvatures du Chéné *et al.* (2008). In the present paper, the least squares approach mentioned in Sec. 5.1 is used for all the cases.

To assess the accuracy of our interface curvature estimation, we calculate the  $L_\infty$  norm of a circle/sphere of radius 0.25 centered in a unit square/cube.

Table 1: Grid convergence of the current interface curvature calculation in both 2D and 3D.

Points per diameter	16	32	48	64
$L_\infty$ 2D	$1.144 \times 10^{-2}$	$2.904 \times 10^{-3}$	$1.285 \times 10^{-3}$	$7.227 \times 10^{-4}$
$L_\infty$ 3D	$1.527 \times 10^{-2}$	$3.888 \times 10^{-3}$	$1.732 \times 10^{-3}$	$9.753 \times 10^{-4}$

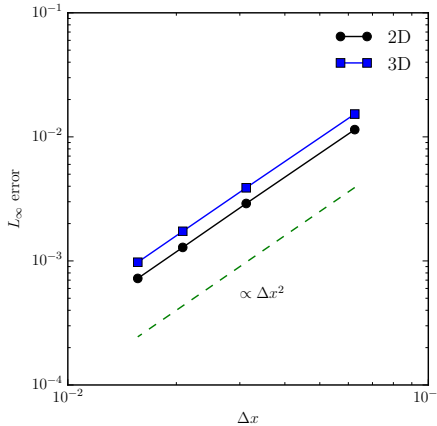


Figure 8: Second order convergence of the interface curvature computation in both 2D and 3D.

Table 1 summarizes the error after one step of the calculations on different resolutions, which are also plotted in Fig. 8. Clearly, second-order convergence is achieved in both 2D and 3D cases.

## 6. Solution of the Navier-Stokes equations

In this section, we outline the flow solver developed from that of Breugem (2012) for particle-laden flows. After advancing the level set from  $\phi^n$  to  $\phi^{n+1}$ , the density and viscosity fields are updated by

$$\rho^{n+1} = \rho_1 H_s(\phi^{n+1}) + \rho_2(1 - H_s(\phi^{n+1})), \quad (36a)$$

$$\mu^{n+1} = \mu_1 H_s(\phi^{n+1}) + \mu_2(1 - H_s(\phi^{n+1})), \quad (36b)$$

where

$$H_s(\phi) = \begin{cases} 1 & \text{if } \phi > 0 \\ 0 & \text{otherwise,} \end{cases} \quad (37)$$

is a simple step function.

Next, a prediction velocity  $\mathbf{u}^*$  is computed by defining  $\mathbf{RU}^n$  as

$$\mathbf{RU}^n = -\nabla \cdot (\mathbf{u}^n \mathbf{u}^n) + \frac{1}{Re} \left( \frac{1}{\rho^{n+1}} \nabla \cdot [\mu^{n+1} (\nabla \mathbf{u}^n + (\nabla \mathbf{u}^n)^T)] \right) + \frac{1}{Fr} \mathbf{g}, \quad (38)$$

which is the right-hand side of the momentum equation (1b) excluding the pressure gradient term. Integrating in time with the second-order Adams-Bashforth scheme (AB2) yields

$$\mathbf{u}^* = \mathbf{u}^n + \Delta t \left( \frac{3}{2} \mathbf{RU}^n - \frac{1}{2} \mathbf{RU}^{n-1} \right). \quad (39)$$

To enforce a divergence-free velocity field (Eq. (1a)), we proceed by solving the Poisson equation for the pressure as in the standard projection method Chorin (1968), *i.e.*

$$\nabla \cdot \left( \frac{1}{\rho^{n+1}} \nabla p^{n+1} \right) = \frac{1}{\Delta t} \nabla \cdot \mathbf{u}^*. \quad (40)$$

The surface tension between two fluids is also computed during this step, using the ghost fluid method Fedkiw *et al.* (1999) (Sec. 6.2). This allows for an accurate and sharp evaluation of the pressure jump even at large density contrasts Desjardins *et al.* (2008). Finally, the velocity at the next time level is updated as

$$\mathbf{u}^{n+1} = \mathbf{u}^* - \frac{\Delta t}{\rho^{n+1}} \nabla p^{n+1}. \quad (41)$$

### 6.1. Fast pressure-correction method

In the above outline, a Poisson equation for the pressure (Eq. (40)) must be solved at each time step. This operation takes most of the computational time in the projection method, as it is usually solved iteratively. In addition, the operation count of iterative methods depends on the problem parameters (e.g. density ratio) and the convergence tolerance Dodd & Ferrante (2014). On the other hand, Dong and Shen Dong & Shen (2012) recently developed a velocity-correction method that transforms the variable-coefficient Poisson equation into a constant-coefficient one. The essential idea is to split the pressure gradient term in Eq. (40) in two parts, one with constant coefficients, the other with variable coefficients, *i.e.*

$$\frac{1}{\rho^{n+1}} \nabla p^{n+1} \rightarrow \frac{1}{\rho_0} \nabla p^{n+1} + \left( \frac{1}{\rho^{n+1}} - \frac{1}{\rho_0} \right) \nabla \hat{p}, \quad (42)$$

where  $\rho_0 = \min(\rho_1, \rho_2)$  and  $\hat{p}$  is the approximate pressure at time level  $n + 1$ . This splitting reduces to the exact form of Eq. (40) within the lower-density phase, while its validity in the higher-density phase and at the interface depends on the choice of  $\hat{p}$ . Later, Dodd and Ferrante Dodd & Ferrante (2014) showed that by explicitly estimating  $\hat{p}$  from two previous time levels as

$$\hat{p} = 2p^n - p^{n-1}, \quad (43)$$

the resulting velocity field in Eq. (41) will be second-order accurate in both space and time, independent of the interface advection method. Furthermore, if the computational domain includes periodic boundaries or can be represented by certain combination of homogeneous Dirichlet/Neumann conditions Schumann & Sweet (1988), the constant-coefficient part of Eq. (42) can be solved directly using Gauss elimination in the Fourier space. Such a FFT-based solver can lead to a speed-up of 10 – 40 times, thus the name fast pressure-correction method (FastP\*). Following this approach, Eqs. (40) and (41) are modified as

$$\nabla^2 p^{n+1} = \nabla \cdot \left[ \left( 1 - \frac{\rho_0}{\rho^{n+1}} \right) \nabla \hat{p} \right] + \frac{\rho_0}{\Delta t} \nabla \cdot \mathbf{u}^* \quad (44)$$

and

$$\mathbf{u}^{n+1} = \mathbf{u}^* - \Delta t \left[ \frac{1}{\rho_0} \nabla p^{n+1} + \left( \frac{1}{\rho^{n+1}} - \frac{1}{\rho_0} \right) \nabla \hat{p} \right]. \quad (45)$$

## 6.2. Ghost fluid method

As discussed before, surface tension is commonly computed using the continuum surface force (CSF) model Brackbill *et al.* (1992), in which the pressure jump across an interface is represented as a forcing term on the right-hand side of Eq. (1b). Despite its simplicity, CSF introduces an unfavorable smearing in the density and pressure profiles, resulting in an artificial spreading of the interface (typically over a thickness of  $3\Delta x$ ). An alternative approach is the so-called ghost fluid method (GFM), originally developed by Fedkiw *et al.* Fedkiw *et al.* (1999) to capture the boundary conditions in the inviscid compressible Euler equations. Unlike CSF, GFM enables a numerical discretization of the gradient operator while preserving the discontinuity of the differentiated quantity. It was extended to viscous flows by Kang *et al.* Kang *et al.* (2000) and has been successfully utilized in multiphase flow simulations, see e.g. Desjardins *et al.* (2008); Coyajee & Boersma (2009); Tanguy & Berlemont (2005).

Recall from Eq. (2) that the pressure jump has two components, one arising from the surface tension, the other from the viscosity difference of the two fluids. In Kang *et al.* (2000), a complete algorithm is provided to compute the two contributions, making the density, viscosity, and pressure all sharp. However, having a sharp viscosity profile requires an extra step to evaluate the divergence of the deformation tensor (see Eq. (38)). That is, for cells adjacent to the interface, the second derivatives of the velocity must be evaluated using the techniques developed in Liu *et al.* (2000); Kang *et al.* (2000). However, rewriting Eq. (2) as

$$[p]_\Gamma = \frac{1}{Re} \left( \frac{\kappa}{Ca} + 2[\mu]_\Gamma \mathbf{n}^T \cdot \nabla \mathbf{u} \cdot \mathbf{n} \right), \quad (46)$$

reveals that surface tension is the dominant term when the Capillary number,  $Ca = We/Re$ , is small. For the applications we are interested in, e.g. colloidal droplets in microfluidic channels,  $Ca$  is of the order of  $10^{-5}$ . Therefore, in the

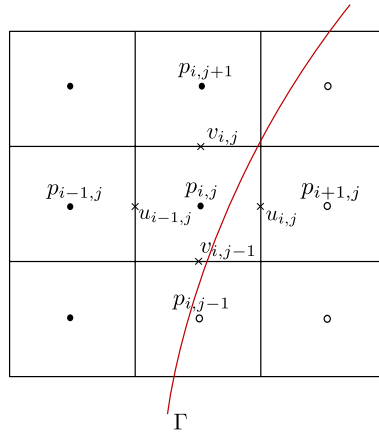


Figure 9: Schematic of the 2D staggered grid where pressure locates at cell centers and velocity components locate at cell faces. The curved line specifies the interface  $\Gamma$ ; filled and empty circles indicate discontinuous pressure (or density) values in phase 1 and 2, respectively.

present implementation, we regularize the viscosity profile (*i.e.* replacing  $H_s(\phi)$  in Eq. (36b) with  $H_\epsilon(\phi)$  in Eq. (18)) and use GFM only for the pressure jump.

### 6.2.1. Spatial discretization

Eqs. (38), (44), and (45) are discretized on a standard staggered grid using a second-order conservative finite volume method. It is equivalent to central differences in all three directions if the mesh is uniform. A detailed description of the discretization of the individual terms can be found in Dodd & Ferrante (2014), Sec. 2.2.1. For brevity, we show here only the 2D evaluations of  $\nabla p$  and  $\nabla^2 p$  due to GFM.

As sketched in Fig. 9, computing  $\nabla^2 p$  at node  $(i, j)$  requires three entries of  $p$  in each direction. If CSF is used, all gradient terms can be evaluated with the straightforward central-difference, *i.e.*

$$(\nabla^2 p)_{i,j} = \frac{p_{i-1,j}^s - 2p_{i,j}^s + p_{i+1,j}^s}{\Delta x^2} + \frac{p_{i,j-1}^s - 2p_{i,j}^s + p_{i,j+1}^s}{\Delta y^2}. \quad (47)$$

However, the pressure at the cells adjacent to the interface will have to be smeared out; hence we denote them with  $p^s$ . In order for the pressure to be sharp, GFM creates an artificial fluid (the “ghost” fluid) and assumes that the discontinuity can be extended beyond the physical interface. That is, if we know the corresponding jumps of pressure, then its derivatives can be evaluated without smearing by removing such jumps. For the particular case depicted in Fig. 9, Eq. (47) can be re-written as (see Liu *et al.* (2000) for the intermediate

steps)

$$(\nabla^2 p)_{i,j} = \frac{p_{i-1,j} - 2p_{i,j} + p_{i+1,j}}{\Delta x^2} - \frac{[p]_{i,j}}{\Delta x^2} - \frac{1}{\Delta x} \left[ \frac{\partial p}{\partial x} \right]_{i+1/2,j} + \frac{p_{i,j-1} - 2p_{i,j} + p_{i,j+1}}{\Delta y^2} - \frac{[p]_{i,j-1}}{\Delta y^2}, \quad (48)$$

where we recall  $[ \cdot ]_{i,j}$  denotes the discontinuity from fluid 1 to fluid 2 at cell  $(i,j)$  (same for  $[ \cdot ]_{i,j-1}$ , etc.).

To determine the jump terms in Eq. (48), we first note that the velocity and its material derivatives across the interface of viscous flows are continuous Kang *et al.* (2000); Desjardins *et al.* (2008), resulting in

$$\left[ \frac{1}{\rho^{n+1}} \nabla p^{n+1} \right]_\Gamma = \mathbf{0}. \quad (49)$$

Furthermore, owing to the splitting that allows us to solve only for a constant-coefficient Poisson equation (Eq. (44)), Eqs. (42) and (49) lead to

$$\left[ \frac{1}{\rho_0} \nabla p^{n+1} \right]_\Gamma + \left[ \left( \frac{1}{\rho^{n+1}} - \frac{1}{\rho_0} \right) \nabla \hat{p} \right]_\Gamma = \mathbf{0}, \quad (50)$$

which also implies that the pressure gradient terms are continuous everywhere (e.g. the subscript can be  $(i+1/2, j)$ ), along any direction.

Denoting the right-hand side of Eq. (44) as  $RP$ , it is discretized as

$$RP_{i,j} = \left( \left( 1 - \frac{\rho_0}{\rho_{i+1/2,j}^{n+1}} \right) \frac{\partial \hat{p}}{\partial x}_{i+1/2,j} - \left( 1 - \frac{\rho_0}{\rho_{i-1/2,j}^{n+1}} \right) \frac{\partial \hat{p}}{\partial x}_{i-1/2,j} \right) / \Delta x + \left( \left( 1 - \frac{\rho_0}{\rho_{i,j+1/2}^{n+1}} \right) \frac{\partial \hat{p}}{\partial y}_{i,j+1/2} - \left( 1 - \frac{\rho_0}{\rho_{i,j-1/2}^{n+1}} \right) \frac{\partial \hat{p}}{\partial y}_{i,j-1/2} \right) / \Delta y - \frac{1}{\Delta x} \left[ \left( 1 - \frac{\rho_0}{\rho^{n+1}} \right) \frac{\partial \hat{p}}{\partial x} \right]_{i+1/2,j} + \frac{\rho_0}{\Delta t} \left( \frac{u_{i,j}^* - u_{i-1,j}^*}{\Delta x} + \frac{v_{i,j}^* - v_{i,j-1}^*}{\Delta y} \right), \quad (51)$$

again using GFM Liu *et al.* (2000). Comparing Eqs. (48) and (51), we note that the jump of the first derivatives cancels out recognizing Eq. (50). With a modified right-hand side,  $RP^*$ , defined as

$$RP_{i,j}^* = RP_{i,j} + \frac{1}{\Delta x} \left[ \left( 1 - \frac{\rho_0}{\rho^{n+1}} \right) \frac{\partial \hat{p}}{\partial x} \right]_{i+1/2,j}, \quad (52)$$

the discrete form of Eq. (44) reduces to

$$\frac{p_{i-1,j}^{n+1} - 2p_{i,j}^{n+1} + p_{i+1,j}^{n+1}}{\Delta x^2} + \frac{p_{i,j-1}^{n+1} - 2p_{i,j}^{n+1} + p_{i,j+1}^{n+1}}{\Delta y^2} = \frac{[p]_{i,j}^{n+1}}{\Delta x^2} + \frac{[p]_{i,j-1}^{n+1}}{\Delta y^2} + RP_{i,j}^*. \quad (53)$$

Eq. (53) is still not ready to solve, since the pressure jumps for the first point away from the interface (e.g.  $[p]_{i,j}^{n+1}$ ) are not known. Following Desjardins

*et al.* (2008), we perform a Taylor series expansion around  $\Gamma$ ,

$$[p]_{i,j}^{n+1} = [p]_{\Gamma}^{n+1} + (x_i - x_{\Gamma}) \left[ \frac{\partial p}{\partial x} \right]_{\Gamma}^{n+1} + O((x_i - x_{\Gamma})^2), \quad (54)$$

where  $[p]_{\Gamma}^{n+1} = \kappa_{\Gamma,x}/We$ , and  $\kappa_{\Gamma,x}$  is estimated from Eq. (31) in 2D and from Eq. (34) in 3D, along the  $x$  direction using  $\phi_{i,j}^{n+1}$  and  $\phi_{i+1,j}^{n+1}$ . The jump of the pressure gradient at the interface can be similarly expanded at  $(i,j)$

$$\left[ \frac{\partial p}{\partial x} \right]_{\Gamma}^{n+1} = \left[ \frac{\partial p}{\partial x} \right]_{i,j}^{n+1} + O(x_{\Gamma} - x_i), \quad (55)$$

resulting in

$$[p]_{i,j}^{n+1} = \frac{\kappa_{\Gamma,x}}{We} + (x_i - x_{\Gamma}) \left[ \frac{\partial p}{\partial x} \right]_{i,j}^{n+1} + O((x_i - x_{\Gamma})^2). \quad (56)$$

Using Eq. (50), we can re-write Eq. (56) as

$$[p]_{i,j}^{n+1} = \frac{\kappa_{\Gamma,x}}{We} + (x_i - x_{\Gamma}) \left[ \left(1 - \frac{\rho_0}{\rho^{n+1}}\right) \frac{\partial \hat{p}}{\partial x} \right]_{i,j} + O((x_i - x_{\Gamma})^2), \quad (57)$$

where the jump term on the right-hand side can be explicitly calculated using the family of identities of the form Kang *et al.* (2000)

$$[AB] = [A]\tilde{B} + \tilde{A}[B], \quad \tilde{A} = aA_1 + bA_2, \quad a + b = 1. \quad (58)$$

Although Eqs. (57) and (58) lead to a second-order pressure jump, it is much simpler to keep only the leading-order term, *i.e.*

$$[p]_{i,j}^{n+1} = \frac{\kappa_{\Gamma,x}}{We} + O(x_i - x_{\Gamma}). \quad (59)$$

This way, the pressure jump varies only with the local curvature, remains invariant across the interface, and is second-order accurate when the density is uniform. For the test cases shown below, Eq. (59) is used. Thus, the complete discretization of Eq. (44) reads

$$\frac{p_{i-1,j}^{n+1} - 2p_{i,j}^{n+1} + p_{i+1,j}^{n+1}}{\Delta x^2} + \frac{p_{i,j-1}^{n+1} - 2p_{i,j}^{n+1} + p_{i,j+1}^{n+1}}{\Delta y^2} = \frac{1}{We} \left( \frac{\kappa_{\Gamma,x}}{\Delta x^2} + \frac{\kappa_{\Gamma,y}}{\Delta y^2} \right) + RP_{i,j}^*, \quad (60)$$

with  $RP_{i,j}^*$  defined in Eq. (52) corresponding to Fig. 9.

Clearly, the resulting linear system (Eq. (60)) has a standard positive definite, symmetric coefficient matrix, and it can be solved directly using the FFT-based fast Poisson solver (Sec. 6.1). Care should be exercised when a nodal point crosses the interface in more than one direction. In those cases, the interface curvature of each crossing direction may be different and it shall not be averaged. Otherwise, the projection (Eq. (44)) and correction (Eq. (45)) steps can become inconsistent, making the velocity not divergence-free. Additionally,

when taking the gradient of the pressure-correction term; e.g. its derivative along the  $x$  direction, the correct discretization should be

$$\frac{\partial \hat{p}}{\partial x_{i,j}} = \frac{(\hat{p}_{i+1,j} - (2[p]_{i+1,j}^n - [p]_{i+1,j}^{n-1})) - \hat{p}_{i,j}}{\Delta x}. \quad (61)$$

After removing the jump, the divergence of the bracket term in Eq. (44) is evaluated in the same way as in Dodd & Ferrante (2014).

Finally, we can re-write Eqs. (44) and (45) compactly as

$$\nabla^2 p^{n+1} = \nabla_g^2 [p]_\Gamma + \nabla \cdot \left[ \left( 1 - \frac{\rho_0}{\rho^{n+1}} \right) \nabla_g \hat{p} \right] + \frac{\rho_0}{\Delta t} \nabla \cdot \mathbf{u}^*, \quad (62)$$

$$\mathbf{u}^{n+1} = \mathbf{u}^* - \Delta t \left[ \frac{1}{\rho_0} \nabla_g p^{n+1} + \left( \frac{1}{\rho^{n+1}} - \frac{1}{\rho_0} \right) \nabla_g \hat{p} \right]. \quad (63)$$

where  $\nabla_g$  and  $\nabla_g^2 [p]_\Gamma$  denote, respectively, the gradient operator considering the jump and the extra jump terms from the laplacian operator due to GFM.

### 6.3. Time integration

In the current work, a second-order accurate Adams-Bashforth scheme is used for the time integration. The time step is restricted by convection, diffusion, surface tension, and gravity, due to our explicit treatment of these terms. As suggested in Kang *et al.* (2000), the overall time step restriction is

$$\Delta t \leq 1 / \left( C_{CFL} + V_{CFL} + \sqrt{(C_{CFL} + V_{CFL})^2 + 4G_{CFL}^2 + 4S_{CFL}^2} \right), \quad (64)$$

where  $C_{CFL}$ ,  $V_{CFL}$ ,  $G_{CFL}$ , and  $S_{CFL}$  are the “speeds” due to convection, viscosity, gravity, and surface tension, respectively. Specifically, they are given as

$$C_{CFL} = \frac{|u|_{max}}{\Delta x} + \frac{|v|_{max}}{\Delta y} + \frac{|w|_{max}}{\Delta z}, \quad (65)$$

$$V_{CFL} = \frac{1}{Re} \max \left( \frac{\mu_1}{\rho_1}, \frac{\mu_2}{\rho_2} \right) \left( \frac{2}{\Delta x^2} + \frac{2}{\Delta y^2} + \frac{2}{\Delta z^2} \right), \quad (66)$$

$$G_{CFL} = \sqrt{\frac{1}{Fr} \frac{|(1 - \frac{\rho_1 + \rho_2}{2\rho})g|_{max}}{\min(\Delta x, \Delta y, \Delta z)}}, \quad (67)$$

$$S_{CFL} = \sqrt{\frac{1}{We} \frac{|\kappa|_{max}}{\min(\rho_1, \rho_2) [\min(\Delta x, \Delta y, \Delta z)]^2}}. \quad (68)$$

where  $|\kappa|_{max}$  in (68) can be approximated by  $1/\Delta x$  in 2D and  $2/\Delta x$  in 3D, assuming  $\Delta x$  is the smallest grid spacing.

The reasons we choose an explicit temporal scheme rather than an implicit one are twofold. First, for applications involving a large density and viscosity

contrast, the stability restriction imposed by surface tension is usually greater than that imposed by diffusion. Second, an implicit formulation of GFM has been admitted to be challenging to develop Desjardins *et al.* (2008), and it was shown in a recent study Denner & Wachem (2015) that a capillary time-step constraint exists, irrespective of the type of implementation, due to the temporal sampling of surface capillary waves. Fortunately, the fast pressure-correction method enables the use of FFT for the constant-coefficient Poisson equation and hence an accurate and fast solution of the two-fluid Navier-Stokes equation can be obtained.

#### 6.4. Full solution procedure

We summarize the full solution procedure as follows:

1. Advance the interface explicitly from  $\phi^n$  to  $\phi^{n+1}$  using the ICLS, and update the density  $\rho^{n+1}$  and the viscosity  $\mu^{n+1}$ .
2. Advance the velocity field explicitly from  $\mathbf{u}^n$  to  $\mathbf{u}^*$  with Eqs. (38) and (39).
3. Project the velocity field by solving the constant-coefficient Poisson Eq. (62) making use of the FastP\* and the GFM.
4. Update the velocity from  $\mathbf{u}^*$  to  $\mathbf{u}^{n+1}$  explicitly with Eq. (63), again using the FastP\* and the GFM.

#### 6.5. Validations

In this section, we validate the coupled ICLS/NS solver using three benchmark examples with increasing complexities. Specifically, the first example verifies the discrete momentum balance for fluids of the same density and viscosity. This concerns the surface tension computed by the GFM using interface curvatures. Then, the density and viscosity ratios are significantly increased (up to  $10^4$ ) to test the combined FastP\* and GFM. Using the same test, we also provide a convergence check of the complete flow solver. Finally, the overall accuracy is assessed by simulating a 3D bubble in comparison with experiments.

##### 6.5.1. Spurious currents

A common problem in multiphase-flow simulations is the artificial velocity generated at the fluid interface due to errors in the curvature computation. To access the significance of such spurious currents, we test a stationary droplet of diameter  $D = 0.4$  placed at the center of a unit box. The surface tension between the inner and outer fluid is  $\sigma = 1$ , the viscosity is uniformly  $\mu = 0.1$ , and the density ratio is 1. By changing the density  $\rho$  of both fluids, the Laplace number  $La = \sigma\rho D/\mu^2$  can be varied. The spurious currents are thus determined from the resulting capillary number  $Ca = |U_{max}|\mu/\sigma$  at a non-dimensional time  $t\sigma/(\mu D) = 250$ . Here, we compare the results on a  $32 \times 32$  mesh with the GFM implementation by Desjardins *et al.* (2008). As listed in Table 2, the capillary numbers from both tests remain very small for all the Laplace numbers, with the present results being one-order smaller.

Table 2: Dependence of spurious current capillary number  $Ca$  on the Laplace number for a static droplet with surface tension on a  $32 \times 32$  mesh in comparison with Desjardins *et al.* (2008).

La	12	120	1,200	12,000	120,000	1,200,000
Ca	$2.85 \times 10^{-6}$	$3.14 \times 10^{-6}$	$3.63 \times 10^{-6}$	$3.87 \times 10^{-6}$	$3.41 \times 10^{-6}$	$5.79 \times 10^{-7}$
Ca (ref)	$4.54 \times 10^{-5}$	$3.67 \times 10^{-5}$	$3.62 \times 10^{-5}$	$4.15 \times 10^{-5}$	$3.75 \times 10^{-5}$	$8.19 \times 10^{-6}$

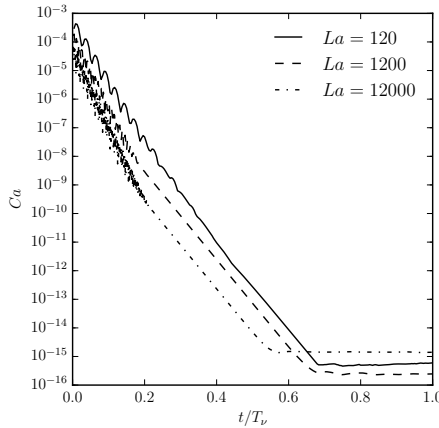


Figure 10: Temporal evolution of the spurious currents without performing level set reinitialization at three Laplace numbers as in Popinet (2009).

We also note that the spurious currents reported in Table 2 are obtained by performing the level set reinitialization at about every 100 time steps. However, if we turn off the reinitialization, such spurious velocity will eventually go to machine zero, as shown in Fig. 10, where time is non-dimensionalized with the viscous time scale,  $T_\nu = \rho D^2 / \mu$ . The nearly exponential decay of  $Ca$  and the collapsing of the three curves are the result of the viscous damping of the spurious velocity, as the shape of droplet relaxes to its numerical equilibrium. Similar results are obtained and explained in greater detail in Popinet (2009) using a balanced-force continuum-surface-force surface-tension formulation and the VOF. The result in Fig. 10 therefore validates the computation of the surface tension with the GFM.

### 6.5.2. Capillary wave

To verify the solver at large density and (dynamic) viscosity contrasts, we simulate a small-amplitude capillary wave for which there exists an analytical solution derived by Prosperetti (1981). Specifically, an initially

Table 3: Temporal and spatial convergence rates for the velocity component  $u$  and the pressure  $p$ .

	$L_2^{4\Delta t, 2\Delta t}$	$L_2^{2\Delta t, \Delta t}$	Rate	$L_2^{4\Delta x, 2\Delta x}$	$L_2^{2\Delta x, \Delta x}$	Rate
$u$	$2.46 \times 10^{-8}$	$1.03 \times 10^{-8}$	1.19	$2.16 \times 10^{-7}$	$5.95 \times 10^{-8}$	1.82
$p$	$1.13 \times 10^{-6}$	$3.85 \times 10^{-7}$	1.46	$3.25 \times 10^{-3}$	$6.11 \times 10^{-4}$	2.67

sinusoidal interface is imposed between two immiscible, viscous fluids of infinite depth and lateral extent. When the lower fluid is heavier, the balance between inertia, viscosity, and surface tension results in a decaying free-surface wave. By requiring matching kinematic viscosity  $\nu_u = \nu_l$  ( $u$  for upper,  $l$  for lower), the solution of the wave amplitude in terms of Laplace transforms can be inverted analytically and compared with the simulation results.

We set up our simulation in the same way as suggested in Dodd & Ferrante (2014). Here, two fluids of equal depth are placed in a  $1 \times 3$  ( $64 \times 192$  grid points) domain, where the streamwise direction ( $L = 1$ ) is periodic and the vertical direction ( $H = 3$ ) wall-bounded. The interface has an initial wavelength of  $\lambda = 1$  and an amplitude of  $a_0 = 0.01$ . With varying density ratios  $\rho_l/\rho_u$ , the non-dimensional parameters for the test are

$$Re = 100, \quad We = 1, \quad Fr = \infty, \quad \rho_l/\rho_u = 10 - 10,000, \quad \nu_l = \nu_u. \quad (69)$$

The CFL number  $\Delta t/\Delta x$  is  $2.5 \times 10^{-2}$  for  $\rho_l/\rho_u = 10$  and  $10^2$ , and it is reduced to  $2.5 \times 10^{-3}$  for  $\rho_l/\rho_u = 10^3$  and  $2.5 \times 10^{-4}$  for  $\rho_l/\rho_u = 10^4$ .

Fig. 11 shows the temporal evolution of the wave amplitude up to  $t = 10$ . The excellent agreement with Prosperetti's analytical solution Prosperetti (1981) confirms the normal stress balance computed using the GFM. And accurate results at very large density contrasts are realized by combining the FastP\* with GFM. Note that the dynamic viscosity ratio  $\mu_l/\mu_u$  also varies from 10 to  $10^4$ . However, neglecting its contribution to the pressure jump by regularizing the viscosity profile yields accurate results since the Capillary number is small ( $Ca = We/Re = 0.01$ ), as discussed in conjunction with Eq. (46).

### 6.5.3. Convergence

We continue to check the temporal and spatial convergence rates of the coupled ICLS/NS solver. Here, the same test problem as in Sec. 6.5.2 is used, with the non-dimensional parameters given as

$$Re = 500, \quad We = 1, \quad Fr = \infty, \quad H_0 = 0.05, \quad \rho_l/\rho_u = 20, \quad \mu_l/\mu_u = 20, \quad (70)$$

again following Dodd & Ferrante (2014). Placing the fluids in a  $1 \times 1$  box, the flow is simulated under different time steps or on different meshes so that the errors can be computed between successive solutions.

Table 3 shows the convergence rates for the velocity component  $u$  and the pressure  $p$  in the  $L_2$  norm. Here, the temporal convergence is evaluated at

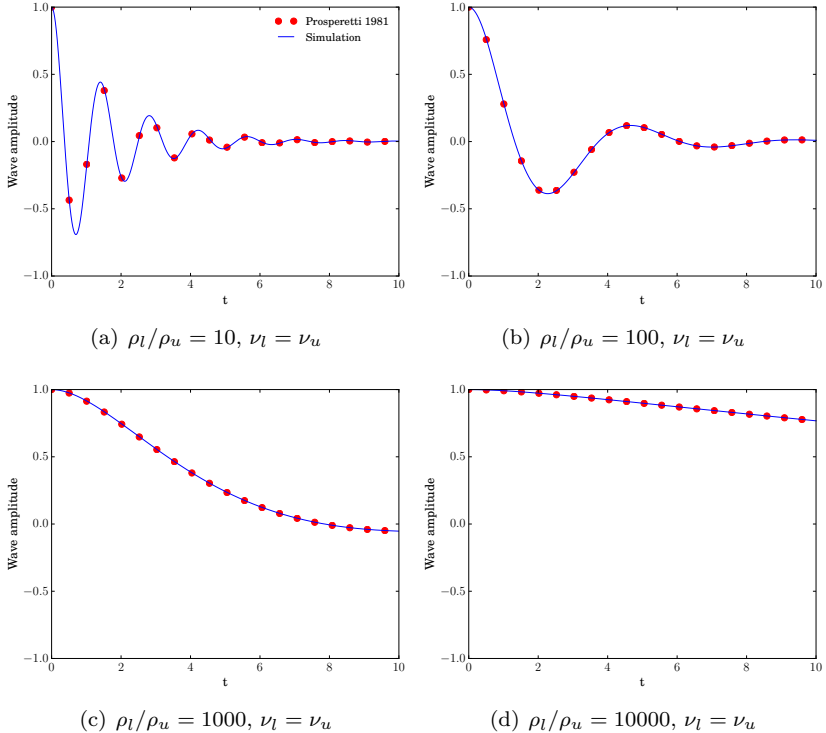


Figure 11: Time development of the capillary wave amplitude (normalized to  $a_0$ ) for increasing density ratios and matching kinematic viscosity in comparison with Prosperetti's analytical solution Prosperetti (1981).

$t = 6.25 \times 10^{-2}$  on a  $256^2$  grid, by increasing the time step from  $\Delta t = 4.88 \times 10^{-5}$  to  $2\Delta t$  and  $4\Delta t$ . Two iterations of reinitialization are performed every 25 – 100 time steps. The observed convergence rates for both velocity and pressure is between first and second order. Considering that we use RK3 for LS and AB2 for NS, the reduced convergence is probably due to the reinitialization that perturbs the interface. Changing the frequency of the reinitialization, we indeed observe different convergence rates (they can also exceed second order if the density ratio is 1, not shown). Next, the spatial convergence is obtained by successively refining the grid from  $32^2$  to  $64^2$  to  $128^2$ . Using the same time step  $\Delta t = 4.88 \times 10^{-5}$  and interpolating the solution to the coarse grid after one solve, the results display nearly second order convergence for the velocity and a super-convergence for the pressure. We note that the GFM has been proven convergent (but without a rate) for variable-coefficient Poisson equations Liu & Sideris (2003). Our results thus show improved accuracy in two fluid problems,

when a constant-coefficient Poisson equation is obtained by combining the GFM with the FastP\*.

#### 6.5.4. Rising bubble

Finally, we compute four cases of a rising bubble to access the overall accuracy of the current ICLS/NS solver in 3D in the presence of moderate deformations. Originally documented by Grace Grace (1973), it was observed that a single gas bubble rising in quiescent liquid has four characteristic shapes: spherical, ellipsoidal, skirted, or dimpled. The governing non-dimensional numbers are the Morton number  $M$ , Eotvos number  $Eo$  (sometimes referred to as the Bond number), and the terminal Reynolds number  $Re_t$ , defined as

$$M = \frac{g\mu_l^4}{\rho_l\sigma^3}, \quad Eo = \frac{\Delta\rho gd^2}{\sigma}, \quad Re_t = \frac{\rho_l U_\infty d}{\mu_l}, \quad (71)$$

where  $d$  is the bubble diameter,  $\Delta\rho$  is the density difference,  $U_\infty$  is the terminal velocity of the bubble, and the subscripts  $l$  and  $g$  denote, in order, the liquid and gas phase. The Morton and Eotvos number are defined purely by the material properties of the chosen fluids, while the terminal Reynolds number provides a measure of the steady-state bubble velocity.

Table 4 lists the four representative cases we select for the simulations. A spherical bubble of diameter  $d = 1$  is centered in a domain of size  $(L_x \times L_y \times L_z) = (3d \times 6d \times 3d)$ . A grid of  $96 \times 192 \times 96$  points is used, giving the bubble an initial resolution of 32 points per diameter. Periodic boundary conditions are imposed in the  $x$  (spanwise) and  $y$  (rising) directions whereas no friction, no penetration is enforced in the  $z$  direction. As suggested by Annaland *et al.* Annaland *et al.* (2005), a ratio of 100 between the density and viscosity of liquid and gas is sufficiently high to approximate such gas-liquid systems, leading to  $\Delta\rho \approx \rho_l$ .  $Re$  and  $We$  in Eq. (3) can thus be obtained from  $M$  and  $Eo$  as

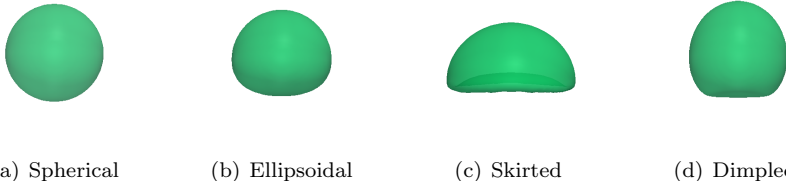
$$Re = \left( \frac{Eo^3}{M} \right)^{1/4}, \quad We = Eo. \quad (72)$$

The CFL number,  $\Delta t / \Delta x$ , is  $1.6 \times 10^{-4}$  for cases (a), (b), and (d), and  $1.6 \times 10^{-3}$  for case (c). The simulation is integrated in time up to  $t = 10$  to ensure the bubble reaches nearly steady state.

The results of the bubble terminal velocities are presented in Table 4. The difference between the computed Reynolds,  $Re_C$ , and the terminal Reynolds,  $Re_G$ , measured by Grace Grace (1973) remains small for all four cases. The bubble mass is conserved, with a maximal mass loss of about 0.02% found in the skirted case, where the bubble undergoes a large and rapid deformation. The corresponding bubble shapes are illustrated in Fig. 12, which clearly displays spherical, ellipsoidal, skirted, and dimpled shapes. We can therefore conclude that the dynamics of a single rising bubble is well-captured.

Table 4: Comparison of computed terminal Reynolds number ( $Re_C$ ) and experimental terminal Reynolds number ( $Re_G$ ) obtained from the Grace diagram Grace (1973) under four different Morton (M) and Eotvos (Eo) numbers.

Case	Bubble regime	$M$	$Eo$	$Re_G$	$Re_C$	Mass loss (%)
(a)	Spherical	$1 \times 10^{-3}$	1	1.7	1.73	$9.86 \times 10^{-5}$
(b)	Ellipsoidal	0.1	10	4.6	4.57	$3.32 \times 10^{-4}$
(c)	Skirted	1	100	20.0	19.21	$1.64 \times 10^{-2}$
(d)	Dimpled	1000	100	1.5	1.71	$3.28 \times 10^{-3}$



(a) Spherical                    (b) Ellipsoidal                    (c) Skirted                    (d) Dimpled

Figure 12: Bubble shapes resulting from different Morton (M) and Eotvos (Eo) numbers, as indicated in Table 4.

## 7. Droplet interactions

A unique feature of colloidal suspensions is the interaction between neighboring droplets, displaying fascinating behaviors such as self-assembly, self-replication, etc. . The reason for such interactions is rather complex; it often arises from a combination of fluid mechanical effects and physicochemical properties of the substance. To study the droplet interactions in the present ICLS/NS framework, we provide in this section a hydrodynamic model for the depletion forces. The method is a natural extension of the LS and GFM, and we demonstrate the clustering of droplets in various structures from a dumbbell to a face-centered cubic crystal.

### 7.1. Extension to multiple level set

The level set method discussed so far involves one marker function; we call it single level set (SLS) method. Thanks to its Eulerian nature, SLS can describe many droplets at the same time, provided that they do not need to be distinguished from each other. On the other hand, SLS can also be extended to multiple level set (MLS), so that each droplet has its own color function. This has several benefits including distinction and tracking of each droplet, independent curvature computation, and ability to prevent numerical coalescence, etc. .

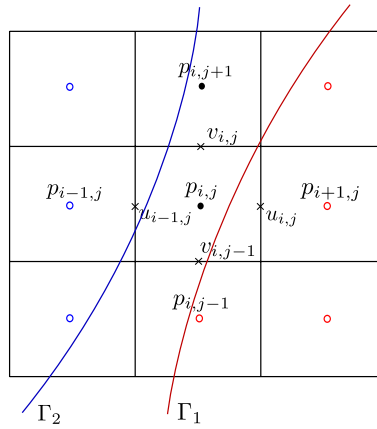


Figure 13: Pressure jump in the presence of multiple interfaces within two grid cells. Red and blue circles indicate nodal pressure in droplet 1 and 2, respectively. (For interpretation of the references to color in this figure legend, the reader is referred to the web version of this article.)

Furthermore, with the narrow band approach Adalsteinsson & Sethian (1995); Peng *et al.* (1999) and the various other techniques introduced in Sec. 1 Nielsen & Museth (2006); Brun *et al.* (2012), the additional computational and memory cost as the number of the level set functions increases is limited.

The extension from SLS to MLS is straightforward. Assuming no droplets will overlap, each level set function is simply advected successively. When two droplets get close (typically within two grid cells, see Fig. 13), the pressure jump across each interface needs to be considered and superimposed. That is, Eq. (48) (corresponding to Fig. 9) should be modified as

$$\begin{aligned} (\nabla^2 p)_{i,j} = & \frac{p_{i-1,j} - 2p_{i,j} + p_{i+1,j}}{\Delta x^2} - 2 \frac{[p]_{i,j}}{\Delta x^2} - \frac{1}{\Delta x} \left[ \frac{\partial p}{\partial x} \right]_{i+1/2,j} + \frac{1}{\Delta x} \left[ \frac{\partial p}{\partial x} \right]_{i-1/2,j} \\ & + \frac{p_{i,j-1} - 2p_{i,j} + p_{i,j+1}}{\Delta y^2} - \frac{[p]_{i,j-1}}{\Delta y^2}, \end{aligned} \quad (73)$$

Similarly, all the jumps should be removed consistently when computing the pressure gradient in the subsequent step. The above modification applies to both SLS and MLS, as the compact formulas (Eqs. (62) and (63)) remain the same; although MLS is clearly more accurate in resolving the near field structure.

## 7.2. Near-field interactions

As introduced earlier, colloidal droplets transported in microfluidic devices are subject to various forces, a typical of which is the depletion force. The depletion force arises from the exclusion of the surfactant micelles in the colloidal

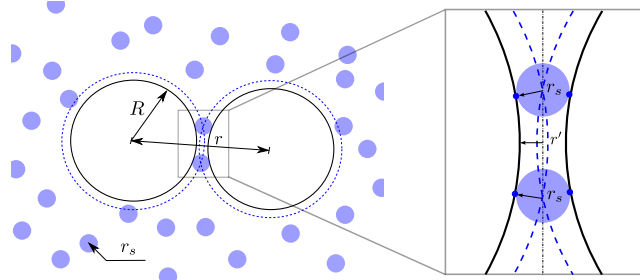


Figure 14: Depletion of surfactant micelles of radius  $r_s$  between larger colloidal droplets of radius  $R$ , separated by distance  $r$ . The dashed lines around larger spheres represent the region from which the centers of small spheres are excluded. They overlap when  $r \leq 2R + 2r_s$ . Inset: a zoom-in sketch of two droplets near contact.

suspension. It is often characterized as a near-field attracting potential Asakura & Oosawa (1958); Mewis & Wagner (2012), and plays a key role in the droplet dynamics Shen *et al.* (2016); Shen (2014). Below, we first provide a brief background on the colloidal theory of the depletion potential, then present a numerical model to enforce the depletion force using MLS and GFM.

### 7.2.1. The colloidal theory of the depletion potential

The original depletion potential model proposed by Asakura and Oosawa Asakura & Oosawa (1958) assumes the surfactant micelles as non-interacting hard-spheres. As sketched in Fig. 14, a suspension of such small spheres around the large colloidal droplets creates an osmotic pressure on the droplet surface. When the distance between two droplets is less than the diameter of the surfactant micelles, there will be a pressure defect due to the exclusion of the micelles, thus creating an attracting force. Integrating this force with respect to the inter-droplet distance  $r$  leads to a potential energy

$$U(r) = \begin{cases} \infty & \text{if } r \leq 2R \\ -p_{os} V_{ex} & \text{if } 2R < r \leq 2R + 2r_s \\ 0 & \text{otherwise,} \end{cases} \quad (74)$$

where  $V_{ex}$  is the excluded volume and  $p_{os}$  is the osmotic pressure. For spherical droplets,  $V_{ex}$  can be calculated analytically

$$V_{ex}(r) = \frac{4\pi(R + r_s)^3}{3} \left[ 1 - \frac{3r}{4(R + r_s)} + \frac{r^3}{16(R + r_s)^3} \right], \quad (75)$$

where  $R$  and  $r_s$  are, respectively, the radii of the big and small spheres. The osmotic pressure is given as

$$p_{os} = nkT, \quad (76)$$

where  $n$  is the number density of the small spheres,  $k$  is the Boltzmann constant, and  $T$  is the temperature. The negative sign in Eq. (74) corresponds to the tendency of the system to reduce its potential energy as the overlap increases. This is equivalent to increasing the total entropy of the small spheres Melby *et al.* (2007), and it provides a physical description of the depletion force even when the droplets are deformable, or when  $p_{os}$  cannot be expressed by the van't Hoff's formula (Eq. (76)) Asakura & Oosawa (1958).

### 7.2.2. A hydrodynamic model for the depletion force

Based on the above theory, the depletion force acting on a droplet is simply the derivative of the depletion potential, *i.e.*  $F(r) = dU/dr = -p_{os}dV_{ex}/dr$ . However,  $dV_{ex}/dr$  is not always straightforward to evaluate for non-spherical droplets; and unlike rigid-body dynamics,  $F(r)$  cannot be applied directly to the motion of a liquid drop. In order to induce locally an aggregation, we take a closer look at the overlap region. As illustrated in Fig. 14, when the surface distance between two colloidal droplets is less than  $2r_s$ , there is a small area in which the osmotic pressure is subject to a jump. Assuming the concentration of the surfactant micelles changes abruptly, it resembles the jump of the Laplace pressure; however, it will not generate any flow if the pressure is uniform in the depleted region. On the contrary, if the osmotic pressure varies continuously within the overlap, *i.e.*  $p' = p'(r')$ , then we can write it as a Taylor-series expansion from  $r' = r_s$

$$p'(r'/r_s) = p'(1) + \left( \frac{r'}{r_s} - 1 \right) \frac{\partial p'}{\partial r'/r_s}, \quad (77)$$

where the distance to the droplet surface  $r'$  is normalized by the surfactant micelle radius. An expansion of the osmotic pressure with the distance corresponds to a gradient of the micelle concentration near the gap. And if the micelle is much smaller than the droplet, as it is in many microfluidic devices Shen *et al.* (2016), the gradient will be very sharp. Conversely, when the distance to the surface varies slowly, such as in the gap of a droplet and a flat wall, a uniform pressure will be recovered. Furthermore, a favorable pressure gradient from the overlap center will generate an outflow, pulling the droplets towards each other. Hence, Eq. (77) provides a hydrodynamic model for the depletion force.

In Eq. (77), the gradient of the osmotic pressure  $\partial p'/\partial(r'/r_s)$  is not known *a priori*. It can be obtained by equating the depletion force acting on one droplet, *i.e.*

$$-p_{os}A_{ex} = \int_{\Omega} (p'(1) - p'(r'/r_s)) dS, \quad (78)$$

where  $A_{ex}$  is the effective area of the overlap  $\Omega$ . Assuming a constant  $\partial p'/\partial(r'/r_s)$ , the above yields a linear dependence of the osmotic pressure on  $r'$ . Note that this is not the same as  $p'$  varying linearly with the distance to the overlap center (see Fig. 14). A description of the implementation and verification will be shown in the next section.

---

**Algorithm 1:** A pseudo code for computing the depletion force.

---

Enter the pressure solver. Compute the right-hand side of Eq. (62).

**for**  $m = 1 : (N - 1)$  **do**

Get the level set for droplet  $m$ ,  $\phi_m$ .

**for**  $n = (m + 1) : N$  **do**

Get the level set for droplet  $n$ ,  $\phi_n$ .

**where**  $\phi_m < r_s$  and  $\phi_n < r_s$  **do**  $r' = (\phi_m + \phi_n)/2$ , tag as *overlap*.

Compute  $[p']_\Omega$  from Eqs. (78) and (79) within *overlap*.

**forall**  $i, j, k$  **do**

**if** *entering overlap* **then**

| Add the osmotic pressure jump  $[p']_{i,j,k}$ .

**else**

| Remove the osmotic pressure jump  $[p']_{i,j,k}$ .

**end**

**end**

**end**

**end**

Solve for  $p^{n+1}$  regularly using the FastP\* and GFM. Exit the pressure solver.

---

### 7.2.3. A MLS/GFM-based method for computing the depletion force

Provided a hydrodynamic model for the depletion force between two droplets, we can easily generalize it to multiple droplets using the MLS. Thanks to the distance information embedded in the level set functions, it is straightforward to identify the overlap region of arbitrary geometries. Furthermore, as the jump of the osmotic pressure occurs only across the overlap shell, we can define

$$[p']_\Omega = p'(r'/r_s) - p'(1), \quad (79)$$

similar to the Laplace pressure jump  $[p]_\Gamma$  implemented by the GFM. Based on these observations, we propose a numerical method to compute the depletion force as laid out in Algorithm 1.

The overall idea of Algorithm 1 is to enforce the depletion attraction in the projection step through the use of MLS and GFM. Specifically, we first locate the overlap region of a pair of droplets with its own level set function, and define  $r'$  as the average of the two distances. Then, Eq. (78) can be integrated numerically to obtain  $\partial p'/\partial(r'/r_s)$ , which together with Eqs. (77) and (79) gives  $[p']_\Omega$ . This variable pressure jump manifests itself as a modification term on the right-hand side of Eq. (62), allowing us to use GFM to impose it across a sharp overlap shell. The resulting flow is divergence-free provided that all the jump terms are removed consistently in the correction step. Therefore, Eqs. (62) and

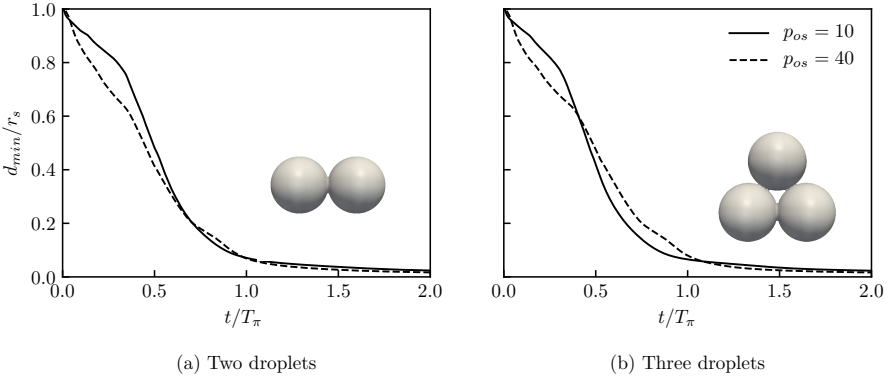


Figure 15: Minimal distance between the droplet surfaces as function of time in the presence of depletion forces proportional to  $p_{os} = 10$  (solid line) and  $p_{os} = 40$  (dashed line). Simulation of (a) two droplets and (b) three droplets suspended in an initially quiescent fluid. Due to symmetry, only the minimal distance is plotted.

(63) are re-formulated as <sup>1</sup>

$$\nabla^2 p^{n+1} = \nabla_g^2 ([p]_\Gamma + [p']_\Omega) + \nabla \cdot \left[ \left( 1 - \frac{\rho_0}{\rho^{n+1}} \right) \nabla_g \hat{p} \right] + \frac{\rho_0}{\Delta t} \nabla \cdot \mathbf{u}^*, \quad (80)$$

and

$$\mathbf{u}^{n+1} = \mathbf{u}^* - \Delta t \left[ \frac{1}{\rho_0} \nabla_g p^{n+1} + \left( \frac{1}{\rho^{n+1}} - \frac{1}{\rho_0} \right) \nabla_g \hat{p} \right]. \quad (81)$$

**Approaching drops.** We verify the depletion force model and its numerical implementation by simulating 2 to 14 approaching droplets in a quiescent fluid environment. Specifically, we set the droplet radius  $R = 0.5$ , the computational domain  $3 \times 3 \times 3$ , and the resolution  $\Delta x = 1/32$ . The radius of the surfactant micelle is set to be  $r_s = 1/16$ , corresponding to  $2\Delta x$ . The viscosity and density ratios of the droplet to the ambient fluid are both 1. The non-dimensional parameters are  $La = 2000$  and  $Fr = \infty$ , leading to a reference Laplace pressure jump  $p_\sigma = 80$  and neglected gravity. The uniform osmotic pressure is either 10 or 40.

The temporal evolutions of the minimal surface distances in the case of two and three droplets are shown in Fig. 15. Here, time is scaled by a factor  $T_\pi = (r_s/R)(p_\sigma/p_{os})$ . The droplets, originally separated by a distance of  $r_s$ , get closer to the limit of the grid spacing at  $t \approx T_\pi$ . For the present study, we let the droplets aggregate without applying any repulsion models, except that

<sup>1</sup>Eqs. (63) and (81) are identical in form; however,  $[p']_\Omega$  has to be removed when evaluating  $\nabla_g p^{n+1}$  and  $\nabla_g \hat{p}$  in Eq. (81), as it is done in Eq. (61)

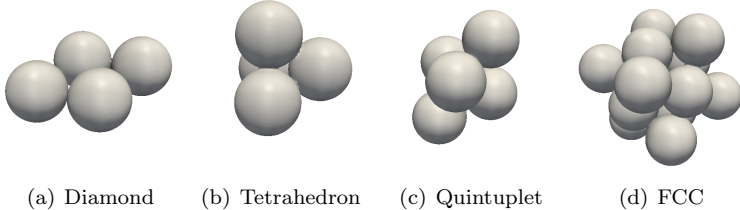


Figure 16: Examples of droplet clusters of different structures.

the magnitude of the osmotic pressure is reduced when  $d_{min}/r_s < 0.1$ . The smooth approaching in all cases and the collapse of the distance curve clearly evidence an attracting depletion force. To assess the robustness of the method, we further tested clustering of droplets into shapes from a 2D diamond to a face-centered cubic (FCC) composed of 14 drops, illustrated here in Fig. 16. FCC represents the unit structure of one of the most compact sphere packings. Therefore, we can conclude that the hydrodynamic model implemented by the MLS/GFM-based method is accurate and robust in computing the depletion forces.

## 8. Conclusion

A numerical method mainly intended for the hydrodynamic simulations of colloidal droplets in microfluidic devices has been developed and validated. The code is based on an efficient and sharp solver of the incompressible, two-fluid Navier-Stokes equations, and uses a mass-conserving level set method to capture the fluid interface. This combination provides a general framework for any multiphase flow problems (see e.g. our recent study on jet instabilities Tammisola *et al.* (2017)), and allows us to develop specific methods for the simulations of droplets in saturated surfactant suspensions with depletion forces as in the recent experiment in Shen *et al.* (2016). Particularly, we have developed or extended four numerical techniques to improve the general accuracy:

1. A mass-conserving, interface-correction level set method (ICLS) is proposed. As a standalone level set module, it is efficient, accurate, guarantees global mass conservation, and is simple to implement. It also enables corrections that can depend on the local curvature or any other parameter of interest.
2. A geometric estimation of the interface curvature based on nodal curvatures is introduced. As an important ingredient both for the mass correction (ICLS) and the surface tension computation, we show that the calculation converges in second-order both in 2D and 3D, and can lead to machine-zero spurious currents for a stationary 2D droplet.

3. The ghost fluid method (GFM) for the computation of surface tension is combined with the FastP\* method Dodd & Ferrante (2014). This enables the use of FFT-based solvers for a direct pressure solve, and can accurately account for surface tension at large density ratios.
4. A ghost fluid/multiple level set (GFM/MLS-based) method is also proposed to compute the interaction force caused by depletion potentials between multiple droplets or between droplets and a nearby wall. The approach can possibly be extended to account for surfactant diffusion at the interface and in the liquid.

The last technique applies specifically to the simulation of colloidal droplets in microfluidic devices. This will enable us to further explore the effects of the near-field interactions as those observed experimentally in Shen *et al.* (2016), and potentially improve the design of microfluidic devices. In addition, the combination of the GFM for sharp interfaces and the FastP\* method Dodd & Ferrante (2014) can be exploited for the simulations of droplet in turbulent flows as in Dodd & Ferrante (2016), adding an accurate representation of evaporation thanks to the ICLS approach proposed here.

## Acknowledgments

The work is supported by the Microflusa project. This effort receives funding from the European Union Horizon 2020 research and innovation programme under Grant Agreement No. 664823. O.T. acknowledges support from Swedish Research Council (VR) through the Grant Nr. 2013-5789. L.B. and J.-C.L. also acknowledge financial support by the European Research Council grant, no. ERC-2013-CoG-616186, TRITOS. The computer time was provided by SNIC (Swedish National Infrastructure for Computing). Last but not least, Z.G. thanks Mehdi Niazi, Michael Dodd, Walter Fornari, Dr. Olivier Desjardins, Dr. Sébastien Tanguy, Dr. Marcus Herrmann, and Dr. David Salac for interesting and helpful discussions.

## Appendix A. Discretization error of $\int_{\Gamma} \mathbf{n} \cdot \mathbf{u}_c d\Gamma$

Similar to Engquist *et al.* (2005), we define the discretization error

$$E = \left| \left( \prod_{k=1}^d \Delta x_k \right) \sum_{j \in Z^d} \hat{\delta}_{\epsilon}(\Gamma, g, \mathbf{x}_j) - \int_{\Gamma} \mathbf{n} \cdot \mathbf{u}_c d\Gamma \right|, \quad (82)$$

where  $\hat{\delta}_{\epsilon}$  is a Dirac delta function of variable strength  $g$  supported on the surface  $\Gamma$ , and  $\mathbf{x} \in \mathbb{R}^d$ . Following the derivations in Sec. 4, the extension of  $g$  to  $\mathbb{R}^d$  is provided by Eq. (22), allowing one to write

$$E = \left| \left( \prod_{k=1}^d \Delta x_k \right) \sum_{j \in Z^d} \frac{\delta V}{\delta t} \frac{f_s \delta_{\epsilon}(\phi(\mathbf{x}_j)) |\nabla \phi(\mathbf{x}_j)|}{A_f} - \int_{\Gamma} \mathbf{n} \cdot \mathbf{u}_c d\Gamma \right|. \quad (83)$$

Here,  $\delta_{\epsilon}(\phi)$  is a one dimensional regularized delta function depending on the level set  $\phi$ , and the expression is simplified noting that  $\mathbf{n} \cdot \nabla \phi = |\nabla \phi|$  (it does

not have to be a distance function). By definition,  $A_f = \int_{\Gamma} f_s \delta_{\epsilon}(\phi) |\nabla \phi| d\Gamma$ , discretely reducing Eq. (83) to

$$E = \left| \frac{\delta V}{\delta t} - \int_{\Gamma} \mathbf{n} \cdot \mathbf{u}_c d\Gamma \right|. \quad (84)$$

Comparing with Eq. (13), it is obvious that  $E = 0$ . That is, the discretization error of  $\int_{\Gamma} \mathbf{n} \cdot \mathbf{u}_c d\Gamma$  used in the mass correction is identically zero, independent of the choice of the regularized delta function.

## REFERENCES

- AANJANEYA, M., PATKAR, S. & FEDKIW, R. 2013 A monolithic mass tracking formulation for bubbles in incompressible flow. *J. Comput. Phys.* **247**, 17–61.
- ADALSTEINSSON, D. & SETHIAN, J. 1995 A fast level set method for propagating interfaces. *J. Comput. Phys.* **111**(2), 269–277.
- ADALSTEINSSON, D. & SETHIAN, J. 1999 The fastconstruction of extension velocities in level set methods. *J. Comput. Phys.* **148**, 2–22.
- ANNALAND, M. v. S., DEEN, N. & KUIPERS, J. 2005 Numerical simulation of gas bubbles behaviour using a three-dimensional volume of fluid method. *Chemical Engineering Science* **60**, 2999–3011.
- ASAKURA, S. & OOSAWA, F. 1958 Interaction between particles suspended in solutions of macromolecules. *Journal of Polymer Science* **XXXIII**, 183–192.
- BRACKBILL, J., KOTHE, D. & ZEMACH, C. 1992 A continuum method for modeling surface tension. *J. Comput. Phys.* **100**, 335–354.
- BREUGEM, W.-P. 2012 Numerical simulation of drop impact on a liquid-liquid interface with a multiple marker front-capturing method. *J. Comput. Phys.* **228**, 4444–4467.
- BRUN, E., GUILLETET, A. & GIBOU, F. 2012 A local level-set method using a hash table data structure. *J. Comput. Phys.* **231**, 2528–2536.
- CHEN, S., MERRIMAN, B., OSHER, S. & SMEREKA, P. 1997 A simple level set method for solving stefan problems. *J. Comput. Phys.* **135**, 8–29.
- DU CHÉNÉ, A., MIN, C. & GIBOU, F. 2008 Second-order accurate computation of curvatures in a level set framework using novel high-order reinitialization schemes. *J. Sci. Comput.* **35**, 114–131.
- CHORIN, A. 1968 Numerical solution of the navier-stokes equations. *Math. Comput.* **22**, 745–762.
- COSTA, P. S. 2017 Cans (canonical navier-stokes). <https://github.com/p-costa/CaNS>, accessed: 2017-10-11.
- COYAJEE, E. & BOERSMA, B. 2009 A second-order accurate immersed boundary method for fully resolved simulations of particle-laden flows. *J. Comput. Phys.* **231**, 4469–4498.
- DENNER, F. & WACHEM, B. v. 2015 Numerical time-step restrictions as a result of capillary waves. *J. Comput. Phys.* **285**, 24–40.
- DESJARDINS, O., MOUREAU, V. & PITSCHE, H. 2008 An accurate conservative level set/ghost fluid method for simulating turbulent atomization. *J. Comput. Phys.* **227**, 8395–8416.
- DODD, M. & FERRANTE, A. 2014 A fast pressure-correction method for incompressible two-fluid flows. *J. Comput. Phys.* **273**, 416–434.

- DODD, M. & FERRANTE, A. 2016 On the interaction of taylor length scale size droplets and isotropic turbulence. *J. Fluid Mech.* **806**, 356–412.
- DONG, S. & SHEN, J. 2012 A time-stepping scheme involving constant coefficient matrices for phase-field incompressible flows with large density ratios. *J. Comput. Phys.* **231**, 5788–5804.
- ENGQUIST, B., TORNBERG, A.-K. & TSAI, R. 2005 Discretization of dirac delta functions in level set methods. *J. Comput. Phys.* **207**, 28–51.
- ENRIGHT, D., FEDKIW, R., FERZIGER, J. & MITCHELL, I. 2002 A hybrid particle level set method for improved interface capturing. *J. Comput. Phys.* **183**, 83–116.
- FEDKIW, R., ASLAM, T., MERRIMAN, B. & OSHER, S. 1999 A non-oscillatory eulerian approach to interfaces in multimaterial flows (the ghost fluid method). *J. Comput. Phys.* **152**, 457–492.
- FRANCOIS, M., CUMMINS, S., DENDY, E., KOTHE, D., SICILIAN, J. & WILLIAMS, M. 2006 A balanced force algorithm for continuous and sharp interfacial surface tension models within a volume tracking framework. *J. Comput. Phys.* **213**, 141–173.
- GALUSINSKI, C. & VIGNEAUS, P. 2008 On stability condition for bifluid flows with surface tension: Application to microfluidics. *J. Comput. Phys.* **227**, 6140–6164.
- GRACE, J. R. 1973 Shapes and velocities of bubbles rising in infinite liquids. *Transactions of the Institution of Chemical Engineering* **51**, 116–120.
- HERRMANN, M. 2008 A balanced force refined level set grid method for two-phase flows on unstructured flow solver grids. *J. Comput. Phys.* **227**, 2674–2706.
- KANG, M., FEDKIW, R. & LIU, X.-D. 2000 A boundary condition capturing method for multiphase incompressible flow. *J. Sci. Comput.* **15**, 323–360.
- KUMAR, A. & GRAHAM, M. 2012 Accelerated boundary integral method for multiphase flow in non-periodic geometries. *J. Comput. Phys.* **231**, 6682–6713.
- LALANNE, B., VILLEGRAS, L. R., TANGUY, S. & RISSO, F. 2015 On the computation of viscous terms for incompressible two-phase flows with level set/ghost fluid method. *J. Comput. Phys.* **301**, 289–307.
- LI, F., JOSEPHSON, D. & STEIN, A. 2011 Colloidal assembly: the road from particles to colloidal molecules and crystals. *Angew. Chem. Int. Ed.* **50**, 360–388.
- LIU, X.-D., FEDKIW, R. & KANG, M. 2000 A boundary condition capturing method for poisson's equation on irregular domains. *J. Comput. Phys.* **160**, 151–178.
- LIU, X.-D., OSHER, S. & CHAN, T. 1994 Weighted essentially non-oscillatory schemes. *J. Comput. Phys.* **115**, 200–213.
- LIU, X.-D. & SIDERIS, T. C. 2003 Convergence of the ghost fluid method for elliptic equations with interfaces. *Math. Comput.* **72**, 1731–1746.
- LUO, J., HU, X. & ADAMS, N. 2015a A conservative sharp interface method for incompressible multiphase flows. *J. Comput. Phys.* **284**, 547–565.
- LUO, K., SHAO, C., YANG, Y. & FAN, J. 2015b An mass conserving level set method for detailed numerical simulation of liquid atomization. *J. Comput. Phys.* **298**, 495–519.
- MARCHANDISE, E., GEUZAIN, P., CHEVAUGEON, N. & REMACLE, J.-F. 2007 A stabilized finite element method using a discontinuous level set approach for the computation of bubble dynamics. *J. Comput. Phys.* **225**, 949–974.
- MELBY, P., PREVOST, A., EGOLF, D. & URBACH, J. 2007 Depletion force in a bidisperse granular layer. *Phys. Rev. E* **76**, 051307, 1–5.

- MEWIS, J. & WAGNER, N. 2012 *Colloidal suspension rheology*. New York, USA: Cambridge University Press.
- MIN, C. & GIBOU, F. 2007 A second order accurate level set method on non-graded adaptive cartesian grids. *J. Comput. Phys.* **225**, 300–321.
- MULDER, W., OSHER, S. & SETHIAN, J. 1992 Computing interface motion in compressible gas dynamcis. *J. Comput. Phys.* **100**, 209–228.
- NIELSEN, M. & MUSETH, K. 2006 Dynamic tubular grid: an efficient data structure and algorithms for high resolution level sets. *J. Sci. Comput.* **26**, 261–299.
- NOURGALIEV, R. & THEOFANOUS, T. 2007 High-fidelity interface tracking in compressible flows: unlimited anchored adaptive level set. *J. Comput. Phys.* **227**, 836–866.
- OLSSON, E. & KREISS, G. 2005 A conservative level set method for two phase flow. *J. Comput. Phys.* **210**, 225–246.
- PENG, D., MERRIMAN, B., OSHER, S., ZHAO, H. & KANG, M. 1999 A pde-based fast local level set method. *J. Comput. Phys.* **155**, 410–438.
- PESKIN, C. S. 1972 Flow patterns around heart valves: a numerical method. *J. Comput. Phys.* **10**, 252–271.
- PIJL, S. v. d., SEGAL, A., VUIK, C. & WESSELING, P. 2008 Computing three-dimensional two-phase flows with a mass-conserving level set method. *Comput. Vis. Sci.* **11**, 221–235.
- POPINET, S. 2009 An accurate adaptive solver for surface-tension-driven interfacial flows. *J. Comput. Phys.* **228**, 5838–5866.
- POPINET, S. 2018 Numerical models of surface tension. *Ann. Rev. Fluid Mech.* **50**, 49–75.
- POZRIKIDIS, C. 1992 *Boundary integral and singularity methods for linearized viscous flow*. New York, USA: Cambridge University Press.
- PROSPERETTI, A. 1981 Motion of two superposed viscous fluids. *Phys. Fluids* **24**, 1217.
- RUSSO, G. & SMEREKA, P. 2000 A remark on computing distance functions. *J. Comput. Phys.* **163**, 51–67.
- SACANNA, S. & PINE, D. 2011 Shape-anisotropic colloids: building blocks for complex assemblies. *Curr. Opin. Colloid Interface Sci.* **16**, 96–105.
- SALAC, D. 2016 A general, mass-preserving navier-stokes projection method. *Comput. Phys. Comm.* **204**, 97–106.
- SCARDOVELLI, R. & ZALESKI, S. 1999 Direct numerical simulation of free-surface and interfacial flow. *Ann. Rev. Fluid Mech.* **31**, 567–603.
- SCHUMANN, U. & SWEET, R. A. 1988 Fast fourier transforms for direct solution of poisson's equation with staggered boundary conditions. *J. Comput. Phys.* **75**, 123–137.
- SETHIAN, J. 1999 *Level set method and fast marching method*. New York, USA: Cambridge University Press.
- SHEN, B. 2014 Transport and self-assembly of droplets in microfluidic devices. PhD thesis, Physics. Université Pierre et Marie Curie - Paris VI, english. MNT: 2014PA066499. Tel-01127629.
- SHEN, B., RICOURVIER, J., MALLOGGI, F. & TABELING, P. 2016 Designing colloidal molecules with microfluidics. *Adv. Sci.* **1600012**, 1–7.

- SHU, C.-W. & OSHER, S. 1988 Efficient implementation of essentially non-oscillatory shock-capturing schemes. *J. Comput. Phys.* **77**, 439–471.
- STRAIN, J. 1999a Semi-lagrangian methods for level set equations. *J. Comput. Phys.* **151**(2), 498–533.
- STRAIN, J. 1999b Tree methods for moving interfaces. *J. Comput. Phys.* **151**, 616–648.
- SUSSMAN, M. & FATEMI, E. 1997 An efficient, interface-preserving level set redistancing algorithm and its application to interfacial incompressible fluid flow. *J. Sci. Comput.* **20**, 1165–1191.
- SUSSMAN, M. & PUCKETT, E. 2000 A coupled level set and volume-of-fluid method for computing 3d and axisymmetric incompressible two-phase flows. *J. Comput. Phys.* **162**, 301–337.
- SUSSMAN, M., SMEREKA, P. & OSHER, S. 1994 A level set approach for computing solutions to incompressible two-phase flow. *J. Comput. Phys.* **114**, 146–159.
- TAMMISOLA, O., LOISEAU, J.-C. & BRANDT, L. 2017 Effect of viscosity ratio on the self-sustained instabilities in planar immiscible jets. *Phys. Rev. Fluids* **2**(3) 033903.
- TANGUY, S. & BERLEMONT, A. 2005 Application of a level set method for simulations of droplet collisions. *Int. J. Multiph. Flow* **31**, 1015–1035.
- UHLMANN, M. 2005 A immersed boundary method with direct forcing for simulation of particulate flows. *J. Comput. Phys.* **209**, 448–476.
- VELEV, O. & GUPTA, S. 2009 Materials fabricated by micro- and nanoparticle assembly - the challenging path from science to engineering. *Adv. Mater.* **21**, 1897–1905.
- VELMURUGANA, G., E.M., K. & SALAC, D. 2016 Level set jet schemes for stiff advection equations: The semijet method. *ArXiv* **1509.0283**.
- WÖRNER, M. 2012 Numerical modeling of multiphase flows in microfluidics and micro process engineering: a review of methods and applications. *Microfluid Nanofluid* **12**, 841–886.
- XIA, Y., GATES, B., YIN, Y. & LU, Y. 2000 Monodispersed colloidal spheres: old materials with new applications. *Adv. Mater.* **12**, 693–713.
- YI, G.-R., PINE, D. & SACANNA, S. 2013 Recent progress on patchy colloids and their self-assembly. *J. Phys.: Condens. Matter* **25**, 193101.
- ZALESAK, S. 1979 Fully multidimensional flux-corrected transport algorithms for fluids. *J. Comput. Phys.* **31**, 335–362.
- ZHU, L., RORAI, C., DHRUBADITYA, M. & BRANDT, L. 2014 A microfluidic device to sort capsules by deformability: a numerical study. *Soft Matter* **10**, 7705–7711.

**2**

**Paper 2**



# Integral representation of channel flow with interacting particles

Itzhak Fouxon<sup>1,2</sup>, Zhouyang Ge<sup>3</sup>, Luca Brandt<sup>3</sup>,  
Alexander Leshansky<sup>1</sup>

<sup>1</sup> Department of Chemical Engineering, Technion, Haifa 32000, Israel

<sup>2</sup> Department of Computational Science and Engineering, Yonsei University,  
Seoul 120-749, South Korea

<sup>3</sup> Linné FLOW Centre and SeRC, KTH Mechanics, S-100 44 Stockholm, Sweden

*Physical Review E* (2017), vol. **96** (063110)

We construct a boundary integral representation for the low-Reynolds-number flow in a channel in the presence of freely-suspended particles (or droplets) of arbitrary size and shape. We demonstrate that lubrication theory holds away from the particles at horizontal distances exceeding the channel height and derive a multipole expansion of the flow which is dipolar to the leading approximation. We show that the dipole moment of an arbitrary particle is a weighted integral of the stress and the flow at the particle surface, which can be determined numerically. We introduce the equation of motion that describes hydrodynamic interactions between arbitrary, possibly different, distant particles, with interactions determined by the product of the mobility matrix and the dipole moment. Further, the problem of three identical interacting spheres initially aligned in the streamwise direction is considered and the experimentally observed “pair exchange” phenomenon is derived analytically and confirmed numerically. For non-aligned particles, we demonstrate the formation of a configuration with one particle separating from a stable pair. Our results suggest that in a dilute initially homogenous particulate suspension flowing in a channel the particles will eventually separate into singlets and pairs.

---

## 1. Introduction

Hydrodynamic interactions among particles flowing in the fluid confined between two parallel walls at low Reynolds number have recently attracted a considerable attention Carbajal-Tinoco *et al.* (1997); Acuña Campa *et al.* (1998); ?; Pesché & Nägele (2000); Lançon *et al.* (2001); Marcus *et al.* (1999); Santana-Solano & Arauz-Lara (2001, 2002); Cui *et al.* (2004); Cohen *et al.* (2004); Tlusty (2006); Beatus *et al.* (2006, 2012); Sarig *et al.* (2016); ?; ?; ?; ?; ?; ?; ?; ?; ?; ?; ?). The case of particles driven by thermal noise in the absence of a macroscopic flow was studied in Carbajal-Tinoco *et al.* (1997); Acuña Campa *et al.* (1998); ?; Pesché & Nägele (2000); Lançon *et al.* (2001); Marcus *et al.*

(1999); Santana-Solano & Arauz-Lara (2001, 2002); Cui *et al.* (2004); Cohen *et al.* (2004); Tlusty (2006). The hydrodynamic interactions cause long-range correlations in their diffusive motions that are measurable even at distances ten times larger than the particle size Carbajal-Tinoco *et al.* (1997); Cui *et al.* (2004). In the case of pressure-driven Poiseuille or shear flow the particles are, in addition, dragged by the flow ????Beatus *et al.* (2006, 2012); ?; ?; ?; Sarig *et al.* (2016).

Identical particles at similar positions inside the channel move at the same velocity if not for hydrodynamic interactions. These interactions induce particle relative motions, which can result in considerable changes of their configuration inside the channel. In the case of a large number of particles the interactions cause also chaotic collisions among the particles ?.

Theoretical progress has mainly relied on the observation that the far flow caused by a particle confined in a channel is a dipolar flow decaying quadratically with the distance Cui *et al.* (2004). For disk-like particles with thickness close to the channel width  $h$ , the dipolar flow and its moments were derived from lubrication theory in Tlusty (2006). The dipolar flow holds at distances much larger than the disk radius, where it gives also the leading order hydrodynamic interactions among particles Tlusty (2006); Beatus *et al.* (2006, 2012); ?.

It was observed in Beatus *et al.* (2012), however, that hydrodynamic interactions of pancake-like disks can also be described at much smaller distances between the disks where dipolar approximation breaks down, yet lubrication theory still holds ??. This theory predicts that at distances from the particle boundary much larger than  $h$  the depth-averaged flow is an ideal two dimensional flow with potential obeying the Laplace equation. The boundary condition (b. c.), derived somewhat heuristically, is the usual ideal flow b. c. prescribing the velocity component normal to the particle surfaces ?, which allowed to find the hydrodynamic interactions of two close disks, see Beatus *et al.* (2012). Moreover, it was observed that the non-rigidity of the particles makes the lubrication theory valid up to distances from the particles smaller than  $h$ . The calculation of the hydrodynamic interactions for disks of different radii requires solving the Laplace equation with the help of bipolar coordinates, see Sarig *et al.* (2016).

Recently, a practical applications of hydrodynamic interactions among particles in a channel has been proposed. In particular, it is suggested that the combined action of adhesive (non-hydrodynamic) forces and hydrodynamic interactions between microdroplets can result in the formation of regular particle clusters and can thus be potentially used for the production of new materials ?. The hydrodynamic forces are believed to be a significant factor in these structure formation. Though the particles forming the structure are in a close proximity in the experiments mentioned above, the hydrodynamic interactions are described phenomenologically by a dipolar flow, formally only valid at larger distances. Despite the use of the far-field dipolar flow beyond its domain of validity, the numerical simulations in ? showed very good agreement with the

experimental results ?. The above motivates the need for the detailed theoretical study of hydrodynamic interactions among particles in narrow channels.

In this work, we introduce a boundary integral representation of the channel flow in the presence of freely suspended particles. The particles can be rigid or soft (droplets). The representation does not depend on the particle equation of motion, defined by inertia. Boundary integral representations are known to be useful in unconfined flows and can also be applied to confined geometries ??. The flow is here expressed as the sum of the undisturbed Poiseuille flow and an integral over the surfaces of all particles, where the particles can have arbitrary shapes. The derivation is performed for a pressure-driven flow, but identical considerations can be applied to shear flows.

Our representation results in a formula for calculation of the dipole moment, which was previously available only for the case of disk-like particles. The moment is given in terms of a weighted integral of the stress tensor and the flow over the surface(s) of the particle(s). Once this integral is numerically tabulated, the result can be used to approximate the flow in different configurations. Here, we perform simulations for the case of neutrally buoyant rigid spherical particles and compute the integral for different positions of the particle center and different ratios of the particle radius to the channel height, i.e. different confinements.

We use this new integral representation to show that the lubrication theory holds at the particle near proximity, closer than what typically expected. As an example, we solve the problem of three aligned particles moving along the line defined by their centers and the case of three nonaligned particles. We conjecture that this solution is the attractor to which the long-time evolution of arbitrary initial condition converges. We conclude by proposing a mean field description of strong hydrodynamic interactions of close particles in a dense suspension.

## 2. Integral representation for channel flow with particles

In this Section we derive the boundary integral representation for channel flow in the presence of an arbitrary number of particles of arbitrary shape (see Fig. 1 where spherical particles are shown for illustration). It is assumed that the Reynolds number is low and the Stokes equations hold. The derivation uses the reciprocal theorem with the reciprocal flow given by the Stokeslet in a channel ?, similarly to the derivations in infinite space, see e. g. ?. In this Section we make no assumptions on the form of the equation of motion of the particles which may change according to the relevance of inertia. The particles can be rigid, droplets or, e.g. viscoelastic.

The undisturbed flow  $\mathbf{u}^0$ , in the absence of particles, is the Poiseuille flow driven by the constant pressure gradient  $\nabla p^0$ ,

$$u_x^0 = \frac{z(z-h)\nabla_x p^0}{2\eta}, \quad \nabla p^0 = \eta\nabla^2 \mathbf{u}^0. \quad (1)$$

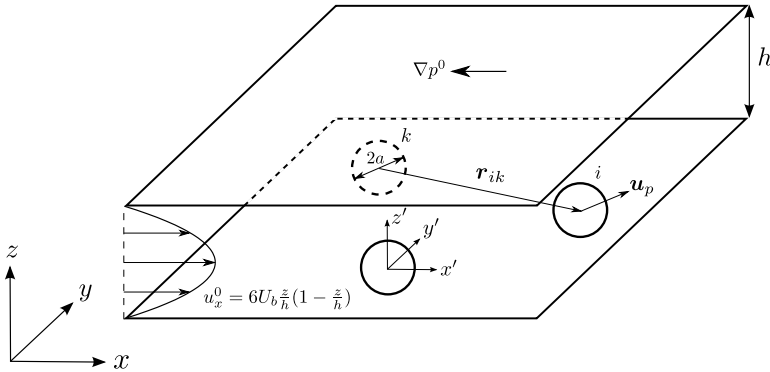


Figure 1: Schematic configuration of spherical particles flowing in the pressure-driven (Poiseuille) flow in a channel.

where  $\eta$  is the fluid viscosity,  $z$  is the vertical coordinate and  $h$  is the channel width. The flow is in  $x$ -direction,  $\nabla_x p^0 = -|\nabla_x p^0| \hat{\mathbf{x}}$ . In the presence of a freely suspended particle we look for the solution of,

$$\begin{aligned} \nabla p &= \eta \nabla^2 \mathbf{u}, \quad \nabla \cdot \mathbf{u} = 0, \quad \mathbf{u}(z = 0) = \mathbf{u}(z = h) = 0, \\ u_x(\infty) &= \frac{z(z-h)\nabla_x p^0}{2\eta}, \end{aligned} \quad (2)$$

which holds outside the particle. The flow is completely determined when solving for the particle motion, i.e. knowing the instantaneous particle position as it determines the boundary condition  $\mathbf{u}_S(\mathbf{x})$  on the particle surface  $S$ . In the case of a rigid particle,  $\mathbf{u}_S(\mathbf{x}) = \mathbf{v} + \boldsymbol{\omega} \times (\mathbf{x} - \mathbf{y})$  where  $\mathbf{v}$  and  $\boldsymbol{\omega}$  are the particle translational and angular velocities and  $\mathbf{y} = (x_p, y_p, z_p)$  is the coordinate of the particle center of mass. The velocities  $\mathbf{v}$  and  $\boldsymbol{\omega}$  are determined by the solution of the equation for the particle motion coupled with the flow. These velocities could be time-independent as in the case of the steady motion of a neutrally buoyant rigid particle or the case of a non-neutrally buoyant particle after sedimentation when reaching the bottom wall (the theoretical determination of these velocities is impossible generally because of the interaction with the walls). These velocities can also be time-dependent as in the case of a transient flow or the gravitational settling of a non-neutrally buoyant particle. If several particles are considered, a time-dependent configuration can be induced by their interactions. We assume here that the time variations are not fast so that the unsteady time-derivative term of the Navier-Stokes equations is negligible (for the steady motion of one particle the time-derivative is the spatial derivative of the flow along the streamline which is small because of the smallness of the Reynolds number). In the case of droplets the boundary condition on the

surface is determined by matching with the inner flow. However there is no need for solving for this inner flow since the detailed form of  $\mathbf{u}_S(\mathbf{x})$  is irrelevant for the derivation of the present representation. The generalization of the problem to the case of many particles is obvious.

*Implications of lubrication theory.*—Some conclusions on the flow at distances from the particle much larger than the channel width  $h$  can be obtained from lubrication theory ?????. The lubrication theory predicts that at these distances,

$$\mathbf{u} = \frac{z(z-h)\nabla p}{2\eta}, \quad (3)$$

with a certain  $z$ -independent  $p$ . Clearly, at large distances,  $p \approx p^0$  at the leading order. The depth-averaged velocity  $\mathbf{u}_d$  is the ideal potential two-dimensional flow,

$$\mathbf{u}_d = \nabla\phi, \quad \phi = -\frac{h^2 p}{12\eta}, \quad \nabla^2\phi = 0. \quad (4)$$

In some cases this helps determining the flow completely.

*Large disks.*—Large non-wetting droplets squeezed between the walls of a Hele-Shaw cell have pancake-like shapes. These can be modeled as disks with radius  $a \gg h$  and height close to  $h$ , i.e., they almost fill the entire channel height Tlusty (2006); Beatus *et al.* (2006, 2012); ?. In this case, one can use Eqs. (3)-(4) at distances from the body that are much larger than  $h$  but much smaller than  $a$ . Thus the ideal flow holds outside the narrow boundary layer near the particle surface whose characteristic size  $l_0$  is of the order  $h$ , much smaller than the particle horizontal size  $a$ . We call the layer containing the flow vorticity the viscous layer and assume that there is no flux of mass through the surface of the droplet, which keeps its shape and volume. Thus, in the frame of reference moving with the disk, the normal velocity component is zero at the outer boundary of the layer and the ideal flow outside the layer is determined uniquely by this boundary condition. However the geometry of the layer is not always known and the complete determination of the flow not possible. If we are only interested in the flow outside the immediate  $l_0$ -vicinity of the viscous layer, we can set the boundary condition for the ideal flow on the disk itself, exploiting the fact that  $l_0 \ll a$ . The flow is then found as the dipole potential Tlusty (2006),

$$\phi = -\frac{h^2 p^0}{12\eta} - \frac{\mathbf{d} \cdot \hat{\mathbf{r}}}{r}, \quad \nabla^2\phi = 0, \quad \mathbf{d} = a^2 \mathbf{v}, \quad (5)$$

where  $\mathbf{d}$  is the dipole moment,  $\mathbf{v} = -v\hat{\mathbf{x}}$  is the difference between the disk velocity and  $-h^2\nabla p_0/(12\eta)$ . It is readily seen that the normal, radial component of the velocity  $\nabla\phi$  on the surface of the disk is  $[\mathbf{v} - h^2\nabla p^0/(12\eta)] \cdot \hat{\mathbf{r}}$ . Note that the velocity  $v > 0$  since the particle moves slower than the fluid.

The tangential velocity component on the outer boundary of the viscous layer obtained from Eq. (5) does not match the tangential velocity of the droplet

surface. In contrast with the normal component, which can be considered almost constant through the viscous layer, the tangential component changes quickly through this layer to match the inner flow at the droplet surface. As example, in the limit of high droplet viscosity, the condition on the disk surface is that the flow is the appropriate superposition of translation and solid body rotation. Similar viscous layers occur for rigid bodies oscillating in the fluid [1]. The ideal flow was obtained in Tlusty (2006) and here we describe how this ideal flow fits the complete equations for the viscous flow.

*Boxes.*—Another case where the flow can be fixed without detailed calculations is the case of a box whose smallest dimension is close to  $h$  and the longer dimensions are much larger than  $h$ . If the box is located in the channel so that the flow is perpendicular to its longer axis with length  $l \gg h$  then far from the ends of the box we find the ideal two-dimensional flow with constant velocity on the line. The solution for the ideal flow with constant velocity on an infinite linear boundary is the uniform flow. We thus conclude that in the frame moving with the box there is a region of stagnant flow behind the box, whose size is of order  $l$ .

Generally, the flow can be inferred from the lubrication theory in quite a detail for particles whose horizontal dimensions are much larger than  $h$  and whose vertical dimension is close to  $h$ . The flow outside the narrow viscous layer near the particle surface is  $z(z-h)$  times the two-dimensional ideal flow determined by the boundary condition of zero normal velocity on the particle surface. The tangential velocity changes fast across the viscous layer. However, if the particle horizontal dimensions are not large or the dimensions are large but the vertical dimension is not close to  $h$ , a different approach is needed.

*Boundary integral representation from the reciprocal theorem.*—We use the reciprocal theorem [2] using as the reciprocal flow the solution of [3] for the point-force or Stokeslet between two parallel plates, i.e.

$$\begin{aligned} -\nabla p^S + \eta \nabla^2 \mathbf{u}^S + \mathbf{g} \delta(\mathbf{x} - \mathbf{x}_0) &= 0, \quad \nabla \cdot \mathbf{u}^S = 0, \\ \mathbf{u}^S(z=0) &= \mathbf{u}^S(z=h) = 0, \quad \mathbf{u}^S(x^2 + y^2 \rightarrow \infty) = 0. \end{aligned} \quad (6)$$

Analogously to the flow due to a point-force acting on a viscous fluid in infinite space (e.g. [4]), the solution depends linearly on the source forcing  $\mathbf{g}$ ,

$$\mathbf{u}^S(\mathbf{x}) = \frac{1}{8\pi\eta} S_{ik}(\mathbf{x}, \mathbf{x}_0) g_k, \quad (7)$$

where we introduced the tensor  $S_{ik}$  independent of  $\mathbf{g}$ . Similarly for the stress tensor of the Stokeslet solution we can write,

$$\sigma_{ik}^S(\mathbf{x}) = -p^S \delta_{ik} + \eta (\nabla_k u_i^S + \nabla_i u_k^S) = \frac{T_{ilk}(\mathbf{x}, \mathbf{x}_0) g_l}{8\pi}, \quad (8)$$

$$\nabla_k T_{ilk} = -8\pi\delta_{il}\delta(\mathbf{x} - \mathbf{x}_0), \quad T_{ilk} = -p_l \delta_{ik} + \nabla_k S_{il} + \nabla_i S_{kl},$$

where  $T_{ilk}$  is a third-rank tensor independent of  $\mathbf{g}$  and we defined the  $\mathbf{g}$ -independent  $p_l$  by  $p^S = \mathbf{p} \cdot \mathbf{g}/(8\pi)$ . We use the Lorentz identity,

$$\nabla_k [u_i \sigma_{ik}^S - u_i^S \sigma_{ik}] + \mathbf{u} \cdot \mathbf{g} \delta(\mathbf{x} - \mathbf{x}_0) = 0, \quad (9)$$

readily inferred from the Stokes equations with  $\sigma_{ik}$  the stress tensor of the flow defined by Eqs. (2),

$$\sigma_{ik} = -p\delta_{ik} + \eta(\nabla_i u_k + \nabla_k u_i). \quad (10)$$

Substituting  $\mathbf{u}^S$  and  $\boldsymbol{\sigma}^S$  from Eqs. (7)-(8) in Eq. (9) and using the above identity we find that,

$$8\pi\eta u_l(\mathbf{x}')\delta(\mathbf{x}' - \mathbf{x}) = \frac{\partial}{\partial x'_k} [S_{il}(\mathbf{x}', \mathbf{x})\sigma_{ik}(\mathbf{x}') - \eta u_i(\mathbf{x}')T_{ilk}(\mathbf{x}', \mathbf{x})]. \quad (11)$$

Integrating this equation over  $\mathbf{x}'$  outside the particles,

$$u_l = f_l - \sum_n \int_{S_n} \frac{S_{il}(\mathbf{x}', \mathbf{x})\sigma'_{ik} dS'_k}{8\pi\eta} + \sum_n \int_{S_n} \frac{u_i(\mathbf{x}')T_{ilk}(\mathbf{x}', \mathbf{x}) dS'_k}{8\pi}, \quad (12)$$

where  $f$  is the integral over the far surface at infinity,  $S_n$  is the surface of the  $n$ -th particle and  $dS_k$  is aligned with the outward normal to the particle surface. There is no contribution from the channel boundaries  $z = 0$  and  $z = h$  since both flows vanish there.

We assume that the particles are confined in a finite region so that the flow far from the particles is the Poiseuille flow given by Eq. (1), see Eq. (2). Since the Stokeslet decays far from the source, the second and the third terms on the RHS of Eq. (12) decay to zero at large distances from the particles. Thus, the asymptotic approach of  $\mathbf{u}$  to the Poiseuille flow at large distances implies the asymptotic equality of  $f$  to the Poiseuille flow. It is readily seen using the asymptotic form of the Stokeslet at large horizontal distances, provided in the next Section, and the asymptotic, Poiseuille, form of the flow, that  $f$  is determined by terms independent of the particles, that is terms that would be the same for the case of no particles. Thus necessarily  $f$  is the Poiseuille flow given by Eq. (1). This is confirmed by the direct calculation in Appendix A. We therefore conclude that,

$$u_l = \frac{\delta_{lx} z(z-h)\nabla_x p^0}{2\eta} - \sum_n \int_{S_n} \frac{S_{il}(\mathbf{x}', \mathbf{x})\sigma'_{ik} dS'_k}{8\pi\eta} + \sum_n \int_{S_n} \frac{u_i(\mathbf{x}')T_{ilk}(\mathbf{x}', \mathbf{x}) dS'_k}{8\pi}. \quad (13)$$

This integral representation of the flow involves no approximations and holds for particles of arbitrary shape. The flow is determined by the values of  $\mathbf{u}$  and  $\sigma_{ik}$  at the particle surface. When the distance between the particles are much larger than their size the hydrodynamic interactions are negligible and  $\mathbf{u}$  and  $\sigma_{ik}$  are approximately those of an isolated particle. However, the current representation works also when the particles are close to each other so that the

hydrodynamic interactions change significantly the values of  $\mathbf{u}$  and  $\sigma_{ik}$  at the particle surface.

*Simplification for rigid surface.*—The integral representation above simplifies in the case of rigid surfaces when the flow on the surface of the particles is the superposition of translation and solid-body rotation. This is not only the case of rigid particles described after Eq. (2), but often also the case of small bubbles where impurities present in the fluid accumulate at the surface making it effectively rigid. In this case, experiments demonstrate that the behavior of these bubbles is similar to that of rigid particles ???. In these and similar cases the flow at the particle surface  $u_i(\mathbf{x}')$  has the form  $c_i + \epsilon_{irm}x'_m\tilde{\mathbf{c}}$  where both  $\mathbf{c}$  and  $\tilde{\mathbf{c}}$  are independent of  $\mathbf{x}'$ . Hence the last term in Eq. (13) drops out because for  $\mathbf{x}$  outside the particle interior  $V_p$ ,

$$\int_{S_p} dS'_k T_{ilk}(\mathbf{x}', \mathbf{x}) = \int_{V_p} dV \nabla'_k T_{ilk} = 0, \quad (14)$$

$$\epsilon_{irm} \int_S dS'_k x'_m T_{ilk}(\mathbf{x}', \mathbf{x}) = \epsilon_{irm} \int_{V_p} dV \delta_{mk} T_{ilk} = 0,$$

cf. ?. Note that we made use of the fact that  $\epsilon_{irm}$  is antisymmetric over indices  $i, m$  whereas  $T_{ilm}$  is symmetric with respect to those indices. We conclude that in the case of many particles with rigid surfaces,

$$u_l = \frac{\delta_{lx} z(z-h) \nabla_x p^0}{2\eta} - \sum_n \int_{S_n} \frac{S_{il}(\mathbf{x}', \mathbf{x}) \sigma'_{ik} dS'_k}{8\pi\eta}, \quad (15)$$

The representations derived here are thus useful to describe the flow.

### 3. Derivation of lubrication theory

In this Section we demonstrate that Eqs. (13) and (15) imply that the predictions of the lubrication theory hold at horizontal distances from the particles larger than  $h$ . This is less restrictive than the usual condition of applicability of the lubrication theory for distances much larger than  $h$ , cf. Sarig *et al.* (2016). This property comes from the Stokeslet flow which obeys the lubrication theory at distances larger than  $h$ . We use the representation

$$S_{il}(\mathbf{x}', \mathbf{x}) = \frac{12z'(h-z')z(z-h)\nabla_i\nabla_l \ln \rho}{h^3} + \tilde{S}_{il}(\mathbf{x}', \mathbf{x}), \quad (16)$$

where  $\rho$  is the length of  $\boldsymbol{\rho} = (x - x', y - y')$  (thus  $\nabla_i \nabla_l \ln \rho = 0$  if one of the indices is  $z$ ). It was observed in ? that  $\tilde{S}_{il}$  decays exponentially in  $\rho$  with exponent at least  $\pi/h$ , that is the smallness is at least  $\exp(-\pi\rho/h)$ . Thus already at  $\rho \approx h$  we can discard the last, non-potential term in Eq. (16). The resulting approximation to the Stokeslet flow,

$$S_{il}(\mathbf{x}', \mathbf{x}) \approx S_{il}^0(\mathbf{x}', \mathbf{x}) = \frac{12z'(h-z')z(z-h)\nabla_i\nabla_l \ln \rho}{h^3}, \quad (17)$$

is the two-dimensional potential flow times  $z'(h-z')$ , in agreement with the predictions of the lubrication theory, see Eq. (3). Note that  $S_{il}^0(\mathbf{x}', \mathbf{x})$  is a symmetric

function of  $\mathbf{x}$  and  $\mathbf{x}'$ , whose dependence on the horizontal coordinates is via the difference  $\rho$  only. We consider the corresponding pressure  $p^0$  that approximately solves the corresponding Stokes equation  $\nabla'_i p_l^0(\mathbf{x}', \mathbf{x}) = \nabla'^2 S_{il}^0(\mathbf{x}', \mathbf{x})$ , see the second of Eqs. (8). Here  $\nabla'_i$  designates the derivative over  $x'_i$  and we do not write the  $\delta(\mathbf{x}' - \mathbf{x})$  term on the RHS. We thus find ( $l \neq z$ ),

$$p_l^0(\mathbf{x}', \mathbf{x}) = \frac{24z(z-h)\rho_l}{h^3\rho^2} = \frac{24z(z-h)}{h^3} \nabla_l \ln \rho. \quad (18)$$

Here,  $p^0$  is the leading order approximation for the pressure of the Stokeslet at large distances ?, with an exponentially small correction. We can write ( $l \neq z$  but  $i$  or  $k$  can be  $z$ ),

$$T_{ilk}(\mathbf{x}', \mathbf{x}) = -p_l^0 \delta_{ik} + \nabla'_k S_{il}^0 + \nabla'_i S_{kl}^0 + \tilde{T}_{ilk}(\mathbf{x}', \mathbf{x}), \quad (19)$$

where  $\tilde{T}_{ilk}(\mathbf{x}', \mathbf{x})$  decays exponentially in  $\rho$  with exponent at least  $\pi/h$ , cf. Eq. (8). The stress tensor  $T_{ilk}(\mathbf{x}', \mathbf{x})$  is exponentially small when one of the indices is  $z$ . We find using the expressions for  $p_0$  and  $S_{il}^0$ ,

$$\begin{aligned} T_{ilk}(\mathbf{x}', \mathbf{x}) &\approx \frac{24z(h-z)}{h^3} \nabla_l [(\delta_{ik} + z'(h-z')\nabla_i \nabla_k) \ln \rho] \\ &+ \frac{12(h-2z')z(z-h)}{h^3} (\delta_{kz}\nabla_i + \delta_{iz}\nabla_k) \nabla_l \ln \rho, \end{aligned} \quad (20)$$

where we neglected exponentially small correction. We find from Eq. (13) that,

$$\mathbf{u}(\mathbf{x}) = \frac{z(z-h)\nabla p}{2\eta} + O\left(e^{-\pi \min[\rho_n]/h}\right); \quad \nabla^2 p = 0, \quad (21)$$

where  $\mathbf{u} = (u_x, u_y)$  and  $\min[\rho_n]$  is the distance from  $\mathbf{x}$  to the closest boundary of a particle. The pressure  $p$  in this formula is independent of  $z$  as predicted by the lubrication theory used in Eq. (3) with,

$$\begin{aligned} p &= p^0 + \sum_n \delta p_n, \quad \delta p_n = \frac{3\nabla_i}{\pi h^3} \int_{S_n} z'(z'-h) \ln \rho \sigma'_{ik} dS'_k \\ &- \frac{6\eta}{\pi h^3} \int_{S_n} dS'_k (\delta_{ik} + z'(h-z')\nabla_i \nabla_k) u_i(\mathbf{x}') \ln \rho \\ &+ \frac{3\eta}{\pi h^3} \int_{S_n} dS'_k (h-2z') (\delta_{kz}\nabla_i + \delta_{iz}\nabla_k) u_i(\mathbf{x}') \ln \rho, \end{aligned} \quad (22)$$

where  $\delta p_n$  is the pressure perturbation due to the  $n$ -th particle and the summation over repeated indices is from 1 to 3. Eqs. (21)-(22) are one of the main results of our work. These provide a refinement of the lubrication theory demonstrating that Eq. (3) holds under the condition  $\exp(-\pi \min[\rho_n]/h) \ll 1$ , which is difficult to show using the classic lubrication theory as it demands the strong inequality  $\min[\rho_n] \gg h$ . For instance, at  $\min[\rho_n] = h$  the exponential factor is  $\sim 0.04$ . The result holds both for droplets and rigid particles where for rigid particles the last two lines of Eq. (22) become zero and the equation

reduces to

$$p = p^0 + \frac{3\nabla_i}{\pi h^3} \sum_n \int_{S_n} z'(z' - h) \ln \rho \sigma'_{ik} dS'_k. \quad (23)$$

We have good control of the correction terms to Eqs. (21)-(23) from the series representation of  $\tilde{S}_{il}(\mathbf{x}', \mathbf{x})$  provided in ?.

The pressure  $p$  solves the two-dimensional Laplace equation in the domain between the particles since it is formed by integrals of the fundamental solution of the Laplace equation  $\ln \rho$  over the particle boundaries. The formula for  $p$  matches the ideal flow that holds beyond the horizontal distance  $h$  from the particles with the fully viscous flow near the particles. The viscous layer is the neighborhood of the boundary of each particle where Eq. (22) breaks down. Though the solution for  $p$  is given in terms of the unknown velocities and stress tensors on the surfaces of the particles, it seems that this is as much as can be done generally: the matching problem is not solvable for any general particle shape. It does simplify for disk-like particles as described previously.

*Hydrodynamic interactions of pancake-like droplets.*—Eqs. (21)-(22) provide support for the observation that the width of the viscous layer around disk-like droplets is not larger than  $h$ . The formulae tell that, unless the distance between the droplet surfaces is smaller than  $h$ , the (horizontal) flow outside the viscous layers near the particles is an ideal potential flow. This flow can be determined using the boundary condition that the normal velocity at the outer boundary of the viscous layer coincides with the normal component of the translational velocity of the particle. Since the layer width is of the order of  $h$ , and as long as the distance between the droplets is larger than  $h$  (but possibly much smaller than  $a$ ) we can impose the boundary condition on the particle surface, neglecting the finite width of this viscous layer as we did for the case of the single large disk, see Eq. (5). Similarly, in the presence of many particles whose separation is larger than  $h$ , the flow outside the boundary layer is described by a pressure field  $p$  that obeys Sarig *et al.* (2016); Beatus *et al.* (2012),

$$\nabla^2 p = 0, \quad \left( \mathbf{v}_n + \frac{h^2 \nabla p}{12\eta} \right) \cdot \hat{n}_n = 0, \quad (24)$$

where  $\mathbf{v}_n$  is the velocity of  $n$ -th particle,  $\hat{n}_n$  is the unit vector normal to the surface of the  $n$ -th particle. The pressure gradient is taken at the outer boundary of the viscous layer of the  $n$ -th particle. However, since the latter is narrow, one can consider  $\nabla p$  on the surface of the  $n$ -th particle without affecting significantly the solution for the pressure outside the viscous layers. To find the pressure inside the layers would require a separate study. For close droplets the pressure determined by Eq. (24) is different from the superposition of the dipole solutions given by Eqs. (4)-(5) due to the near-field interactions.

Finally, we demonstrate that the force exerted on the particles, determined by the viscous stress tensor at the particle surface, can be obtained from the ideal flow description. The force  $\mathbf{F}^n$  on particle  $n$  is determined by the following

integral over the particle surface,

$$\mathbf{F}_i^n = \int_{S_n} \sigma_{ik} dS_k = \int_{outer} \sigma_{ik} dS_k, \quad (25)$$

where the last integral is over the outer boundary of the viscous layer of the  $n$ -th particle and we used  $\nabla_k \sigma_{ik} = 0$ . We can neglect the viscous contribution to the stress tensor at the outer boundary and find

$$\mathbf{F}^n \approx - \int_{outer} p dS \approx - \int_{S_n} p dS, \quad (26)$$

where we must use the pressure  $p$  determined from Eq. (24) in the last term and not the true pressure on the surface of the particle. Thus, the force coincides with that in an ideal flow and, effectively, we can assume that the ideal flow holds everywhere disregarding the no-slip boundary condition. This provides a consistent basis for the study of hydrodynamic interactions between large droplets at small distances as performed in Sarig *et al.* (2016); Beatus *et al.* (2012).

#### 4. Multipole expansion

The flow at large distances from the particles can be effectively studied using the multipole expansion. The distances must be larger than  $h$  and much larger than the particle size. We perform here this expansion in terms of  $\delta p_n$  in Eq. (22), solution of the two-dimensional Laplace equation. We write  $\delta p_n$  as,

$$\begin{aligned} \delta p_n = & \frac{3}{\pi h^3} \int_{S_n} dS'_k (z'(z' - h) \sigma'_{ik} \nabla_i - \eta u_i(\mathbf{x}') (2\delta_{ik} \\ & + 2z'(h-z') \nabla_i \nabla_k + (h-2z') (\delta_{kz} \nabla_i + \delta_{iz} \nabla_k))) \ln \rho. \end{aligned} \quad (27)$$

We provide next the expansion in Cartesian and polar coordinates as in three-dimensional electrostatics ?.

We set the origin of the coordinate system inside the  $n$ -th particle. To determine the multipole expansion in Cartesian coordinates we consider the Taylor series (remind that  $\rho = |\mathbf{r} - \mathbf{r}'|$ ),

$$\ln \rho = \ln r - r'_l \nabla_l \ln r + \frac{r'_l r'_p}{2} \nabla_l \nabla_p \ln r + \dots, \quad (28)$$

where dots stand for higher-order terms. Substituting into Eq. (27) one obtains the Cartesian form of the multipole expansion. The leading-order  $\ln r$  term in the series,

$$\begin{aligned} \delta p_n = & \frac{3}{\pi h^3} \int_{S_n} dS'_k (z'(z' - h) \sigma'_{ik} \nabla_i - \eta u_i(\mathbf{x}') (2\delta_{ik} \\ & + 2z'(h-z') \nabla_i \nabla_k + (h-2z') (\delta_{kz} \nabla_i + \delta_{iz} \nabla_k))) \ln r, \end{aligned} \quad (29)$$

has a contribution proportional to  $\int \mathbf{u} \cdot d\mathbf{S}$ , i.e. proportional to  $\ln r$ . Further assuming the droplet is incompressible  $\int \mathbf{u} \cdot d\mathbf{S} = 0$ . In this case, the leading

order term at larger distances is given by the dipole term,

$$\delta p_n = \frac{3}{\pi h^3} \int_{S_n} dS'_k (z'(z' - h) \sigma'_{ik} \nabla_i - \eta u_i(\mathbf{x}') (h - 2z')) \\ (\delta_{kz} \nabla_i + \delta_{iz} \nabla_k)) \ln r + \frac{6\eta \nabla_l \ln r}{\pi h^3} \int_{S_n} r'_l \mathbf{u} \cdot d\mathbf{S}, \quad (30)$$

where the last term comes from the next-order term in the expansion of the logarithm. This term can be simplified for droplets that do not change their shape, such as the pancake-like droplets considered previously, since the slip and flow on the surface are irrelevant. For instance, for a spherical droplet whose center moves with velocity  $\mathbf{v}$ , one obtains  $\int_{S_n} r'_l \mathbf{u} \cdot d\mathbf{S} = v_k \int_{S_n} r'_l dS_k = 4\pi a^3 v_l / 3$ . The complete expansion becomes,

$$\delta p_n = \frac{3}{\pi h^3} \int_{S_n} dS'_k (z'(z' - h) \sigma'_{ik} \nabla_i - \eta u_i(\mathbf{x}') (2\delta_{ik} \\ + 2z'(h - z') \nabla_i \nabla_k + (h - 2z') (\delta_{kz} \nabla_i + \delta_{iz} \nabla_k))) (\ln r \\ - r'_l \nabla_l \ln r + \frac{r'_l r'_p}{2} \nabla_l \nabla_p \ln r + \dots). \quad (31)$$

The expansion in polar coordinates is found observing that for  $r' < r$ ,

$$\ln |\mathbf{r} - \mathbf{r}'| = \ln r \\ - \sum_{n=1}^{\infty} \left( \frac{r'}{r} \right)^n \frac{\cos(n\theta) \cos(n\theta') + \sin(n\theta) \sin(n\theta')}{n}. \quad (32)$$

This formula represents the fundamental solution  $\ln |\mathbf{r} - \mathbf{r}'|$  in terms of the elementary solutions of Laplace equation,  $r^{-k} \exp(ik\theta)$  and  $r'^p \exp(ip\theta')$  with  $k$  and  $p$  positive integers. This is the counterpart of the expansion of  $|\mathbf{r} - \mathbf{r}'|^{-1}$  in spherical harmonics adopted in three-dimensional multipole expansion in electrostatics ? and, in fact, it can be derived from that expansion by confining  $\mathbf{r}, \mathbf{r}'$  in a plane. We provide here a simpler derivation. We consider,

$$\ln |\mathbf{r} - \mathbf{r}'| = \ln r + \frac{\ln(1 - 2\epsilon \cos \gamma + \epsilon^2)}{2}, \quad \epsilon = \frac{r'}{r}, \quad (33)$$

where  $\gamma$  is the angle between  $\mathbf{r}$  and  $\mathbf{r}'$  and  $\epsilon < 1$ . We recall the Fourier series,

$$\ln(1 - 2\epsilon \cos \gamma + \epsilon^2) = - \sum_{n=1}^{\infty} \frac{2\epsilon^n \cos(n\gamma)}{n} \quad (34)$$

where the integrals for the Fourier coefficients can be obtained using the residue theorem ?. Finally, introducing the polar angles  $\theta$  and  $\theta'$  for  $\mathbf{r}$  and  $\mathbf{r}'$ , respectively, and using  $\gamma = \theta' - \theta$  we obtain Eq. (32). The multipolar expansion in

polar coordinates is finally

$$\begin{aligned} \delta p_n = & \frac{3}{\pi h^3} \int_{S_n} dS'_k (z'(z' - h) \sigma'_{ik} \nabla_i - \eta u_i(\mathbf{x}') (2\delta_{ik} \\ & + 2z'(h-z') \nabla_i \nabla_k + (h-2z') (\delta_{kz} \nabla_i + \delta_{iz} \nabla_k))) (\ln r \\ & - \sum_{n=1}^{\infty} \left( \frac{r'}{r} \right)^n \frac{\cos(n\theta) \cos(n\theta') + \sin(n\theta) \sin(n\theta')}{n} \Big), \end{aligned} \quad (35)$$

which gives the pressure as a superposition of elementary solutions  $r^{-k} \exp(ik\theta)$ . The formulae simplify for rigid particles to

$$\begin{aligned} \delta p_n = & \frac{3}{\pi h^3} \int_{S_n} dS'_k z'(z' - h) \sigma'_{ik} \nabla_i (\ln r \\ & - r'_l \nabla_l \ln r + \frac{r'_l r'_p}{2} \nabla_l \nabla_p \ln r + \dots) \end{aligned} \quad (36)$$

and

$$\begin{aligned} \delta p_n = & \frac{3}{\pi h^3} \int_{S_n} dS'_k z'(z' - h) \sigma'_{ik} \nabla_i (\ln r \\ & - \sum_{n=1}^{\infty} \left( \frac{r'}{r} \right)^n \frac{\cos(n\theta) \cos(n\theta') + \sin(n\theta) \sin(n\theta')}{n} \Big). \end{aligned} \quad (37)$$

The multipole expansion of the flow is derived by taking the gradient of the pressure using Eq. (21). As an example, the perturbation of the Poiseuille flow due to a rigid particle,  $\delta u_k$ , is up to a cubically decaying term,

$$\begin{aligned} \delta u_k = & -\frac{3z(z-h)s_i}{2\pi h^3 \eta} \nabla_k \nabla_i \ln r - \frac{3z(z-h)}{2\pi h^3 \eta} \\ & \times \nabla_k \nabla_i \frac{1}{r} \int_S dS'_k z'(z'-h) \sigma'_{ik} r' \cos(\theta - \theta'), \end{aligned} \quad (38)$$

where we introduced,

$$s_i = \int_S z'(h-z') \sigma'_{ik} dS'_k. \quad (39)$$

The first term in Eq. (38) is a dipole and the second term a quadrupole. Similarly, we can write the corresponding and higher-order terms for droplets.

## 5. Leading-order behavior at large distances

In this Section we consider the leading order behavior of the flow at large horizontal distances from the particle(s). The distances must be larger than  $h$  (but not much larger) and much larger than the size of the particles. The far-field flow perturbation  $\delta \mathbf{u}_n$  due to the  $n$ -th particle is given by the dipole flow,

$$\delta \mathbf{u}_n = \frac{z(z-h)}{2\eta} \nabla \delta p_n, \quad \delta p_n = -\frac{3}{\pi h^3} (\mathbf{s}_n \cdot \nabla) \ln r, \quad (40)$$

where

$$(s_n)_i = \int_{S_n} dS'_k z' (h - z') \sigma'_{ik} + \eta \int_{S_n} dS'_z (h - 2z') u_i(\mathbf{x}') \\ + \eta \int_{S_n} dS'_i (h - 2z') u_z(\mathbf{x}') - 2\eta \int_{S_n} r'_i \mathbf{u} \cdot d\mathbf{S}, \quad (41)$$

see Eqs. (21) and (30). For rigid particles this reduces to Eq. (39) which is why we use the same letter for the coefficient  $s_i$ . We find that the perturbation of the potential of the depth-averaged flow  $\delta\phi_n = -h^2\delta p_n/(12\eta)$  is,

$$\delta\phi_n = -\frac{\tilde{\mathbf{d}}_n \cdot \hat{\mathbf{r}}}{r}, \quad \tilde{\mathbf{d}}_n = -\frac{\mathbf{s}_n}{4\pi\eta h}, \quad (42)$$

see Eq. (4). Thus, the flow perturbation at large distances is the dipolar flow with effective dipole moment  $\tilde{\mathbf{d}}$ . We can describe the far-field impact of a particle of arbitrary shape on the flow introducing the source in the potential equation,  $\nabla^2\delta\phi_n = -2\pi(\tilde{\mathbf{d}}_n \cdot \nabla)\delta(x)\delta(y)$  so that the full potential  $\phi$  obeys,

$$\nabla^2\phi = -2\pi \sum_n (\tilde{\mathbf{d}}_n \cdot \nabla) \delta(x - x_n) \delta(y - y_n) \quad (43)$$

where  $(x_n, y_n)$  are the horizontal coordinates of some point inside the  $n$ -th particle (observe that  $p^0$  is a linear function and has zero laplacian).

The resulting correction to the Poiseuille flow is that of a particle that moves in direction of  $\mathbf{s}$ , see Eq. (5),

$$\delta u_k(\mathbf{x}) = \frac{3s_i z(h-z)}{\pi\eta h^3(x^2 + y^2)} \left[ \frac{\delta_{ik}}{2} - \frac{x_i x_k}{x^2 + y^2} \right], \quad \rho \gg h. \quad (44)$$

The lateral,  $y$  and  $z$ , components of  $\mathbf{s}$  vanish for particles that have fore-and-aft symmetry. This can be shown in the same way as for the absence of lateral migration of spheres in a channel ???. The reversal of the sign of  $\mathbf{u}$  and  $p$  produces another solution of the system of Eqs. (2). This solution has opposite sign of the stress tensor and velocity and thus of  $\mathbf{s}$ . However, it describes the same physical situation and thus must have the same lateral components of  $\mathbf{s}$ , hence these components must vanish. Thus, for spheres or ellipsoids  $\mathbf{s} = s\hat{\mathbf{x}}$ . In contrast, for particles whose shape is an arc or similar one can have a non-zero  $s_y$  and  $s_z$ .

We consider a spherical particle as an example of a particle with fore-and-aft symmetry. We can introduce  $s_i = s(z_p)\delta_{ix}$  where,

$$s(z_p) = \int_S z'(h - z') \sigma'_{xk} dS'_k + \eta \int_{S_n} dS'_z (h - 2z') u_x(\mathbf{x}') \\ + \eta \int_{S_n} dS'_x (h - 2z') u_z(\mathbf{x}') - 2\eta \int_{S_n} r'_x \mathbf{u} \cdot d\mathbf{S}, \quad (45)$$

Table 1: Relative particle velocity  $\delta u_p/U_b$  and magnitude of  $\hat{s}$  as function of the particle centre position  $z_p/h$  for spherical particles of radius  $a = h/6$  obtained from the numerical simulations.

$z_p/h$	0.50	0.55	0.60	0.65	0.70	0.75	0.80
$\delta u_p/U_b$	-0.06	-0.06	-0.06	-0.07	-0.07	-0.09	-0.17
$\hat{s} \times 10^{-3}$	1.8	2.2	3.7	6.3	10.6	17.8	30.0

with  $z_p$  the vertical position of the particle center. In this case, the flow is

$$\begin{aligned}\delta u_x(\mathbf{x}) &= \frac{3s(z_p)z(h-z)}{2\pi\eta h^3(x^2+y^2)} \frac{y^2-x^2}{x^2+y^2}, \\ \delta u_y(\mathbf{x}) &= -\frac{3s(z_p)z(h-z)}{2\pi\eta h^3(x^2+y^2)} \frac{2xy}{x^2+y^2}.\end{aligned}\quad (46)$$

It is plausible that  $s(z_p) > 0$  because the particle is always lagging behind the local flow. This is confirmed by the direct numerical simulations reported below.

The formulas provided here give the possibility of tabulating the particle dipole moments from numerical simulations for future use. For a spherical particle of fixed radius the dipole moment depends on the vertical coordinate  $z_p$ . The solution of the flow equations in the presence of an isolated sphere would give the stress tensor and the surface velocity with which we can find  $s(z_p)$ . We illustrate this procedure for the case where the particle is a rigid sphere with same density as that of the fluid. The equation of motion is,

$$m \frac{dv_i}{dt} = \int_S \sigma_{ik} dS_k, \quad (47)$$

where  $m$  is the mass of the particle and gravity does not influence the motion since the particle is assumed to be neutrally buoyant. This equation is coupled to the time- dependent Navier-Stokes equations where the unsteady term is not negligible during the transients. The particle eventually reaches a constant velocity and the fluid flow is governed by the steady Stokes equations due to the small Reynolds number. Thus, our derivation of the far flow holds with the dipole coefficient for rigid particles,

$$s(z_p) = \int_S z'(h-z') \sigma'_{xk} dS'_k. \quad (48)$$

We computed here  $s(z_p)$  using the numerically determined  $\sigma_{xk}$  for different  $z_p$  and different radii of the sphere. The results are summarized in Tables 1 - 3 (see Appendix B for details). Here, the particle relative velocity, defined as  $\delta u_p = u_p - u_x^0$  where  $u_p$  is the particle center velocity, is non-dimensionalized by the bulk velocity of the undisturbed channel flow  $U_b = -h^2 \nabla_x p^0 / (12\eta)$ . The reduction of the translational velocity as the particle is placed closer to one wall or as the particle size increases is consistent with previous computations using the boundary integral method ?.

Table 2: Relative particle velocity  $\delta u_p/U_b$  and magnitude of  $\hat{s}$  as function of the particle centre position  $z_p/h$  for spherical particles of radius  $a = h/3$  obtained from the numerical simulations.

$z_p/h$	0.50	0.55	0.60	0.65
$\delta u_p/U_b$	-0.24	-0.25	-0.30	-0.45
$\hat{s} \times 10^{-2}$	4.1	4.9	7.6	15.8

Table 3: Relative particle velocity  $\delta u_p/U_b$  and magnitude of  $\hat{s}$  as function of the particle centre position  $z_p/h$  for spherical particles of radius  $a = h/2.25$  obtained from the numerical simulations.

$z_p/h$	0.50
$\delta u_p/U_b$	-0.52
$\hat{s} \times 10^{-1}$	2.1

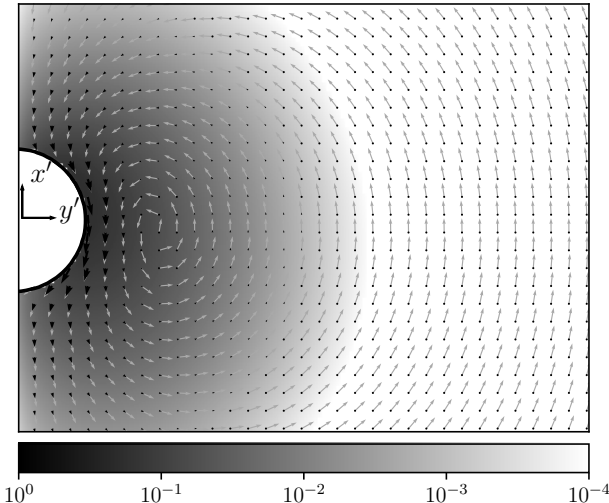


Figure 2: Depth-averaged disturbance flow around a sphere from the numerical simulations. The heavy arrows indicate the magnitude and light arrows the direction. The color in the background depicts the decay of the vorticity outside the sphere. The particle travels in the  $x'$  direction and is located at the mid-channel ( $z_p/h = 0.5$ ), with  $h/(2a) = 1.5$ . Only half of the plane is shown due to symmetry.

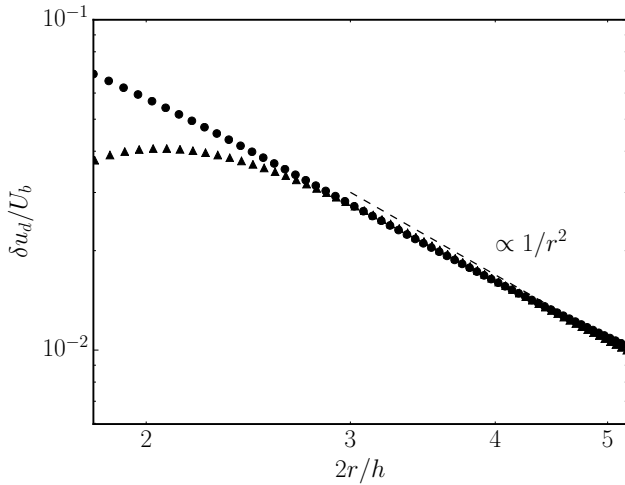


Figure 3: Spatial variation of the normalized streamwise depth-averaged disturbance-velocity,  $\delta u_d/U_b$ , along the streamwise ( $y = 0$ , circle) and spanwise ( $x = 0$ , triangle) directions away from the particle center. The particle is located at the mid-channel ( $z_p/h = 0.5$ ), with  $h/(2a) = 1.125$ . The collapse of the disturbance-velocity away from the particle confirms the leading-order dipolar decay (dashed line).

We also report the values of  $\hat{s}(z_p) = 3s(z_p)/(2\pi\eta h^3)$ , the common pre-factor in Eq. (46). We note that, though overall small,  $\hat{s}$  increases as the particle approaches one wall or as the confinement increases, as the relative velocity  $\delta u_p$ . The resulting  $\hat{s}$ , quantifying the local velocity disturbance generated by one particle, along with the spatial dependence in the horizontal plane, allows for predictions of the far-field interactions of spheres. These will be examined in Section 6.

Finally, we return to the lubrication theory by showing some typical depth-average velocity field in Fig. 2 and the velocity decay in Fig. 3. As mentioned earlier, the lubrication theory is valid at horizontal distances larger than the height of the channel. Fig. 2 depicts the flow field due to a sphere of diameter equal to  $2/3$  of the channel height. The non-zero vertical vorticity outside the particle indicates the non-ideal structure of the depth-average flow, in contrast to the simple mass dipole of a disk (see Eq. 5). However, as the confinement increases, the disturbance velocity asymptotes the leading-order quadratic decay, as shown in Fig. 3.

## 6. Interactions

In this Section, we introduce equations that describe interactions of well-separated particles and solve them in some specific cases. We start by observing

that because of the linearity of the problem, the steady state (horizontal) velocity  $\mathbf{v}_0$  of an isolated particle driven by the Poiseuille flow according to Eq. (2) is given by

$$\mathbf{v}_0 = -\hat{M}\nabla p^0, \quad (49)$$

where we assume  $\mathbf{v}_0$  is a function of  $\nabla p^0$  that can be any constant vector in the plane. Indeed,  $\mathbf{v}_0$  is a linear function of  $\nabla p^0$  that is zero when there is no driving flow. Since  $\hat{M}$  connects the velocity  $\mathbf{v}_0$  with the force per unit volume of the fluid, we call  $\hat{M}$  the mobility matrix though it differs from the more commonly used coefficient between the velocity and the force on the particle  $?$ . The two-by-two mobility matrix  $\hat{M}$  depends on the shape of the particle, whether the particle is rigid or droplet, and the particle position in the channel. The equation neglects gravitational settling, absent for neutrally buoyant particles or particles whose sedimentation is stopped by interactions with the walls, (as the pancake-like droplets) or because settling is negligible at relevant time scales. In cases with sedimentation velocity  $\mathbf{v}_s$  so low that the particle stays in quasi-steady state we have,

$$\mathbf{v}_0 = -\hat{M}(t)\nabla p^0 + \mathbf{v}_s, \quad (50)$$

where the matrix  $\hat{M}(t)$  is determined by the instantaneous configuration in the channel, which may depend on time due to sedimentation.

We next consider interactions of many well-separated particles. The flow induced at the position of the  $i$ -th particle by the other particles is a quasi-Poiseuille flow,

$$\mathbf{u} = \frac{z(z-h)\nabla p}{2\eta}, \quad p = p^0 - \sum_{k \neq i} \frac{3}{\pi h^3} (\mathbf{s}_k \cdot \nabla) \ln |\mathbf{r} - \mathbf{r}_k|, \quad (51)$$

where  $\mathbf{r}_k$  is the horizontal position of the  $k$ -th particle, see Eqs. (21), (40). We observe that we can neglect variations of  $\nabla p$  over the particle since the rest of the particles are well-separated. Thus, at the leading order in large distances between the particles the  $i$ -th particle assumes the horizontal velocity,

$$\frac{d\mathbf{r}_i}{dt} = -\hat{M}_i \nabla \left( p^0 - \sum_{k \neq i} \frac{3}{\pi h^3} (\mathbf{s}_k \cdot \nabla) \ln |\mathbf{r} - \mathbf{r}_k| \right)_{\mathbf{r}=\mathbf{r}_i}, \quad (52)$$

where  $\hat{M}_i$  describes the geometry of the  $i$ -th particle. The sedimentation velocity can be included in a straightforward way. This is the equation that describes the long-range interactions of the particles. The presented derivation avoids the problem with boundary conditions encountered in the derivation of  $?$  for the case of droplets. In that case, the derivation started with the flow induced by other particles at the position of the  $i$ -th particle and not the pressure. Since for particles of finite extent it becomes non-obvious where the three-dimensional flow must be considered, our derivation seems to be useful for a proper consideration of particles whose vertical size is smaller than  $h$ .

We consider the case of spherical particles or droplets of radius  $a$  smaller than  $h/2$ . In this case  $\hat{M}_i$  is  $M(z_i)$  times the unit matrix where the scalar coefficient  $M$  depends on the vertical coordinate  $z_i$  of the  $i$ -th particle. Similarly  $s_k = s(z_k)\hat{x}$  where  $s(z)$  was introduced previously. We find,

$$\dot{\mathbf{r}}_i = -M(z_i)\nabla p^0 + \sum_{k \neq i} \frac{3M(z_i)s(z_k)}{\pi h^3 r_{ik}^2} \left[ \hat{\mathbf{x}} - \frac{2(\mathbf{r}_{ik} \cdot \hat{\mathbf{x}}) \mathbf{r}_{ik}}{r_{ik}^2} \right],$$

where  $\mathbf{r}_{ik} = \mathbf{r}_i - \mathbf{r}_k$ . Thus for pair of particles,

$$\dot{\mathbf{r}} = (M(z_1) - M(z_2))\nabla p^0 + \frac{3\delta_{12}}{\pi h^3 r^2} \left[ \hat{\mathbf{x}} - \frac{2x\mathbf{r}}{r^2} \right], \quad (53)$$

where  $\mathbf{r} = \mathbf{r}_2 - \mathbf{r}_1 = (x, y, z)$  and we introduced,

$$\delta_{12} = M(z_2)s(z_1) - M(z_1)s(z_2). \quad (54)$$

Another case when Eqs. (52) simplify significantly is for pancake-like droplets that almost completely fill the channel in the vertical direction. In this case  $M$  and  $s$  are constant since no variation of the vertical position of the particles is possible. We see immediately that the configuration of two droplets is stable in the dipole approximation where  $\dot{\mathbf{r}}$  in Eq. (53) is zero (in a higher-order quadrupole approximation proportional to  $r^{-3}$  the pair would not be stable). For many particles, the equations of motion in the frame that moves with the velocity of the isolated droplet  $-M\nabla p^0$  become,

$$\frac{d\mathbf{r}_i}{dt} = \sum_{k \neq i} \frac{q}{r_{ik}^2} \left[ \hat{\mathbf{x}} - \frac{2(\mathbf{r}_{ik} \cdot \hat{\mathbf{x}}) \mathbf{r}_{ik}}{r_{ik}^2} \right], \quad q = \frac{3Ms}{\pi h^3}. \quad (55)$$

These equations hold also for spherical particles located at the same distance from the mid-plane where we must use for  $M$  and  $s$  the values at the corresponding  $z$ . This is the case where the particles have identical vertical coordinate or their coordinates can be obtained by reflection with respect to the mid plane. Other cases of symmetric particles where Eq. (55) hold can be considered. If gravitational settling is relevant,  $\mathbf{r}_{ik}$  will change via time-dependent  $s = s(z(t))$ . It is assumed below that the change of  $s = s(z(t))$  can be neglected over the time scales of interest.

It is often the case that we have two spherical particles at the same vertical distance from the walls. This can be the case of spherical droplets created at some fixed place in the channel and then transported down the flow ?. In this case, an isolated pair is stable in the dipole approximation: we have  $\dot{\mathbf{r}} = 0$  in Eq. (53) for  $z_1 = z_2$ .

This characterizes the basic property of the interaction given by Eq. (55), that the velocity induced by particle  $i$  at the position of the  $k$ -th particle is equal to the velocity induced by particle  $k$  at the position of the  $i$ -th particle. Thus the interparticle distances can change only if there are three or more

particles. We can re-write the equation of motion as

$$\frac{d\mathbf{r}_{ik}}{dt} = \sum_{l \neq i, l \neq k} \left( \frac{q}{r_{il}^2} \left[ \hat{\mathbf{x}} - \frac{2(\mathbf{r}_{il} \cdot \hat{\mathbf{x}}) \mathbf{r}_{il}}{r_{il}^2} \right] - \frac{q}{r_{kl}^2} \left[ \hat{\mathbf{x}} - \frac{2(\mathbf{r}_{kl} \cdot \hat{\mathbf{x}}) \mathbf{r}_{kl}}{r_{kl}^2} \right] \right). \quad (56)$$

We start by considering in more detail the simplest case of two particles whose distance is constant in time. If the particles have the same  $y$ -coordinate then the  $x$ -coordinates obey,

$$\frac{dx_1}{dt} = \frac{dx_2}{dt} = -\frac{q}{(x_1 - x_2)^2}. \quad (57)$$

In this case the particles form a simple cluster with fixed distance that moves as a whole slower than the particles separately. We consider now two particles at different spanwise locations,  $y_1 = y$ ,  $y_2 = 0$ ,

$$\begin{aligned} \frac{dx_1}{dt} &= \frac{dx_2}{dt} = q \frac{(y_1 - y_2)^2 - (x_1 - x_2)^2}{[(x_1 - x_2)^2 + (y_1 - y_2)^2]^2}, \\ \frac{dy_1}{dt} &= \frac{dy_2}{dt} = -q \frac{2(x_1 - x_2)(y_1 - y_2)}{[(x_1 - x_2)^2 + (y_1 - y_2)^2]^2}. \end{aligned} \quad (58)$$

The RHSs are constant because inter-particle distances are but the velocity of the cluster of the two particles can change sign unlike the previous case. For two particles with the same  $x$  coordinate, the  $x$ - component of their velocity increases while the  $y$ -component is zero, see ? for experimental observations.

Next, we consider the simplest case with changing inter-particle distances: three particles at the same height. From the analysis of the two-particle dynamics, a possible solution is that particles form a cluster of two particles with the third farther away. The interactions of the single distant particle with the clustered particles decay quadratically with the distance and can be assumed negligible. Thus, the isolated particle moves with the velocity of one single sphere. The cluster keeps its configuration and moves at a constant velocity  $(q/r^2)[\hat{\mathbf{x}} - 2(\mathbf{r} \cdot \hat{\mathbf{x}}) \mathbf{r}/r^2]$  with respect to the third particle. If this velocity is such to increase the separation between the cluster and the third particle, this solution will continue ad infinitum. It is thus plausible to assume that any arbitrary initial configuration of three particles will separate asymptotically in one cluster and one particle. We will prove this below for the practically important case of three particles aligned in the streamwise,  $x$ -, direction. This case can be observed when the particles are injected in the flow at the same location.

The distances between three particles are determined by two vectors  $\mathbf{r}_{12}$  and  $\mathbf{r}_{13}$  that obey,

$$\begin{aligned}\dot{\mathbf{r}}_{12} &= \frac{q}{r_{13}^2} \left[ \hat{\mathbf{x}} - \frac{2(\mathbf{r}_{13} \cdot \hat{\mathbf{x}}) \mathbf{r}_{13}}{r_{13}^2} \right] - \frac{q}{r_{23}^2} \left[ \hat{\mathbf{x}} - \frac{2(\mathbf{r}_{23} \cdot \hat{\mathbf{x}}) \mathbf{r}_{23}}{r_{23}^2} \right], \\ \dot{\mathbf{r}}_{13} &= \frac{q}{r_{12}^2} \left[ \hat{\mathbf{x}} - \frac{2(\mathbf{r}_{12} \cdot \hat{\mathbf{x}}) \mathbf{r}_{12}}{r_{12}^2} \right] - \frac{q}{r_{23}^2} \left[ \hat{\mathbf{x}} - \frac{2(\mathbf{r}_{23} \cdot \hat{\mathbf{x}}) \mathbf{r}_{23}}{r_{23}^2} \right].\end{aligned}\quad (59)$$

The solution described above pertaining the cluster of two particles (named here 2 and 3) and the faraway particle 1 corresponds to neglecting the first terms in the RHSs,

$$\dot{\mathbf{r}}_{12} \approx \dot{\mathbf{r}}_{13} \approx -\frac{q}{r_{23}^2} \left[ \hat{\mathbf{x}} - \frac{2(\mathbf{r}_{23} \cdot \hat{\mathbf{x}}) \mathbf{r}_{23}}{r_{23}^2} \right] \approx \text{const}, \quad (60)$$

where  $\mathbf{r}_{23}$  is approximately constant. At large times the constant vector  $\mathbf{r}_{23}$  has become much smaller than the linearly growing  $\mathbf{r}_{12}$  and  $\mathbf{r}_{13}$ . We have that  $\mathbf{r}_{23} = \mathbf{r}_{13} - \mathbf{r}_{12}$  obeys the equation,

$$\dot{\mathbf{r}}_{23} = \frac{q}{r_{12}^2} \left[ \hat{\mathbf{x}} - \frac{2(\mathbf{r}_{12} \cdot \hat{\mathbf{x}}) \mathbf{r}_{12}}{r_{12}^2} \right] - \frac{q}{r_{13}^2} \left[ \hat{\mathbf{x}} - \frac{2(\mathbf{r}_{13} \cdot \hat{\mathbf{x}}) \mathbf{r}_{13}}{r_{13}^2} \right],$$

where the RHS decays quadratically with time, in agreement with the assumption of constant  $\mathbf{r}_{23}$ .

We prove that the separation of 3 particles into one binary cluster and one isolated particle holds for arbitrary initial conditions when all three particles lie on the same line in the  $x$ -direction. It is clear that the separation can occur in two ways in this case: either particles 1 and 2 form a cluster or 2 and 3. Here we assume the ordering  $x_1 > x_2 > x_3$ . As the cluster moves slower than the isolated particle, the third particle would catch up with the binary cluster, made of 1 and 2. Hence the only stable configuration is a cluster of particles 2 and 3 whose distance from particle 1 increases linearly with time due to the cluster deceleration. Formally,

$$\begin{aligned}\dot{x}_{12} &= -q \left( \frac{1}{x_{13}^2} - \frac{1}{(x_{13} - x_{12})^2} \right), \\ \dot{x}_{13} &= -q \left( \frac{1}{x_{12}^2} - \frac{1}{(x_{13} - x_{12})^2} \right).\end{aligned}$$

Introducing  $x = x_{12}$  and  $r = x_{13}/x_{12}$  where  $r > 1$ , we can write

$$\begin{aligned}\dot{x} &= -\frac{q}{x^2} \left( \frac{1}{r^2} - \frac{1}{(r-1)^2} \right) = -\frac{q(1-2r)}{x^2 r^2 (r-1)^2}, \\ \dot{x} + \frac{x\dot{r}}{r} &= -\frac{q}{x^2} \left( \frac{1}{r} - \frac{1}{r(r-1)^2} \right).\end{aligned}\quad (61)$$

The distance  $r$  obeys,

$$\begin{aligned} x^3 \dot{r} &= -q \left( 1 - \frac{1}{(r-1)^2} \right) + q \left( \frac{1}{r} - \frac{r}{(r-1)^2} \right) \\ &= -\frac{q(r-1)}{r} - \frac{q}{r-1} = -\frac{q(r^2-r+1)}{r(r-1)}. \end{aligned} \quad (62)$$

Hence  $r(t)$  decreases in time monotonously and we can write

$$\begin{aligned} \frac{d \ln x}{ds} &= q \left( \frac{1}{(r-1)^2} - \frac{1}{r^2} \right), \\ \frac{dr}{ds} &= -\frac{q(r^2-r+1)}{r(r-1)}, \quad \frac{ds}{dt} = \frac{1}{x^3(t)}. \end{aligned} \quad (63)$$

We can solve for  $s(r)$ ,

$$\begin{aligned} \frac{ds}{dr} &= -\frac{1}{q} + \frac{1}{q(r^2-r+1)}, \quad s(r) = \frac{r_0 - r}{q} \\ &+ \frac{2}{q\sqrt{3}} \arctan \left( \frac{2r-1}{\sqrt{3}} \right) - \frac{2}{q\sqrt{3}} \arctan \left( \frac{2r_0-1}{\sqrt{3}} \right), \end{aligned} \quad (64)$$

where  $r_0 = r(s=0)$ . The inversion of this formula, to find  $r(s)$ , gives a transcendental equation. However, the asymptotic properties of the solution can be derived without solving the equation. When  $s$  increases,  $r$  decreases reaching  $r = 1$  at a finite value  $s = s_*$  where,

$$s_* = \frac{r_0 - 1}{q} + \frac{\pi}{3q\sqrt{3}} - \frac{2}{q\sqrt{3}} \arctan \left( \frac{2r_0 - 1}{\sqrt{3}} \right). \quad (65)$$

The situation of  $r$  reaching 1 would correspond to coalescence of the second and the third particles. This happens only asymptotically, as  $s = s_*$  corresponds to infinite physical time,  $t(s_*) = \infty$ . We have directly from Eq. (64) that  $s'(r=1) = 0$  and  $s'' = (1-2r)/[q(r^2-r+1)^2]$  which gives,

$$\begin{aligned} s(r) &\approx s_* + (r-1)s'(r=1) + \frac{(r-1)^2 s''(r=1)}{2} \\ &= s_* - \frac{(r-1)^2}{2q}, \quad (r-1)^2 = 2q(s_* - s). \end{aligned} \quad (66)$$

We can find  $x$  as a function of  $r$  observing that,

$$\frac{d \ln x}{dr} = \frac{d \ln x}{ds} \frac{ds}{dr} = - \left( \frac{1}{r-1} + \frac{1}{r} \right) \frac{1}{r^2-r+1}. \quad (67)$$

Integration of the above gives (with  $x_0 = x(t=0)$ ),

$$\ln \left( \frac{x}{x_0} \right) = \ln \frac{r_0(r_0-1)}{r_0^2-r_0+1} - \ln \frac{r(r-1)}{r^2-r+1}, \quad (68)$$

where we used,

$$\int \left( \frac{1}{r-1} + \frac{1}{r} \right) \frac{1}{r^2-r+1} dr = \ln \frac{r(r-1)}{r^2-r+1}. \quad (69)$$

We find from Eq. (68) that,

$$x = x_0 \frac{r_0(r_0 - 1)(r^2 - r + 1)}{r(r - 1)(r_0^2 - r_0 + 1)}. \quad (70)$$

In the limit of large times where  $r$  approaches 1 from above we have,

$$x \approx \frac{r_0(r_0 - 1)x_0}{(r - 1)(r_0^2 - r_0 + 1)} \approx \frac{r_0(r_0 - 1)x_0}{(r_0^2 - r_0 + 1)\sqrt{2q(s_* - s)}}, \quad (71)$$

where we used Eq. (66). Finally we restore the physical time using,

$$\frac{dt}{ds} = x^3(s) \approx \frac{r_0^3(r_0 - 1)^3 x_0^3}{(r_0^2 - r_0 + 1)^3 (2q)^{3/2} (s_* - s)^{3/2}}, \quad (72)$$

and obtain,

$$t(s) \approx \frac{r_0^3(r_0 - 1)^3 x_0^3}{q(r_0^2 - r_0 + 1)^3 \sqrt{2q(s_* - s)}}. \quad (73)$$

We conclude from Eqs. (66), (71) that the long-time asymptotic form of the solution is,

$$x(t) = \frac{qt(r_0^2 - r_0 + 1)^2}{r_0^2(r_0 - 1)^2 x_0^2}, \quad r(t) = 1 + \frac{x_0^3 r_0^3 (r_0 - 1)^3}{qt(r_0^2 - r_0 + 1)^3}. \quad (74)$$

This implies that the distance between the second and the third particles reaches a constant value at large times,

$$\begin{aligned} x_{23}(t) &= x(t)(r(t) - 1) \approx \frac{x_0 r_0 (r_0 - 1)}{r_0^2 - r_0 + 1} \\ &= \frac{x_{13}(0)x_{23}(0)x_{12}(0)}{x_{13}(0)x_{23}(0) + x_{12}^2(0)}. \end{aligned} \quad (75)$$

To conclude, we can write,

$$x(t) = \frac{qt}{x_{23}^2}, \quad (76)$$

in agreement with the form given by Eq. (60). This relation proves the separation in cluster and faraway particle and provides the distance between the particles in the cluster as function of the initial conditions.

The obtained formulas provide a theoretical explanation for the pair exchange observed in the experiments by ?, and confirmed by numerical simulations as illustrated in Fig. 4. We consider initial conditions for which particles 1 and 2 are close and the third particle is trailing behind. In this case  $x_{12}^2(0) \ll x_{13}(0), x_{23}(0)$  and Eq. (75) becomes,

$$x_{23}(t) = x_{12}(0). \quad (77)$$

Thus, for long times the distance between the third and the second particle becomes equal to the initial distance between the first and the second particle, that is an exchange takes place.

We can also prove the separation in one cluster and one faraway particle for initial conditions where the particles are "almost" aligned, i.e.  $y_{12}$  and  $y_{13}$

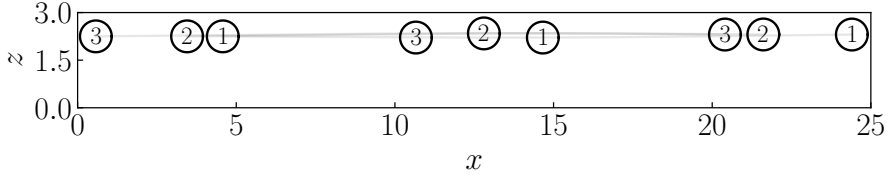


Figure 4: Pair exchange phenomenon as obtained from numerical simulations. Initially particles 1 are 2 are close and particle 3 is trailing behind the pair. As a result of hydrodynamic interactions the trailing particle is catching up with the pair, while the leading particle breaks away from the newly formed pair, whereas the trailing particles 2 and 3 are separated by the same distance as 1 and 2 were initially.

are much smaller than the smallest of  $x_{12}$  and  $x_{13}$ . If the  $y$ -components of the particle positions are linearly ordered, the equations for  $x_{ik}$  do not change and the evolution of  $x_{ik}$  is as above. The  $y$ -components obey,

$$\begin{aligned}\dot{y}_{12} &= -\frac{2qy_{13}}{x_{13}^3} + \frac{2qy_{23}}{(x_{13} - x_{12})^3}, \quad \dot{y}_{23} = \frac{2qy_{13}}{x_{13}^3} - \frac{2qy_{12}}{x_{12}^3} \\ \dot{y}_{13} &= -\frac{2qy_{12}}{x_{12}^3} + \frac{2qy_{23}}{(x_{13} - x_{12})^3},\end{aligned}\tag{78}$$

where  $x_{ik}(t)$  are determined from the previous solution. Since  $x_{12}$ ,  $x_{13}$  grow linearly with time at large times then the asymptotic form of the solution is,

$$y_{12} = y_{13} = \frac{2qct}{x_0^3}, \quad y_{23} = c = \text{const.}$$

This solution indicates that the first particle separates from the binary cluster at constant small but finite angle  $\phi$  with respect to the  $x$ -direction given by,

$$\phi = \frac{y_{12}}{x_{12}} \approx \frac{y_{13}}{x_{13}} \approx \frac{c}{x_0 \sqrt{2}},\tag{79}$$

Self-consistency with the assumption of smallness of  $y_{ik}$  demands that  $c \ll x_0$ . This assumption can be guaranteed by the smallness of the initial conditions on  $y_{ik}$  because of the linearity of the equations in  $y_{ik}$ .

Thus we demonstrated the for initial conditions where the particles are aligned in the  $x$ -direction, or almost aligned, the solution at large times takes the form of a cluster of particles 2 and 3, those two initially upstream, with constant distance  $r_{23}$  and the first particle separating from the cluster according to Eq. (60).

We formulate the hypothesis that any arbitrary initial configuration of three particles will lead at large times to a binary cluster and the third particle linearly separating from it. It seems that the evolution from any arbitrary initial conditions cannot be solved analytically, but only numerically: a reduction from

four to three degrees of freedom can be obtained, but the resulting equations could not be solved.

To conclude, we describe the properties of cluster solutions assuming constant  $\mathbf{r}_{23}$ , of magnitude  $r_{23}$ , and angle  $\phi$  with respect to the  $x$ -axis. Using Eq. (60), we write

$$\dot{x}_{12} \approx \dot{x}_{13} \approx \frac{q \cos(2\phi)}{r_{23}^2}, \quad \dot{y}_{12} \approx \dot{y}_{13} \approx \frac{q \sin(2\phi)}{r_{23}^2}.$$

We can assume with no loss of generality that  $x_2 \geq x_3$  so that  $\phi$  is in the range  $-\pi/2 \leq \phi \leq \pi/2$ . Four different solutions can therefore be identified, assuming the cluster at large time can be denoted as a point at the origin. In the range  $0 \leq \phi \leq \pi/4$  the first particle leaves the cluster behind when going to infinity inside the first quadrant. In the range  $-\pi/4 \leq \phi \leq 0$ , the first particle leaves the cluster behind when going to infinity inside the second quadrant. In the case of  $\pi/4 \leq \phi \leq \pi/2$  the cluster leaves the first particle behind and to the right. Finally in the case of  $-\pi/2 \leq \phi \leq -\pi/4$  the cluster leaves the first particle behind and to the left.

It is clear from the above that the configuration with distant pairs or singlets of particles is stable: the singlets separate ballistically from the stable pairs which maintain the pair distance constant. In contrast, clusters of three and probably more particles are unstable. Thus, we conjecture that under arbitrary initial conditions an arbitrary number of distant particles will separate at large times into a collection of singlets and pairs if the solution is dilute. For suspensions of many particles this implies that hydrodynamic interactions increase the probability of particles to be isolated or in pairs, rather than forming clusters composed of many particles. In dense suspensions, the interactions discussed above do not have time to occur and we rather expect chaotic collisions of particles ?.

## 7. Concluding remarks

In the present paper, we provided a boundary integral representation for the flow due to particles (rigid ones or droplets) freely-suspended in a channel flow. The particle number, size and shape and the inter-particle distances are arbitrary. We have thus demonstrated the utility of this representation.

For an isolated particle, the proposed representation is useful for the study of the far-field flow. At the leading order, the far flow is dipolar flow with the dipole moment given by a weighted integral of the stress tensor and the flow over the particle surface. This defines the far flow completely. The flow was previously available only for strongly confined pancake-like droplets that almost block the channel in the vertical direction. We also determine the dipole moment integral numerically for neutrally buoyant rigid sphere. Further, we provide the multipole expansion from which the far flow can be found with any desired accuracy.

For close particles, the representation is helpful for the study of hydrodynamic interactions. It demonstrates clearly that the range of validity of the lubrication theory is larger than expected from the usual approach ?????. Our representation also solves the problem of matching the ideal flow holding far from the particles with the fully viscous flow near the particle surface. The solution is expressed in terms of the unknown surface velocity and stress tensor. This sheds light on the use of the ideal flow approximation in previous works on disk-like particles ?Sarig *et al.* (2016) and helps to consider particles of other shapes.

We introduced the equation of motion of particles interacting at long distances, refining previous derivation for droplets ? and extending it to the case of arbitrary, possibly different, interacting particles. We solved the three-body problem of hydrodynamic interactions for the case of identical symmetric particles aligned in the stream-wise direction. This solution provides theoretical support for the pair exchange phenomenon observed previously in experiments ?. We provide special solutions for the three-body problem and demonstrate that it is plausible that these solutions describe the long-time asymptotic evolution for arbitrary initial conditions. We further demonstrate the application of the theory to the many body problem.

We did not consider potential lateral migration induced by hydrodynamic interactions. It can be readily seen that a pair of distant spherical particles with different vertical coordinates will separate laterally because the coordinate-dependent mobility matrices and dipole moments will differ for these particles. The study of this instability will be the object of future work.

The representation proposed here is a good starting point for a mean-field description of strong hydrodynamic interactions of close particles. We notice after Eq. (15) that the effect of the interactions can be described by a change of the stress-tensors and velocities at the particle surfaces. Thus the model description of the interaction boils down to the model description of surface stress tensors and velocity. This can be done by introducing the mean field  $\nabla p$  whose direction can differ from the direction of the undisturbed flow. We assume that the stress tensor and flow on the surface of each particle is that for an isolated particle in the Poiseuille flow with pressure gradient  $\nabla p$  (e.g., the particle velocity is equal to minus the mobility matrix times  $\nabla p$ ). Using this in Eq. (15) one can find the flow in terms of  $\nabla p$ . A closed integral equation for  $\nabla p$  can then be obtained from the Stokes flow equations. The study of this equation is planned as future work.

This study was majorly motivated by recent experiments on the formation of droplet clusters in a microfluidic channel ?. The theoretical modeling in ? assumed that flow-assisted clustering of weakly confined spherical droplets in close proximity is driven by the combination of non-hydrodynamic (adhesive, e.g., depletion forces) and hydrodynamic interactions of dipolar nature similar to interactions of strongly confined (pancake-like) droplets in Hele-Shaw cells. The qualitative agreement between the results of the numerical simulations and

experimental results in ? suggested that *ad hoc* modeling of hydrodynamic interactions by dipolar flow is admissible. The present study shows that far-field interactions of weakly confined droplets are indeed of dipolar nature, however their magnitude is too weak to lead to relative motion between freely suspended particles on the time scale of the experiment. Moreover, the present study, as well as the calculations of the interactions at small distances in Beatus *et al.* (2012); Sarig *et al.* (2016), suggest that hydrodynamic interactions at close proximity cannot be described by dipolar flows. We thus believe that the reason for the qualitative agreement between the numerical results and the experiment (using unknown magnitude of the adhesive forces as an adjustable parameter) is that the adhesive force diverges at contact dominating the particle dynamics. The dipolar hydrodynamic interactions provided the source of sliding (tangential) motions of the particles necessary for the particle rearrangement and not provided by the adhesive (radial) forces. However, the particular functional form (e.g., dipolar or other) of these interactions seems to be of minor importance as long as these provide some tangential mobility. An accurate *quantitative* predictive theory of flow-assisted clustering requires the knowledge of the near-field hydrodynamic interactions, including an accurate treatment of the non-uniform flow near the inlet. This will be the object of a future work.

## Acknowledgement

The work is supported by the Microflusa project. The Microflusa project receives funding from the European Union Horizon 2020 research and innovation programme under Grant Agreement No. 664823.

## Appendix A. Calculation of the far-field term $f_l(\mathbf{x}_0)$

In this appendix, we present a direct calculation of the far-field term  $f_l(\mathbf{x}_0)$  in Eq. (12). We find from volume integration of Eq. (11) the boundary term,

$$\begin{aligned}
f_l(\mathbf{x}_0) = & \frac{1}{8\pi\eta} \int_{-L}^L dy \int_0^h dz [S_{il}(L-x_0, y-y_0, z, z_0) \\
& \sigma_{ix}(L, y, z) - S_{il}(-L-x_0, y-y_0, z, z_0)\sigma_{ix}(-L, y, z)] \\
& + \frac{1}{8\pi\eta} \int_{-L}^L dx \int_0^h dz [S_{il}(x-x_0, L-y_0, z, z_0) \\
& \sigma_{iy}(x, L, z) - S_{il}(x-x_0, -L-y_0, z, z_0)\sigma_{iy}(x, -L, z)] \\
& - \frac{1}{8\pi} \int_{-L}^L dy \int_0^h dz [T_{ilx}(L-x_0, y-y_0, z, z_0)u_i(L, y, z) \\
& - T_{ilx}(-L-x_0, y-y_0, z, z_0)u_i(-L, y, z)] - \frac{1}{8\pi} \\
& \times \int_{-L}^L dx \int_0^h dz [T_{ily}(x-x_0, L-y_0, z, z_0)u_i(x, L, z) \\
& - T_{ily}(x-x_0, -L-y_0, z, z_0)u_i(x, -L, z)]; \quad L \rightarrow \infty.
\end{aligned}$$

The Stokeslet decays exponentially in the  $z$ -direction so  $f_z = 0$ . To find the remaining components we use

$$\sigma_{ix}(L, y, z) = -L \nabla_x p^0 \delta_{ix} + \frac{(2z - h) \nabla_x p^0 \delta_{iz}}{2}. \quad (80)$$

We find that  $f_x$  is determined by the asymptotic solution for channel flow and is not affected by the presence of the spherical particle,

$$\begin{aligned} f_x(\mathbf{x}_0) = & -\frac{L \nabla_x p^0}{8\pi\eta} \int_{-L}^L dy \int_0^h dz [S_{xx}(L, y - y_0, z, z_0) \\ & + S_{xx}(-L, y - y_0, z, z_0)] \\ & -\frac{\nabla_x p^0}{8\pi\eta} \int_{-L}^L dx \int_0^h dz x [S_{yx}(x - x_0, L, z, z_0) \\ & - S_{yx}(x - x_0, -L, z, z_0)] \\ & -\frac{1}{8\pi} \int_{-L}^L dy \int_0^h dz \frac{z(z - h) \nabla_x p^0}{2\eta} [T_{xxx}(L, y - y_0, z, z_0) \\ & - T_{xxx}(-L, y - y_0, z - z_0)] \\ & -\frac{1}{8\pi} \int_{-L}^L dx \int_0^h dz \frac{z(z - h) \nabla_x p^0}{2\eta} [T_{xyy}(x - x_0, L, z, z_0) \\ & - T_{xyy}(x - x_0, -L, z - z_0)]; \quad L \rightarrow \infty. \end{aligned} \quad (81)$$

Thus, this must be the unperturbed channel flow as readily verified. Rescaling the integration variable by  $L$  and keeping leading order terms we have,

$$\begin{aligned} f_x(\mathbf{x}_0) = & -\frac{L^2 \nabla_x p^0}{8\pi\eta} \int_{-1}^1 dy \int_0^h dz [S_{xx}(L, Ly, z, z_0) \\ & + S_{xx}(-L, Ly, z, z_0)] \\ & -\frac{L^2 \nabla_x p^0}{8\pi\eta} \int_{-1}^1 dx \int_0^h dz x [S_{yx}(Lx, L, z, z_0) \\ & - S_{yx}(Lx, -L, z, z_0)] \\ & -\frac{L}{8\pi} \int_{-1}^1 dy \int_0^h dz \frac{z(z - h) \nabla_x p}{2\eta} [T_{xxx}(L, Ly, z, z_0) \\ & - T_{xxx}(-L, Ly, z - z_0)] \\ & -\frac{L}{8\pi} \int_{-1}^1 dx \int_0^h dz \frac{z(z - h) \nabla_x p}{2\eta} [T_{xyy}(Lx, L, z, z_0) \\ & - T_{xyy}(Lx, -L, z - z_0)]. \end{aligned} \quad (82)$$

So far the calculation involved the complete Stokeslet solution. To determine  $f_i$  we can use the asymptotic form of the Stokeslet at large distances, which is for the stress tensor,

$$T_{ilk} = -24 \frac{r_l}{\rho^2} (z_0/h^2) (1 - z_0/h) \delta_{ik} + O\left(\frac{1}{\rho^2}\right). \quad (83)$$

Using these formulas for  $S_{ik}$  and  $T_{ilk}$ , one can write

$$\begin{aligned} f_x &= \frac{\nabla_x p^0}{8\pi\eta} \int_{-1}^1 dy \int_0^h dz \frac{24z(z-h)z_0(z_0-h)(y^2-1)}{(1+y^2)^2 h^3} \\ &\quad - \frac{\nabla_x p}{4\pi\eta} \int_{-1}^1 dx \int_0^h dz x^2 \left[ \frac{24z(z-h)z_0(z_0-h)}{(1+x^2)^2 h^3} \right] \\ &\quad - \frac{1}{4\pi} \int_{-1}^1 dy \int_0^h dz \frac{z(z-h)\nabla_x p}{2\eta} \left[ 24 \frac{z_0(z_0-h)}{(1+y^2)h^3} \right]. \end{aligned}$$

Integrating over  $z$ , this can be written as,

$$\begin{aligned} f_x &= \frac{\nabla_x p z_0(z_0-h)}{2\eta} \left( \int_{-1}^1 \frac{dy}{\pi(1+y^2)} \left[ \frac{2}{1+y^2} - 1 \right] \right. \\ &\quad \left. + \frac{1}{\pi} \int_{-1}^1 dx \frac{2x^2}{(1+x^2)^2} + \frac{1}{\pi} \int_{-1}^1 dy \left[ \frac{1}{(1+y^2)} \right] \right). \end{aligned} \quad (84)$$

Performing the integrals we confirm that indeed  $f_x$  is the flow given by Eq. (1).

## Appendix B. Numerical integration of $s$

We compute the weighted dipole moment  $\mathbf{s}$  in Eq. (39) by directly simulating a rigid spherical particle of radius  $a$  transported in a doubly-periodic channel using the immersed boundary method (IBM), see ??? for more details and validations.

In the IBM, there are two meshes; one Eulerian mesh for the flow and one Lagrangian mesh for the moving particle. The two meshes are coupled through a multidirect forcing scheme that ensures the approximate no-slip/no-penetration condition on the particle surface.

The motion of the particle is described by the Newton-Euler equations, given for the translational velocity by Eq. (47)). The equation does not contain the gravitational force which is assumed to be balanced either by the particle interactions with the bottom wall (the case of particle near the wall) or by buoyancy (the case of density-matched particle). We also assume that particle-wall collisions are absent (*cf.* Eq. (3a) in ?).

The flow outside the particle is governed by the incompressible Navier-Stokes (NS) equations with the no-slip boundary conditions on the surface of the rigid particle described in connection with Eq. (2). Although the steady state flow obeys the Stokes equations, computation of the transients demands inclusion of the time derivative in the NS equations. In our simulations, the full NS equations are computed at a small Reynolds number ( $\sim 10^{-1}$ ), *viz.*

$$Re \left( \frac{\partial \mathbf{u}}{\partial t} + \nabla \cdot (\mathbf{u} \mathbf{u}) \right) = \nabla \cdot \boldsymbol{\sigma} + \mathbf{f}, \quad (85)$$

where  $Re = \rho_f U_b (2a)/\eta$  is the Reynolds number,  $U_b$  the channel bulk velocity,  $\rho_f$  ( $= \rho_p$ ) the fluid density and  $\mathbf{f}$  the IBM force enforcing that the no-slip boundary condition (in this formulation pressure is rescaled by  $Re$ .) We discretize these

equations using a second-order finite volume scheme. Finding the flow at given translational and rotational particle velocities we obtain the viscous stress which is used for updating these velocities as in Eq. (47). Numerically, the LHS of Eq. (47) is computed at each time step by summing the forces exerted on all the Lagrangian points, in addition to the volumetric forces inside the particle (see Eq. (8a) in ? for the full expression). In our case, this is simply

$$m \frac{d\mathbf{v}}{dt} \approx - \sum_{l=1}^{N_l} \mathbf{F}_l \Delta V_l + \rho_f \frac{d}{dt} \left( \int_{V_p} \mathbf{u} dV \right), \quad (86)$$

where  $-\mathbf{F}_l$  the force acting on the  $l$  Lagrangian point centred at a shell element of volume  $\Delta V_l$ , and  $N_l$  the total number of Lagrangian points.

At the steady state,

$$\int_S \boldsymbol{\sigma} \cdot d\mathbf{S} \approx - \sum_{l=1}^{N_l} \mathbf{F}_l \Delta V_l, \quad (87)$$

corresponding to the solution of the steady state the Stokes equations, Eq. (2).

Provided that the interpolation and spreading between  $\mathbf{f}_{i,j,k}$  and  $-\mathbf{F}_l$  preserves the local stress, we obtain the dimensionless weighted dipole moment  $\tilde{\mathbf{s}}$  needed to compute particle interactions as

$$\tilde{\mathbf{s}} = - \sum_{l=1}^{N_l} z_l (h - z_l) \mathbf{F}_l \Delta V_l. \quad (88)$$

The dimensional  $\mathbf{s}$  is thus  $\eta U_b (2a)^3 \tilde{\mathbf{s}}$ .

## REFERENCES

- BEATUS, T., BAR-ZIV, R. H. & TLUSTY, T. 2012 The physics of 2d microfluidic droplet ensembles. *Physics Reports* **516** (3), 103 – 145, the physics of 2D microfluidic droplet ensembles.
- BEATUS, T., TLUSTY, T. & BAR-ZIV, R. H. 2006 Phonons in a one-dimensional microfluidic crystal. *Nat. Phys.* **2**, 743.
- ACUÑA CAMPA, H., CARBAJAL-TINOCO, M. D., ARAUZ-LARA, J. L. & MEDINA-NOYOLA, M. 1998 Collective dynamics in quasibidimensional colloidal suspensions. *Phys. Rev. Lett.* **80**, 5802–5805.
- CARBAJAL-TINOCO, M. D., CRUZ DE LEÓN, G. & ARAUZ-LARA, J. L. 1997 Brownian motion in quasibidimensional colloidal suspensions. *Phys. Rev. E* **56**, 6962–6969.
- COHEN, I., MASON, T. G. & WEITZ, D. A. 2004 Shear-induced configurations of confined colloidal suspensions. *Phys. Rev. Lett.* **93**, 046001.
- CUI, B., DIAMANT, H., LIN, B. & RICE, S. A. 2004 Anomalous hydrodynamic interaction in a quasi-two-dimensional suspension. *Phys. Rev. Lett.* **92**, 258301.
- LANCON, P., BATROUNI, G., LOBRY, L. & OSTROWSKY, N. 2001 Drift without flux: Brownian walker with a space-dependent diffusion coefficient. *Europhysics Letters (EPL)* **54** (1), 28–34.

- MARCUS, A. H., SCHOFIELD, J. & RICE, S. A. 1999 Experimental observations of non-gaussian behavior and stringlike cooperative dynamics in concentrated quasi-two-dimensional colloidal liquids. *Phys. Rev. E* **60**, 5725–5736.
- PESCHÉ, R. & NÄGELE, G. 2000 Stokesian dynamics study of quasi-two-dimensional suspensions confined between two parallel walls. *Phys. Rev. E* **62**, 5432–5443.
- SANTANA-SOLANO, J. & ARAUZ-LARA, J. L. 2001 Hydrodynamic interactions in quasi-two-dimensional colloidal suspensions. *Phys. Rev. Lett.* **87**, 038302.
- SANTANA-SOLANO, J. & ARAUZ-LARA, J. L. 2002 Short-time dynamics of colloidal particles confined between two walls. *Phys. Rev. E* **65**, 021406.
- SARIG, I., STAROSVETSKY, Y. & GAT, A. D. 2016 Interaction forces between microfluidic droplets in a hele-shaw cell. *Journal of Fluid Mechanics* **800**, 264–277.
- TLUSTY, T. 2006 Screening by symmetry of long-range hydrodynamic interactions of polymers confined in sheets. *Macromolec* **39**, 3927.

